
Electronic Thesis and Dissertation Repository

11-25-2014 12:00 AM

Monostatic Airborne Synthetic Aperture Radar Using Commercial WiMAX Transceivers In the License-exempt Spectrum

Kai Liu, *The University of Western Ontario*

Supervisor: Dr. Xianbin Wang, *The University of Western Ontario*

Joint Supervisor: Dr. Jagath Samarabandu, *The University of Western Ontario*

A thesis submitted in partial fulfillment of the requirements for the Master of Engineering Science degree in Electrical and Computer Engineering

© Kai Liu 2014

Follow this and additional works at: <https://ir.lib.uwo.ca/etd>



Part of the [Other Electrical and Computer Engineering Commons](#), [Signal Processing Commons](#), and the [Systems and Communications Commons](#)

Recommended Citation

Liu, Kai, "Monostatic Airborne Synthetic Aperture Radar Using Commercial WiMAX Transceivers In the License-exempt Spectrum" (2014). *Electronic Thesis and Dissertation Repository*. 2611.
<https://ir.lib.uwo.ca/etd/2611>

This Dissertation/Thesis is brought to you for free and open access by Scholarship@Western. It has been accepted for inclusion in Electronic Thesis and Dissertation Repository by an authorized administrator of Scholarship@Western. For more information, please contact wlsadmin@uwo.ca.

MONOSTATIC AIRBORNE SYNTHETIC APERTURE RADAR USING
COMMERCIAL WIMAX TRANSCEIVERS IN THE LICENSE-EXEMPT
SPECTRUM

(Thesis format: Monograph)

by

Kai Liu

Graduate Program in Engineering Science of Electrical and Computer
Engineering

A thesis submitted in partial fulfillment
of the requirements for the degree of
Masters of Science Engineering

The School of Graduate and Postdoctoral Studies
The University of Western Ontario
London, Ontario, Canada

© Kai Liu 2014

Abstract

The past half-century witnessed an evolution of synthetic aperture radar (SAR). Boosted by digital signal processing (DSP), a variety of SAR imaging algorithms have been developed, in which the wavenumber domain algorithm is mature for airborne SAR and independent of signal waveforms. Apart from the algorithm development, there is a growing interest in how to acquire the raw data of targets' echoes before the DSP for SAR imaging in a cost-effective way. For the data acquisition, various studies over the past 15 years have shed light on utilizing the signal generated from the ubiquitous broadband wireless technology – orthogonal frequency division multiplexing (OFDM). However, the purpose of this thesis is to enable commercial OFDM-based wireless systems to work as an airborne SAR sensor.

The unlicensed devices of Worldwide interoperability for Microwave Access (WiMAX) are the first option, owing to their accessibility, similarity and economy. This dissertation first demonstrates the feasibility of applying WiMAX to SAR by discussing their similar features. Despite the similarities they share, the compatibility of the two technologies is undermined by a series of problems resulted from WiMAX transceiver mechanisms and industrial rules for radiated power. In order to directly apply commercial WiMAX base station transceivers in unlicensed band to airborne SAR application, we propose a radio-frequency (RF) front design together with a signal processing means. To be specific, a double-pole, double-throw (DPDT) switch is inserted between an antenna and two WiMAX transceivers for generating pulsed signal. By simulations, the transmitted power of the SAR sensor is lower than 0dBm, while its imaging range can be over 10km for targets with relatively large radar cross section (RCS), such as a ship. Its range resolution is 9.6m whereas its cross-range resolution is finer than 1m. Equipped with the multi-mode, this SAR sensor is further enhanced to satisfy the requirements of diversified SAR applications. For example, the width of the scan-mode SAR's range swath is 2.1km, over five times the width of other modes. Vital developed Matlab code is given in Appendix D, and its correctness is shown by comparing with the image of chirped SAR.

To summarize, the significance of this dissertation is to propose, for the first time, a design of directly leveraging commercial OFDM-based systems for airborne SAR imaging. Compared with existing designs of airborne SAR, it is a promising low-cost solution.

Keywords: SAR, WiMAX, OFDM, DPDT, low-cost, multi-mode.

You never grow old
you become old by not continuing to grow.

**This thesis is dedicated
To my beloved Parents, Wife and Baby.**

Acknowledgements

First, I would like to offer my overwhelming gratitude to my supervisor, Dr. Xianbin Wang for his guidance, support and encouragement. His enlightening supervisions inspired me with confidence to undertake this research, broadened my outlook and helped me organize my ideas. It was a productive and joyful journey to learn from him.

Second, I would like to thank my co-supervisor, Dr. Jagath Samarabandu for his mentoring, for shaping my scattered ideas and for pointing out the primary problems in my research. It was my pleasure to work with him.

I am also grateful for Dr. Xianbin Wang and Dr. Jagath Samarabandu's understanding and leniency for the delayed research progress due to my baby's birth in the middle of my graduate studies.

Genuine thanks to Dr. Luiz Fernando Capretz, Dr. Abdallah Shami and Dr. Lucian Ilie for sparing their valuable time in reviewing my dissertation and serving as my examination committee. True thank also to Dr. Hanif Ladak for his gateway course of Matlab and serving as the chair of my thesis examination board.

I would like to express my sincere thanks to Dr. Auon Muhammad Akhtar, for his patience and preciseness in helping me revise my academic paper. Also, earnest thanks to group fellows, Dr. Aydin Behnad, Dr. Arash Khabbazibasmenj and Jiazi Liu for their instructive suggestions about paper-writing skills. Many thanks also to other group members, and it was gratifying to work with you.

Heartfelt thanks to the patient administrative staff in our department and to the warm-hearted librarians in the D. B. Weldon Library.

I am indebted to my beloved parents and wife. Without their unselfish help and endless love for me, I would not have completed the challenging research, which was a brand-new field of knowledge for me. I am grateful for their support, understanding and forgiveness.

Finally, I want to express appreciation for all the friends I have made in Canada and for their cordial assistance in my life.

Contents

Abstract	ii
Acknowledgements	iv
List of Figures	viii
List of Tables	xii
List of Appendices	xiii
List of Abbreviations	xiii
1 Introduction	1
1.1 Motivations	1
1.2 Purpose	2
1.3 Contributions	3
1.4 Dissertation Outline	4
2 Radar, SAR and WiMAX	6
2.1 Chapter Introduction	6
2.2 Radar Fundamentals and Imaging Radar	6
2.2.1 Radar fundamentals	6
2.2.2 Imaging radar	11
2.2.3 SAR parameters specifications	15
2.3 SAR Operating Modes and Its Imaging Algorithms	19

2.3.1	Primary SAR operating modes	20
2.3.2	Wavenumber domain algorithm	25
2.4	Airborne SAR and Broadband Wireless Technologies	31
2.4.1	Current airborne SAR applications	31
2.4.2	WiMAX and other OFDM-based wireless systems	32
2.4.3	Similarities between SAR and WiMAX	37
2.5	Chapter Summary	45
3	Problems of Utilizing WiMAX for SAR	46
3.1	Chapter Introduction	46
3.2	WiMAX Transceiver Mechanism	46
3.2.1	Transmitter signal form	46
3.2.2	Receiver structure	49
3.3	Power Restrictions	49
3.3.1	Transmitted power restriction from industrial regulations	49
3.3.2	Practical consideration for the processing gain of SAR	50
3.4	Chapter Summary	56
4	Airborne Stripmap SAR Using License Exempt WiMAX Transceivers	57
4.1	Chapter Introduction	57
4.2	System Model of WiMAX SAR	58
4.3	Range Matched Filtering by WiMAX Receiver	59
4.4	RF Design for WiMAX SAR	65
4.4.1	System range level	66
4.4.2	Design to increase signal processing gain	67
4.5	System Parameters and Simulation Results	72
4.5.1	Image quality improvement by increasing PRF	73
4.5.2	Ideal and real WiMAX SAR image	76
4.5.3	Code correctness verification	77
4.6	Chapter Summary	80

5	Enhanced WiMAX SAR System Equipped with Multiple Modes	81
5.1	Chapter Introduction	81
5.2	System Model of Multi-mode WiMAX SAR	82
5.3	Scan-mode WiMAX SAR	87
5.3.1	Operating range	87
5.3.2	Geometry	88
5.4	Simulation Results	92
5.5	Evaluation of WiMAX SAR	97
5.6	Chapter Summary	98
6	Conclusion and Future Work	99
6.1	Conclusion	99
6.2	Future Research	100
A	Derivation of Eq. (2.30) using MSP	102
B	Target's cross-range resolution of squint spotlight SAR	104
C	Area expansion due to squint angle	106
D	Key developed Matlab code	108
	Bibliography	110
	Curriculum Vitae	114

List of Figures

2.1	Flow chart of signal processing for high range resolution	9
2.2	Schematic of envelope detection for radar signal by a matched filter	10
2.3	Cross range resolution of real aperture radar.	13
2.4	Cross range resolution comparison between SAR and RAR.	14
2.5	Three dimensional geometry of an airborne stripmap SAR. gr , x and y are ground range, cross range and altitude, respectively, while r represents the slant range. Red area is actual SAR imaging plane, and blue shadow area is slant-range plane.	15
2.6	Two fundamental modes of airborne SAR.	20
2.7	Schematic of a stripmap SAR, where L_x is the length of flight path to ensure the uniform cross-range resolution ΔCR for whole target area, while L_a is aperture size for one target with range of r_c , and a_w is the width of azimuth imaging unit.	21
2.8	Schematic of a broadside spotlight SAR, where ρ is rotational angle of the whole flight path of SAR platform from the perspective of the target at the center of the rectangular target area.	22
2.9	Schematic of a scan-mode SAR, in which the flight length L_{x2} is bigger than L_{x1} due to larger azimuth width a_{w2} of imaging area, corresponding to the farther range swath r_{sw2}	24
2.10	Schematic of a squint stripmap SAR. Its target area requires to be enlarged to cover the counterpart area of broadside stripmap SAR, causing flight length increased by ΔL_x	24

2.11	Two major steps for all SAR receivers: First is two dimensional compression for targets at reference range, while the second is algorithm-dependent correction for focusing all other targets in the imaging area.	26
2.12	Flow chart of SAR imaging processed by ΩKA algorithm.	28
2.13	Basic diagram of an generally-accepted OFDM system.	33
2.14	Downlink subframe structure of WirelessMAN OFDM PHY for WiMAX base station in TDD mode.	35
2.15	Range and cross-range imaging with resolution of 7.5m and 0.5m, respectively.	39
2.16	Channels comparison between radar and wireless communications	41
2.17	Radio frequency (RF) block diagram of a WiMAX receiver	43
3.1	Envelope detection and threshold judge of a radar receiver for the single-carrier sinusoidal waveform.	52
3.2	Comparison between simulation results and theoretical equation for obtaining the detectable probability of an OFDM symbol by envelope detection.	53
3.3	Reconstructed SAR image by ΩKA algorithm	55
3.4	Envelope detection judged by a threshold of 167.6	55
4.1	Block diagram of WiMAX SAR system. The memory device is needed to collected the frequency-domain echo data for the following software-based 2-D imaging.	58
4.2	The operation of circulant convolution between an OFDM symbol and channel, which is established through the inserted cyclic prefix (CP).	60
4.3	The pulse, with the length of an OFDM symbol, is transmitted and received by WiMAX SAR.	64
4.4	Schematic diagram of WiMAX SAR RF design. When the black switches are working, WiMAX SAR is transmitting. When a whole symbol is already transmitted, the red switches work for echo receiving as shown in Figure 4.3.	68
4.5	The reasons why two WiMAX base stations are required to be used include: forcing the length of pulses to be only one symbol duration; obtaining constant PRF; increasing the PRF to satisfy the requirement of Doppler bandwidth.	70

4.6	The proposed design can avoid negative effects such as large minimum range due to the length of TTG or RTG, and bandwidth loss caused by the symbols of preambles, by using a fast controlled DPDT switch for two WiMAX base station transceivers.	72
4.7	WiMAX SAR image for testing its real resolutions. Since the rectangular waveform could cause high sidelobes, the real range resolution could be lower than the theoretical one. Similarly, the sidelobes of antenna beam could widen the pixels in azimuth direction.	74
4.8	Comparison of image quality of WiMAX SAR with different PRF. By increasing the PRF by more than 3dB, the detectability of point targets is much better when the input SNR before signal processing is only -30dB.	75
4.9	Image of Golden Gate Bridge reconstructed by WiMAX SAR. These figures shows the imaging capability of WiMAX for distributed targets, whose original SAR image by AirSAR has different range and cross-range resolutions.	76
4.10	Nine point targets are imaged by WiMAX SAR, in which three targets within range swath (2100m-2500m) have uniform high intensity while others' intensities become weak as their range increase.	78
4.11	Nine point targets are imaged by chirped SAR and WiMAX SAR using $\Omega K A$ algorithm without additive noise.	79
5.1	Block diagram of the simulation model for proposed multi-mode WiMAX SAR, in which the controlled DPDT module is used for converting continuous OFDM waveform into pulsed shape.	83
5.2	Imaging geometry of multi-mode WiMAX SAR. Due to the squint angle Θ , imaging area of spotlight and squint modes (red dashed rectangle) is different from that of stripmap and scan modes (shaded region).	84
5.3	Geometry of scan-mode SAR imaging for one sub-swath. L_b is the burst length in which SAR transmits and receives while L_p is the repetition interval of two neighboring bursts. L_{am} is the aperture size of stripmap SAR.	89
5.4	Geometry of scan-mode WiMAX SAR in range-height domain.	90

5.5	Imaging area of scan-mode WiMAX SAR, where the shaded rectangular region is the imaging area in one scanning process. The Doppler center positions x_c for different sub-swaths are given by green lines.	91
5.6	Comparison of images between stripmap and scan mode. The range swath of stripmap mode is 350m while the scan mode is 2100m. However, the cross-range resolution of stripmap WiMAX SAR is much finer.	93
5.7	Comparison of images of 75 point targets with RCS of 200m ² between scan and spotlight modes. The cross-range spacing of two targets is only 1.5m and the slant range swath is 350m.	94
5.8	Comparison between broadside and squint stripmap modes for imaging the farthest sub-swath. Target RCS is 3000m ² and Doppler center position x_c is 37.5m instead of 0m.	95
5.9	Comparison of images for 4 th sub-swath in scan-mode WiMAX SAR with and without windowing. The ghost images in range direction are reduced by this scheme.	96
B.1	Target cross-range resolution for the squint spotlight SAR.	105
C.1	Area expansion in spotlight or squint SAR, where Θ is squint angle.	107

List of Tables

2.1	System parameters comparison among LTE, WiFi and WiMAX	37
2.2	Range and cross-range resolutions for SAR of two basic modes	38
2.3	Link Budget parameters for WiMAX	42
2.4	A sample link budget parameters for WiMAX	42
3.1	Symbol time duration of WirelessHUMAN	47
3.2	Detection probability of single OFDM symbol with respect to SNR_{in}	53
3.3	Parameters of WiMAX SAR for imaging one point target	54
4.1	Simulation parameters of WiMAX SAR	73
5.1	Burst and center aperture size of each sub-swath	91
5.2	The image SNR for different slant range of scan mode	93
5.3	Estimated working ranges for targets of different RCS by stripmap WiMAX SAR	97
5.4	WiMAX SAR in comparison with other similar SAR systems	97

List of Appendices

Appendix A Derivation of Eq. (2.30) using MSP	102
Appendix B Target's cross-range resolution of squint spotlight SAR	104
Appendix C Area expansion due to squint angle	106
Appendix D Key developed Matlab code	108

List of Abbreviations

Abbreviation	Full name	First use
A/D	Analog-to-Digital converter	34
AWGN	Additive White Gaussian Noise	4
COTS	Commercial Off-The-Shelf	2
CP	Cyclic Prefix	4
D/A	Digital-to-Analog converter	33
DFT	Digital Fourier Transformation	62
DL	Downlink	35
DPDT	Double-Pole, Double-Throw	57
DSP	Digital Signal Processing	4
EIRP	Equivalent Isotropically Radiated Power	16
FCC	Federal Communications Commission	34
FFT	Fast Fourier Transformation	32
FT	Fourier Transformation	9
IDFT	Inverse Digital Fourier Transformation	59
IFFT	Inverse Fast Fourier Transformation	32
IFT	Inverse Fourier Transformation	8
ISM	Industrial, Scientific and Medical	35
LFM	Linear Frequency Modulation	9
LNA	Low-Noise Amplifier	33
LO	Local Oscillator	32
LOS	Line-Of-Sight	40
LTE	Long Term Evolution	34
MAPL	Maximum Allowable Path Loss	44
MSP	Method of Stationary Phase	30

NLOS	Non-Line-Of-Sight	40
OFDM	Orthogonal Frequency-Division Multiplexing	2
OFDMA	Orthogonal Frequency-Division Multiple Access	34
Ω KA	Wavenumber Domain Algorithm	25
P/S	Parallel-to-Serial converter	33
PA	Power Amplifier	33
PAPR	Peak-to-Average Power Ratio	34
PRF	Pulse Repetition Frequency	4
PSD	Power Spectrum Density	10
PSK	Phase Shift Keying	33
PHY	Physical Layer	34
QAM	Quadrature Amplitude Modulation	33
RAR	Real Aperture Radar	12
RCS	Radar Cross Section	11
RDA	Range Doppler Algorithm	26
RF	Radio-Frequency	2
RTG	Receive-to-transmit Transition Gap	69
S/P	Serial-to-Parallel converter	34
SAR	Synthetic Aperture Radar	1
SNR	Signal-to-Noise Ratio	4
TDD	Time Division Duplexing	35
TTG	Transmit-to-receive Transition Gap	48
UAS	Unmanned Aerial System	1
UL	Uplink	35
WiFi	Wireless Fidelity	36
WiMAX	Worldwide interoperability for Microwave Access	2
WirelessHUMAN	Wireless High-speed Unlicensed Metropolitan Area Network	35
WirelessMAN	Wireless Metropolitan Area Network	34
WLAN	Wireless Local Area Network	36

Chapter 1

Introduction

1.1 Motivations

Synthetic aperture radar (SAR), working in microwave spectrum, plays an increasingly vital role in remote sensing field due to its outstanding feature of forming high-resolution images independent of brightness and weather conditions. This imaging radar requires a moving platform such as a satellite, an aircraft or an unmanned aerial system (UAS), to gain the targets' information of large azimuth bandwidth by collecting numerous returns over a flight path. Since the data acquired during the path produces a high-resolution image by post processing, the relatively long path resembles an aerial antenna with large aperture size. For the last three decades, the distinguished clairvoyance of SAR has been extensively utilized for earth surface observation and exploration. Apart from high resolution, this application also demands a large SAR imaging area, which necessitates a spaceborne SAR sensor mounted on an orbiting satellite. Although the earth remote sensing is of great importance for human survival and development, the air surveillance or small-scale remote sensing is indispensable as well in some military and civil applications. For example, airborne SAR is used to the reconnaissance mission for the detection and imaging of intruding vessels day and night on the coastal border. Actually, the thesis was motivated by an interest from industry. A technology company proposed a project to utilize cutting-edge wireless techniques, in order to design a SAR system for carrying out the regional search and rescue for automobiles, aircrafts or ships in distress. Apart from good imaging quality, timeliness is also essential in the above-mentioned examples. To this end, the

airborne SAR is a better option than the spaceborne one.

On the other hand, the rapid advancement of microelectronic technology enables the emergence and proliferation of the miniaturized, lightweight and integrated radio-frequency (RF) or microwave circuits, which offered an impetus for manufacture of the low-cost, small-sized equipment in the vigorous industry of wireless communications. It stands to reason that radar or SAR applications are willing to take advantage of these sophisticated commercial off-the-shelf (COTS) wireless devices. This modernizes the SAR system in a cost-effective way, while opens a potential niche market for the vendors from the communication industry. The design of current wireless systems aims at providing users with high-speed, reliable and informative communication service, which requires broader bandwidth, larger throughput, higher data rate and lower bit error rate. Some of these attributes, such as broadband, can be exploited by radar or SAR systems. Undoubtedly, the orthogonal frequency-division multiplexing (OFDM) is the most representative technique as it has been integrated into a multitude of contemporary wireless or mobile applications. Further, OFDM waveform has been verified for radar applications since this century. It is a challenge as well as an opportunity to develop an effective system method of manipulating COTS OFDM-based wireless devices for SAR imaging.

1.2 Purpose

An OFDM symbol, as a multiple frequency phase code from the radar signal perspective, was proved as a competitive candidate radar waveform ten years ago, due to its high auto-correlation peak while low cross-correlation peaks [1]. Afterwards, a variety of OFDM-based radar designs and products sprang up, including the applications in the SAR scenario. An ultra-wide band (UWB) SAR of was developed by using OFDM signal [2]. It demonstrates the potential anti-interference ability of OFDM pulse due to its dynamic range allocation and easy-made pulse diversity. However, the imaging range could be as small as only 10m-range level due to the weak transmitted power of UWB signal as well as low gain of UWB antenna. Recently, the commercial OFDM-based worldwide interoperability for microwave access (WiMAX) systems have been exploited for passive SAR to collect the target-reflected echo data [3]. The bistatic passive airborne SAR using the widely-distributed WiMAX signal, as it were, is a promising

application owing to its attainable large operating range and free-to-use transmitter. However, its receiving system is much more complicated and pricey. Apart from using a radar receiver for collecting targets' returns, the system requires another receiver for receiving continuous OFDM waveform from commercial WiMAX base stations first, followed by a module to estimate the timing and shape of upcoming transmitted signal for effective matched filtering in the radar receiver. Moreover, the availability of the signal source is uncertain while its location is fixed. All these features exert negative impacts on the bistatic SAR for reliable imaging, although the stability is the most important consideration in the radar field. Thus, a monostatic SAR is preferable. On the other hand, there is a trend of saving budget for SAR applications. A low-cost SAR system, termed BYU μ SAR, was proposed [4], which shows its components still cost several thousand dollars. With the rapid development of wireless industry, an on-chip WiMAX transceiver costs only fifteen dollars [5]. The thesis aims at developing a simple and cost-effective approach to make full use of quality and inexpensive commercial WiMAX transceivers to provide a low-cost solution for monostatic airborne SAR imaging.

1.3 Contributions

- First, the thesis proposes a small-scale RF-front modification for two COTS WiMAX base station transceivers with high-quality and cheap price, converting them to a low-cost, low-powered and lightweight airborne SAR sensor (call it WiMAX SAR) to collect raw data for SAR application with the aid of SAR imaging algorithms. By simulation, its finest range and cross-range resolutions are 9.6m and 0.5m, respectively. The effective range swath of proposed stripmap WiMAX SAR is as wide as 400m, while its operating range can be over 10km with transmitted power of only -3dBm (0.5mW). It is noteworthy the design is applicable to any OFDM-based transceivers.
- Secondly, WiMAX SAR is further enhanced by integrating multiple modes to satisfy the requirements of diverse applications. For instance, the swath width is increased by six times in scanning mode while the transmitted pulses can be saved in spotlight mode.
- Moreover, an analysis is given to explain the relation between the required input signal-

to-noise ratio (SNR) at receiver end and the detection probability of a steady target by matched filtering an OFDM symbol under the condition of the additive white Gaussian noise (AWGN). By the two-dimensional imaging processing, the input SNR can be as low as -30dB for obtaining the detection probability of over 0.999.

- Further, the cyclic prefix (CP) in OFDM symbols and the digitally modulated data are utilized for WiMAX receiver to work as a SAR receiver.
- In addition, the formulae related to adopted SAR algorithm and system model in the format of OFDM waveform are derived for readers to comprehend the thesis readily.
- Finally, a digital signal processing (DSP) way is proposed for ghost image reduction in range dimension. This method can improve target detection at the cost of coarser range resolution, which is used to locate a imaging target.

1.4 Dissertation Outline

This dissertation is composed of six chapters and the rest part is organized as follows.

Chapter 2 depicts the technical background and fundamental concepts for radar, SAR and WiMAX. The first section shows how this chapter is organized, while the two following sections explicate the marked features for radar and SAR in turn. The similarities between the two technologies of SAR and OFDM-based WiMAX is demonstrated in Section 2.4, and this chapter ends up a short summary.

Chapter 3 points out several inevitable challenges and their causes. The incompatibilities for these two technologies are primarily caused by their different transceiver mechanisms and the industrial power restriction for unlicensed WiMAX devices.

Chapter 4 proposes an RF-front modification to bridge the gap between WiMAX system and monostatic SAR sensor. Some decisive parameters, such as receiver sensitivity, isolation and pulse repetition frequency (PRF) are detailed to demonstrate the effectiveness of this design. Moreover, simulation results validate the analysis of input SNR requirement. The features and restrictions of the proposed stripmap WiMAX SAR are discussed eventually.

Chapter 5 further improves the WiMAX SAR system by introducing multiple SAR modes, which overcomes the range swath constraint of stripmap mode and extends the application scope of this system. The scan-mode WiMAX SAR is specified while other modes are sketched by showing significant features. The simulation results vividly reflect the utilities of all the modes of proposed multi-mode WiMAX SAR.

Chapter 6 summarizes the studies of this dissertation and suggests some potential future tasks finally.

Chapter 2

Radar, SAR and WiMAX

2.1 Chapter Introduction

The chapter introduces the background of SAR, WiMAX and their connections, laying a solid foundation for the fusion of these two technologies in the remaining chapters. Since SAR is a modern imaging radar, we first explain primary concepts of radar as well as imaging radar before explaining SAR. Subsequently, the operating modes and imaging algorithms of SAR are described in Section 2.3, in which the wavenumber domain algorithm is detailed due to its application in this thesis. In order to illustrate the feasibility of applying WiMAX to SAR, Section 2.4 demonstrates the similarities between airborne SAR and broadband wireless technologies. Finally, a short chapter summary is given for recapitulating the current chapter and foreshadowing the next chapter.

2.2 Radar Fundamentals and Imaging Radar

2.2.1 Radar fundamentals

Radio and its applications Ever since the famous mathematical physicist, James Clerk Maxwell predicted the electromagnetic (EM) wave propagates through free space at a speed of light by the publication of *A Dynamical Theory of the Electromagnetic Field* in 1865, a new form of signal, called *radio*, was found and applied extensively thereafter. Microwave

spectrum, as a portion of radio frequency band, plays a crucial role in contemporary world. Although it can be better guided by transmission lines, the microwave radiation gains broad interests for its ability to spread efficiently in atmosphere and vacuum as fast as light.

The discovery of radio at least boosted two essential applications, i.e. wireless communications and active remote sensing. With its growing requirements such as larger bandwidth and better anti-interference capability, the wireless industry resorts to the microwave and even millimeter wavebands currently. On the other hand, the active remote sensing exploits the penetration feature of microwave radiation for information acquisition of the earth surface. It utilizes generated microwave radiations to illuminate targets and to collect the backscattered wave reflected by targets. Most of active remote sensors at present are able to collect two-dimensional (2-D) data of targets for acquiring more information.

Radar, an acronym for radio detection and ranging, was originally used for detecting the military target and measuring its distance in all-weather conditions by transmitting radio signal and receiving the returns from targets. The functions of modern radars are extended to radio tracking and imaging. Owing to its outstanding features in terms of working frequency, well-established techniques and multi-dimensional information acquisition, radar is adopted as the most common sensor in active remote sensing.

Range and Resolution There are two important parameters for the basic non-imaging radar: range and range resolution. The former represents how far a target can be measured while the latter denotes how close two targets can be distinguished in range direction by radar.

The operating range counts on many parameters and will be detailed later. Given that the range between a radar and a target is R and the radio speed in free space is c (the speed of light), a signal transmitted from a radar sensor travels the distance of R to arrive at the target, then the echo backscattered from the target goes through same distance to reach the sensor. If it takes the time of t_2 from signal transmission to echo reception, R is half of ct_2 . The round-trip feature of a radar signal is equivalent to a single-trip propagation with the speed of $\frac{c}{2}$.

The range resolution depends on the duration t_{sp} of a simple pulse, since two targets can be distinguished as long as their spacing distance is bigger than the distance equaling to $\frac{c}{2}t_{sp}$. As

shown in many works of the radar field [6, 7], the range resolution satisfies:

$$\Delta R = \frac{c}{2B}, \quad (2.1)$$

where B is the signal frequency bandwidth. For a simple pulse, its bandwidth B is the reciprocal of its pulse width t_{sp} , thereby causing range resolution of $\frac{c}{2}t_{sp}$.

Radar signal features In accordance with different application objectives, radar signals can be classified as two major types, i.e. pulses and the continuous wave (CW). The former is commonly used for detecting the range of a stationary or slow-moving target, while the latter utilizes the Doppler effect to measure the speed of a moving target. Although the CW is always used to detect track those fast-moving targets threatening public safety for national defense and traffic safety, pulsed waveform is adopted for wider applications, including the military reconnaissance and civilian remote sensing. This thesis only concerns the pulsed waveform.

As mentioned above, a shorter simple pulse leads to better range resolution. However, if the simple pulse is too short, the radar transmission power will be restricted, causing the lower energy of received echo reflected by targets in certain range. Since the receiver sensitivity is limited, the pulse of short width limits the operating range of radar. In order to maintain the working range, the pulse power has to be increased. Compared with a high-power short burst, a longer pulse with low-power is easier to be generated for increasing transmission power. Nonetheless, a longer simple pulse causes lower frequency bandwidth, which is adverse to acquired resolution.

The way to gain both advantages is called pulse compression. The *signal and system* course tells us if a signal in time domain is a rectangular pulse, its corresponding signal form in frequency domain is a *sinc* function with effective bandwidth of mainlobe's size, and vice versa. As we know, a signal with rectangular amplitude spectrum multiplied by its complex conjugate in frequency domain results in the signal's power or energy spectrum of similar rectangular shape. Thus, if we can expand the amplitude spectrum of a pulse from a *sinc* function to a rectangle-like function at the transmitter with C_f times the width of *sinc*'s mainlobe, then a *sinc*-like function in time domain can be yielded by the inverse Fourier transform (IFT). The

peak of this function will be at the time instant indicating target's range. Therefore, the range resolution of a target is improved to be the width of the mainlobe of the *sinc*-like function, which is $\frac{1}{C_f}$ of the pulse duration t_p . C_f is the compression factor and the bandwidth B is $\frac{C_f}{t_p}$.

Figure 2.1 visualizes this idea to enhance resolution while keeping the wide pulse, in which we call the operation of spreading signal's amplitude spectrum into a rectangle shape to be SSR while the Fourier transform and its inverse briefed as FT and IFT, respectively. Many frequency-modulated signals have the features of SSR, among which the linear frequency modulation (LFM) signal is the most widely used. However, the OFDM symbol also possesses this feature. Due to additive noise of received signal, a filter is needed to acquire the rectangular spectrum at the receiver end.

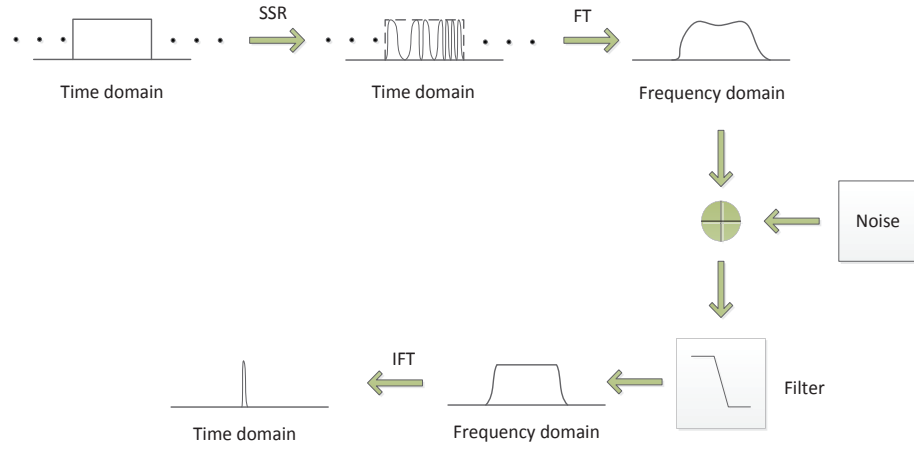


Figure 2.1: Flow chart of signal processing for high range resolution

Matched filtering Once the baseband signal form is ascertained, the next step is to extract the useful spectrum from the received spectrum distorted by noise. The noise can be approximated as the additive white Gaussian noise(AWGN). To this end, the first option is matched filter [6, 8, 9], due to the fact that it not only outputs the energy spectrum of the deterministic transmitted signal as mentioned before, but maximizes the SNR.

Figure 2.2 depicts the classical process for radar signal detection, where a matched filter is used to maximize the strength of received signal. $H(f)$ represents the transfer function of the filter, $s_r(t)$ is the input of matched filter, comprised of the echo pulse $s_e(t)$ and the AWGN $n(t)$. The last block is the threshold comparator to judge if there is a target or not, in which the Th

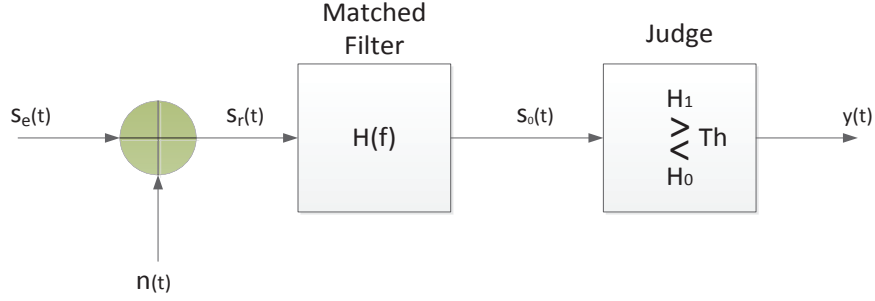


Figure 2.2: Schematic of envelope detection for radar signal by a matched filter

denotes the threshold while H_1 and H_0 are used to show if a target exists or not. The output after matched filter is $s_0(t)$, which consists of filtered echo signal $e_0(t)$ and output noise $n_0(t)$. According to the Figure 2.2, we can derive this output signal in time domain as:

$$s_0(t) = \int_{-\infty}^{\infty} S_0(f) e^{j2\pi ft} df = \int_{-\infty}^{\infty} S_r(f) H(f) e^{j2\pi ft} df, \quad (2.2)$$

where $S_r(f)$ is the spectrum of $s_r(t)$. Since AWGN is a random signal, it is power-limited rather than energy-limited, due to its infinite bandwidth theoretically. Thus, the AWGN is measured by its power spectrum density (PSD): $\frac{N_0}{2} = kT$ with unit of W/Hz or J, where k is the Boltzmann constant while T is the temperature of Kelvin. When the band-unlimited noise goes through a band-limited matched filter, the output noise energy is limited and can be yielded by:

$$E_{n_0} = \int_{-\infty}^{\infty} P_{n_0}(f) df = \int_{-\infty}^{\infty} \frac{N_0}{2} |H(f)|^2 df = \frac{N_0}{2} \int_{-\infty}^{\infty} |H(f)|^2 df. \quad (2.3)$$

Therefore, the output SNR γ_0 can be derived by:

$$\gamma_0 = \frac{E_{e_0}}{E_{n_0}} = \frac{\left| \int_{-\infty}^{\infty} S_e(f) H(f) e^{j2\pi ft} df \right|^2}{\frac{N_0}{2} \int_{-\infty}^{\infty} |H(f)|^2 df}. \quad (2.4)$$

Based on Cauchy-Schwarz inequality, we can derive:

$$\gamma_0 \leq \frac{\int_{-\infty}^{\infty} |S_e(f) e^{j2\pi ft}|^2 df \int_{-\infty}^{\infty} |H(f)|^2 df}{\frac{N_0}{2} \int_{-\infty}^{\infty} |H(f)|^2 df} = \frac{\int_{-\infty}^{\infty} |S_e(f)|^2 df}{\frac{N_0}{2}} = \frac{2E}{N_0}, \quad (2.5)$$

where the equal sign works if and only if the relation $H(f) = S_e^*(f) e^{-j2\pi ft}$ is satisfied. $S_e(f)$

is the spectrum of echo signal $s_e(t)$ while the E is the energy of the input pulse. Thus, the maximum SNR is $\gamma_{max} = \frac{2E}{N_0}$, which is independent of the form of input signal and relies only on its energy. The threshold, used to judge if there is a target, can be set between zero and the γ_{max} . The received rectangular energy spectrum in Figure 2.1 is therefore obtained by the matched filter. Surpassing the preset threshold Th , the detected time-domain impulse is a blip indicating a target's range position of a conventional radar display, while denoting the target's range coordinate in a two-dimensional (2-D) display of an imaging radar.

Radar cross section (RCS) RCS is a measure of a target's capability to scatter the radar signal back to the radar receiver. It is always denoted by σ . More precisely, it can be viewed as the product of target reflectivity, directivity and its projected cross section. When the transmitted signal is intercepted by a target, the signal energy could be either scattered by the target or penetrating the target. The percent of scattered energy is called target reflectivity. For a perfectly smooth target, it is 100%. Provided that the energy scattering is uniformly allocated in all spatial directions, the quota in one direction is a reference value. Directivity is the ratio of the energy backscattered in the direction of radar to the reference value. Directivity counts on target's shape, operating frequency or wavelength. When the wavelength is much smaller than its radius, a sphere's scattering pattern is isotropic, resulting in its directivity is one [10]. The projected cross section can be calculated. Thus, the RCS of a perfectly smoothed sphere with cross sectional area of one square meters is $1m^2$, which is the unit area for RCS. The discussion above assumes that the target is of simple shape and is close to stationary. For the RCS of the complex moving target, the readers can refer to Barton's book [7].

2.2.2 Imaging radar

In remote sensing field, the imaging sensors can be divided into two primary types: active and passive. The principles of their imaging are quite different. Unlike active one, the passive remote sensing only has a receiver, generally consisting of a set of lens, to project a target's radiation or reflection to its sensor. Moreover, its operating electromagnetic spectrum includes visible light or infrared ray, which are the major part of the solar radiation. Furthermore, its operation is highly constrained by sunlight, weather and the intensity of the radiation sources.

In addition, the imaging resolution of passive sensing becomes poor when the sensor goes farther away from the target [11], although its resolution limit is high. As the most common active imaging sensor, the imaging radar can work in all-weather conditions. It is comprised of real aperture radar (RAR) and synthetic aperture radar (SAR). The cross-range resolution of RAR becomes higher when the radar comes closer to the target while the resolution of SAR is independent of the target's range.

Compared with RAR, one unique function of a SAR is its resolving capability in the cross-range dimension, resulting in at least two-dimensional useful information of the target at long distance. Before explaining the resolving ability of SAR, several terms are necessary to be described [12].

- Radiation intensity: it is related to far-zone electric field of an antenna, and it denotes the power radiated from an antenna per unit solid angle. Since the range between the target and the antenna is much larger than the antenna's dimension, the far field approximations can be performed.
- Antenna beamwidth: in practice, it means the half-power beamwidth (HPBW) or 3-dB beamwidth $\Delta\theta$. It is the angle between two directions in which the radiation power is half value of the whole radiated power. $\Delta\theta$ can be calculated by $k_0 \frac{\lambda}{D} (rad)$, where the λ is the wavelength, while D denotes the aperture size of antenna, which can be the azimuth size D_a or elevation size D_e , and k_0 is a constant decided by the type of antenna.
- Antenna resolution: it stands for the ability of an antenna to distinguish between two radiation sources, whose angular spacing is a half of the first-null beamwidth (FNBW). Since $\frac{\text{FNBW}}{2} \approx \text{HPBW}$, the antenna (angular) resolution is equivalent to its 3-dB beamwidth.

The spatial resolution, commonly appeared in image processing, is defined as the minimum distance between two objects which are distinguishable with each other. If an RAR is used for imaging, its cross-range resolution ΔCR_0 shares the similar meaning. The value of ΔCR_0 relates to the range R and antenna resolution $\Delta\theta$ in Figure 2.3, where the two green targets can be distinguished since their angular spacing is bigger than $\Delta\theta$ while the two yellow targets cannot be separated. According to the small-angle approximation, $\Delta CR_0 = 2R \sin(\frac{\Delta\theta}{2}) \approx R\Delta\theta$

if $\Delta\theta$ is small enough. For example, even if $\Delta\theta = 10^\circ$ and $R = 3000\text{m}$, ΔCR_0 is over 500m, while the error is only 0.67m. When the range R becomes large, the beamwidth $\Delta\theta$ has to be lower to keep fine resolution. It is noteworthy that to decrease λ or to increase azimuth size D_a can improve the cross-range resolution by this equation:

$$\Delta CR_0 \approx R\Delta\theta \approx \frac{R\lambda}{D_a}, \quad (2.6)$$

when $\Delta\theta$ is small enough and the antenna constant $k_0 = 1$. However, the antenna with too big physical aperture D_a cannot be mounted on an aircraft. Also, the radar would suffer great constraints, such as power and cost, when it works at a very short wavelength. Thus, imaging radar requires a new path to obtain high cross-range resolution.

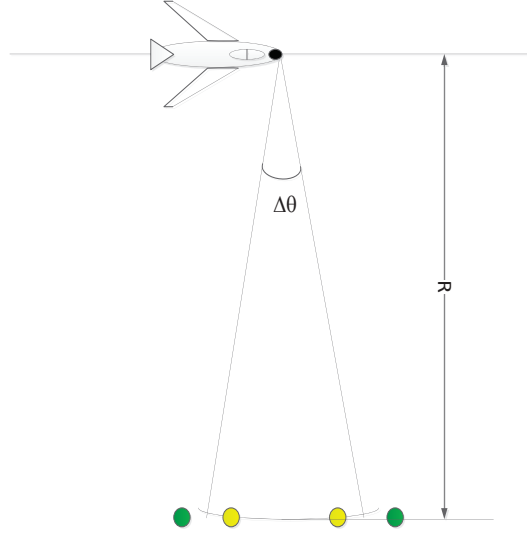


Figure 2.3: Cross range resolution of real aperture radar.

As shown in Figure 2.4, the green icon is an antenna with regular azimuth aperture size of D_a . Brown [13] demonstrated that the physical antenna assembled on an aircraft can be viewed as an element of a large linear array antenna and the length of array is synthetic aperture size depending on the range of interest. The array length is ND_a if the airplane stops, every $\frac{D_a}{2}$ meters, to transmit pulse and receive echo for $2N$ times. Intuitively, if the collected data at these $2N$ positions can be synthesized to work together for the function of a real aperture of size ND_a , the effective 3-dB beamwidth $\Delta\theta_e = \frac{\lambda}{ND_a}$, The cross-range resolution of SAR may be $\Delta CR = \frac{R\lambda}{ND_a}$, which is much finer than single array element can achieve. It seems the ΔCR can

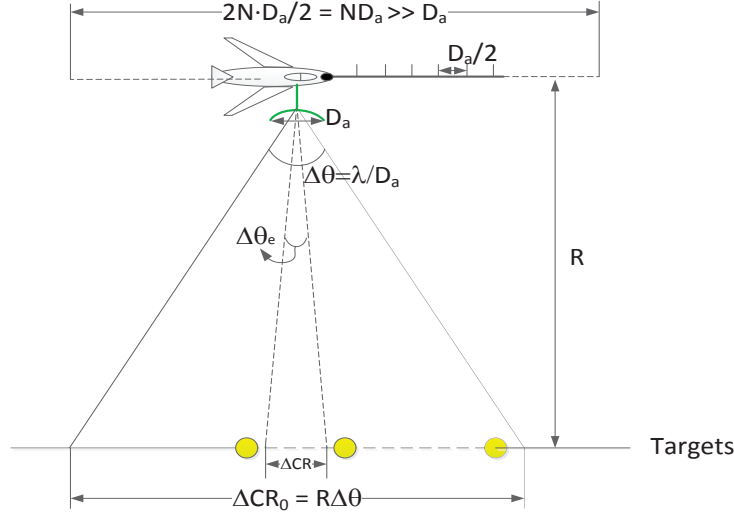


Figure 2.4: Cross range resolution comparison between SAR and RAR.

be infinitesimal if ND_a approaches infinity. Nevertheless, a target may not within the limited 3-dB beamwidth $\Delta\theta$ of the real antenna when Nd is larger than the azimuth resolution of RAR at the range R ($\Delta CR_0 = R\Delta\theta$). For stripmap SAR, synthetic aperture size for a single point target is $L_a = \Delta CR_0$ and L_a is briefed as aperture size hereafter. Thus, we can derive

$$\Delta CR = \frac{R\Delta\theta_e}{2} = \frac{R\lambda}{2L_a} = \frac{R\lambda}{2\Delta CR_0} = \frac{\lambda}{2\Delta\theta} = \frac{D_a}{2}, \quad (2.7)$$

where the effective 3-dB beamwidth $\Delta\theta_e = \frac{\lambda}{L_a}$, while 3-dB antenna beamwidth $\Delta\theta = \frac{\lambda}{D_a}$, and the factor 2 in the denominator results from the two-way path of the radar signal [14]. It is worth noting the effective cross-range resolution of SAR $\Delta\theta_e$ is proportional to the physical antenna's azimuth size D_a and is inversely related to the effective aperture size L_a .

However, if ND_a is smaller than ΔCR_0 , then $L_a = ND_a$, which yields

$$\Delta CR = \frac{R\lambda}{2ND_a}. \quad (2.8)$$

Thus, equation (2.7) shows the limit of azimuth resolution of the stripmap SAR. In practice, ND_a or L_a is selected to be smaller than the RAR's azimuth resolution ΔCR_0 . Figure 2.4 shows the SAR's effective beamwidth $\Delta\theta_e$ is smaller enough to tell the two closer yellow targets apart.

2.2.3 SAR parameters specifications

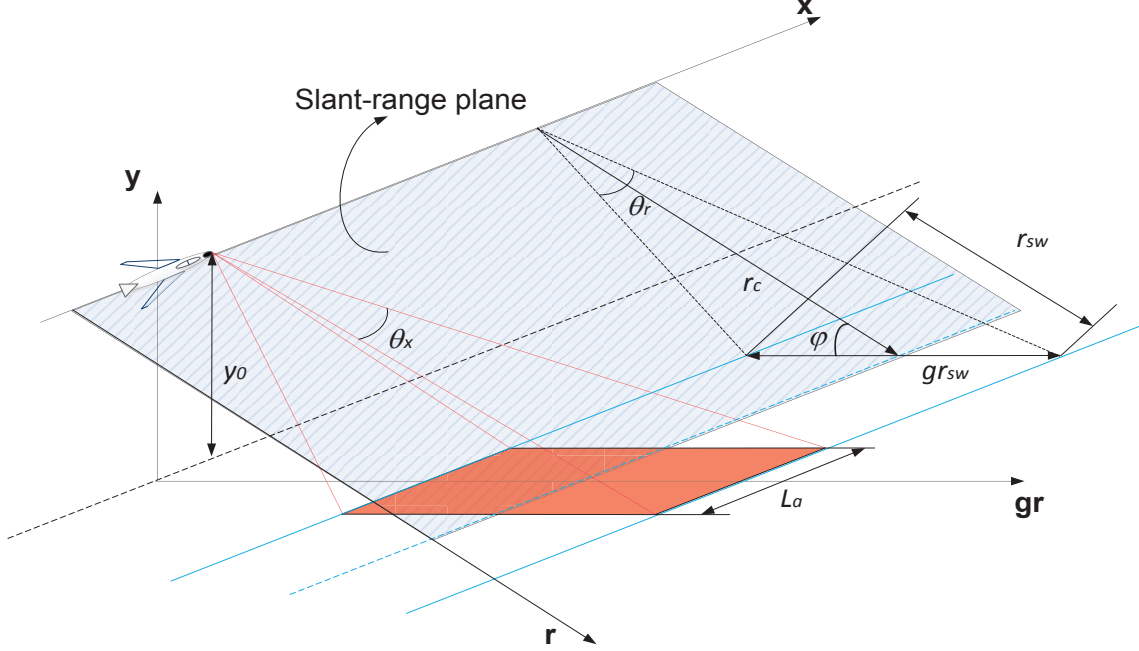


Figure 2.5: Three dimensional geometry of an airborne stripmap SAR. \mathbf{gr} , \mathbf{x} and \mathbf{y} are ground range, cross range and altitude, respectively, while \mathbf{r} represents the slant range. Red area is actual SAR imaging plane, and blue shadow area is slant-range plane.

The imaging geometry of an airborne SAR is depicted in Figure 2.5, in which some vital parameters are symbolized and adopted for the following part of this thesis. In this figure, there are four axes of coordinates, where \mathbf{x} denotes the cross range and \mathbf{y} represents the altitude; while \mathbf{r} and \mathbf{gr} are the slant range and the ground range, respectively. For a broadside SAR sensor, the direction of its side-looking antenna is in the direction of \mathbf{r} . The red rectangle is the area in the ground-range plane illuminated by the antenna of the SAR at a moment. L_a represents the aperture size for a stripmap SAR. Moreover, r_{sw} and gr_{sw} stand for the swaths of slant range and ground range. The blue shadow region denotes the slant-range plane, in which signal transmission and echo reception operate. r_c is the distance between the SAR sensor and the center of gr_{sw} , and it always works as the reference range for many SAR imaging algorithms. Provided that r_c is much larger than r_{sw} , the ground-range plane can be easily obtained by

projecting slant-range plane in this way:

$$gr_{sw} = \frac{r_{sw}}{\cos\varphi}, \quad (2.9)$$

where φ is the grazing angle. It is worth noting that the ground range swath is wider than the swath of slant range. For airborne SAR, the width of slant-range swath r_{sw} always depends on the elevation antenna 3-dB beamwidth θ_r in this approximation way:

$$r_{sw} = \frac{r_c \theta_r}{\tan\varphi}. \quad (2.10)$$

Similarly, the width of illuminating area at a moment is the aperture size L_a of broadside stripmap SAR. It is approximated as:

$$L_a = r_c \theta_x, \quad (2.11)$$

where θ_x is the azimuth antenna 3-dB beamwidth. Thus, the maximum transient illuminating area in slant-range plane could be the product of r_{sw} and L_a , which is an area projected by the red rectangle. Equations (2.10) and (2.11) are sometimes used for calculating the imaging area of broadside stripmap SAR, while the squint stripmap SAR has smaller imaging area.

Based on the description of Figure 2.5, a set of SAR-related parameters and their indicating symbols are given for contextual understanding. These parameters are classified into the six groups and each of them consists of important interrelated concepts for SAR.

1. Transmitting power P_t and equivalent isotropically radiated power (EIRP) P_e : EIRP is defined as the amount of power that a theoretical isotropic antenna would transmit, to yield the maximum energy viewed from the direction of antenna peak gain G_a [15]. It equals to $P_t G_a$ if the cable loss is neglected. The two parameters are factors to dictate the operating slant range R of SAR. EIRP P_e varies with the antenna gain G_a , which is generally pertinent to the antenna physical apertures D_a and D_e .
2. Signal bandwidth B , pulse duration t_p and grazing angle φ : the bandwidth B determines a target's slant-range resolution ΔR via equation (2.1), and the reciprocal of bandwidth

B can be much narrower than the duration t_p of a frequency or phase modulated pulse. As mentioned in Section 2.2.1, this results from the compression factor C_f by:

$$B = \frac{C_f}{t_p}. \quad (2.12)$$

On the other hand, the ground-range resolution ΔR_g can be derived via dividing ΔR by $\cos\varphi$, which is similar as the equation (2.9). Since the range and resolution parameters in ground range can be readily denoted by slant range parameters, **the slant range is briefed as range henceforth and the imaging space used in this dissertation is the slant-range plane.**

3. Aperture size L_a and antenna azimuth size D_a : these two parameters are connected to the effective cross-range or azimuth resolution ΔCR of a stripmap SAR shown in equation (2.7). However, D_a is not a decisive factor of ΔCR for other modes of SAR, since their aperture sizes L_a are not equal to the azimuth resolution of an RAR.
4. Platform velocity v , slow-time τ and azimuth position x : For the broadside stripmap SAR [8], the Doppler frequency bandwidth B_D depends on v by:

$$B_D = \frac{2v}{\lambda}\theta_x, \quad (2.13)$$

which represents the bandwidth resulting from the frequency shift of a target when it is within the antenna's azimuth 3-dB beamwidth θ_x . On the other hand, the flight time instance of the airborne platform is defined as the slow time τ , resulting in the cross-range position $x = v\tau$. Therefore, the instantaneous range R between a target and the SAR sensor can be represented as:

$$R = \sqrt{r_{pl}^2 + (x - x_{pl})^2} = \sqrt{r_{pl}^2 + v^2(\tau - \tau_{pl})^2}, \quad (2.14)$$

where r_{pl} is the distance from the target position (a point) to the straight line of the platform's flight trace. Similar as the reference range r_c in Figure 2.5, r_{pl} is the minimum distance from a target to the stripmap SAR sensor, which is perpendicular to the

platform's trace line at point x_{pl} , whose corresponding time instance is τ_{pl} . The instantaneous range R determines the transient time delay t_d by $t_d = \frac{2R}{c}$, thereby leading to the instantaneous phase delay p_d of received echo as:

$$p_d = 2\pi f t_d = \omega t_d = \frac{2\omega}{c} R = 2kR = 2k \sqrt{r_{pl}^2 + v^2(\tau - \tau_{pl})^2}, \quad (2.15)$$

where ω and k are angular frequency and wavenumber, respectively. Since the phase delay p_d is a function of azimuth time variable τ , the instantaneous cross-range frequency f_x is calculated via:

$$f_x = \frac{\partial p_d}{\partial \tau} = 2k \frac{v^2(\tau - \tau_{pl})}{\sqrt{r_{pl}^2 + v^2(\tau - \tau_{pl})^2}} = \frac{2kv^2}{R}(\tau - \tau_{pl}) = \frac{2kv^2 \cos \Theta_{pl}}{r_{pl}}(\tau - \tau_{pl}) \quad (2.16)$$

where Θ_{pl} is instantaneous deflection angle from the minimum target range r_{pl} to the instantaneous range R i.e. $\cos \Theta_{pl} = \frac{r_{pl}}{R} = \frac{r_{pl}}{\sqrt{r_{pl}^2 + v^2(\tau - \tau_{pl})^2}}$. The frequency f_x alters with slow time τ in a nonlinear manner due to R , yet it is inversely proportional to r_{pl} . Θ_{pl} is close to zero when the maximum azimuth displacement $\max[v^2(\tau - \tau_{pl})^2]$ is much lower than r_{pl} . Thus, the phase history for a target can be approximate to a chirp or LFM signal with respect to the slow time τ due to $R \approx r_{pl}$. Also, the cross-range frequency modulation (FM) rate M_x approximately equals to the constant of $\frac{2kv^2}{r_{pl}}$.

5. PRF f_{pr} and PRI t_{pr} : timing is essential for a pulsed radar system. Since the echo energy is much weaker than the energy of transmitted pulse, the echo cannot be detected if a pulse is transmitted at the same time. On the other hand, the range ambiguity would occur if the echoes of one pulse from the farthest end of range swath reaches earlier than the echoes of the next pulse from the closest end of the swath. The gap between two pulses is called the pulse repetition interval (PRI) t_{pr} , the width of range swath r_{sw} therefore determines the minimum t_{pr} . And the reciprocal of t_{pr} is the PRF f_{pr} . Given that the velocity of signal is equal to the speed of light c , the range swath with no range ambiguity can be derived by:

$$r_{sw}^{nra} = \frac{ct_{pr}}{2} = \frac{c}{2f_{pr}}. \quad (2.17)$$

Comparing r_{sw}^{nra} with the width of range swath determined by antenna's beamwidth shown in equation (2.10), the smaller value is set as the operating swath r_{sw} . On the other hand, PRF has to satisfy the azimuth sampling frequency, which should be higher than the Doppler bandwidth B_D , i.e. $f_{pr} \geq B_D = \frac{2v}{\lambda}\theta_x$. Thus, the PRF of a broadside stripmap SAR is required to satisfy this inequality:

$$\frac{2v\theta_x}{\lambda} \leq f_{pr} \leq \frac{c}{2r_{sw}}. \quad (2.18)$$

6. Pulse's range envelope w_r and its cross-range envelope w_{cr} : the range envelope w_r is a rectangular function if no weighted function is imposed on the transmitted pulse, although w_r is always define the shape to reduce sidelobe level. We use $w_r(\frac{t}{t_p})$ to represent the range envelope of a pulse with duration of t_p . However, due to the antenna's azimuth beam pattern, the pulse cross-range envelope w_{cr} is a sinc^2 -like function, varying with the instantaneous deflection angle Θ_{pl} [8], yielding:

$$w_{cr} \approx \text{sinc}^2\left(\frac{\Theta_{pl}}{\theta_x}\right). \quad (2.19)$$

Since Θ_{pl} alters with the slow time τ as mentioned before, the w_{cr} varies with τ . And $w_{cr}(\tau - \tau_{pl})$ is used to represent the cross-range envelope when the SAR sensor is located at the time instance of τ .

2.3 SAR Operating Modes and Its Imaging Algorithms

A range of currently application-driven SAR working modes are illustrated for the reader to comprehend the remainder of this dissertation. The objective and basic structure of SAR imaging algorithms are briefed, while the wavenumber domain algorithm, adopted by WiMAX SAR, is formulized in detail.

2.3.1 Primary SAR operating modes

As the ancient Greece philosopher Plato said, "Necessity, who is the mother of invention." A variety of SAR modes debut one after another, with the expansion of application requirements for remote sensing.

Since the concept of synthetic aperture radar (SAR) was first proposed by Carl Wiley in 1951, a multitude of SAR modes for different applications came forth over past six decades. Brown reconstructed the stripmap SAR imaging by optical processing [13], while Walker first proposed the spotlight SAR system in 1980 for imaging comparatively small target area with finer azimuth resolution [16]. Moore demonstrated a scanning SAR for wider slant range swath of image in the following year [17]. Around 1990s, the squint mode SAR started to gain attentions [18] for special requirements of imaging geometry.

Stripmap and spotlight modes are used for different applications. Figure 2.6 depicts these two modes, in which stripmap SAR images a long belt region while spotlight SAR improves the cross-range resolution by increasing its aperture size to be larger than L_a in Figure 2.5.

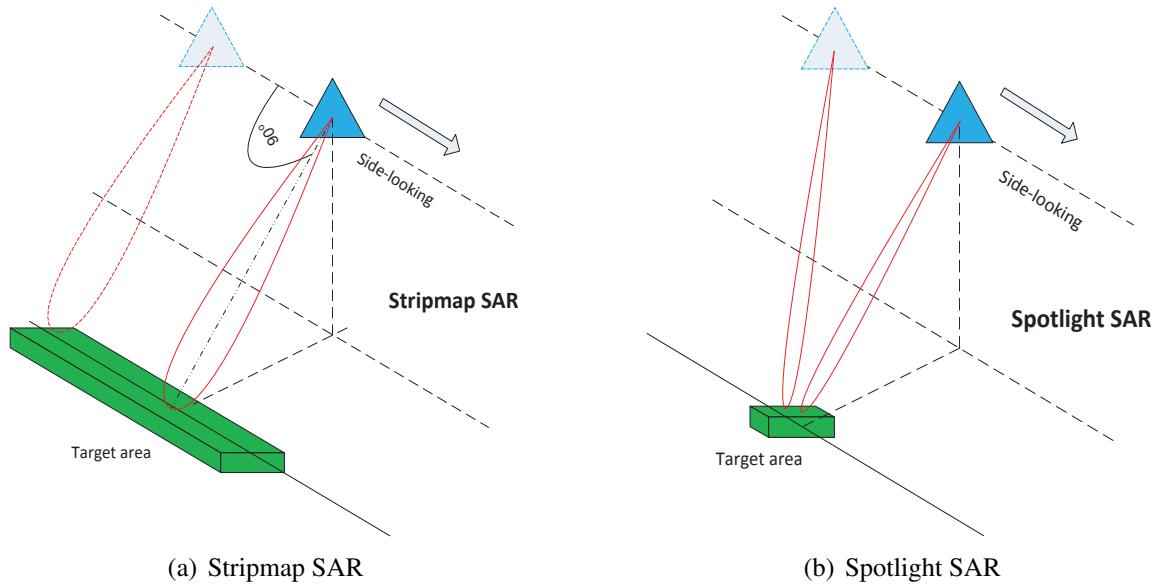


Figure 2.6: Two fundamental modes of airborne SAR.

Figure 2.6 shows beamwidth of the stripmap SAR is wider than the spotlight one. It is also worth noting that the imaging area of stripmap SAR is a strip, which could be much longer than the patch area imaged by spotlight SAR. Further, the beam direction of stripmap SAR is

fixed to be perpendicular to the flight track (broadside), whereas the beam of spotlight SAR is steered to focus on the small patch during the flight path of the SAR sensor.

These two types of SAR are of such a disparity that they are known as "forerunner" of other modes of SAR systems. Apart from the two SAR modes, we only discuss two descendant types. For acquaintance of their differences and relations, the stripmap, spotlight, scan-mode and squint-mode stripmap SAR are described with their geometries.

- **Stripmap SAR**

It is the first type of SAR, which is able to image a swath region with width of r_{sw} , while the region's length depends on the imaging area of interest. In Figure 2.7, the a_w is the

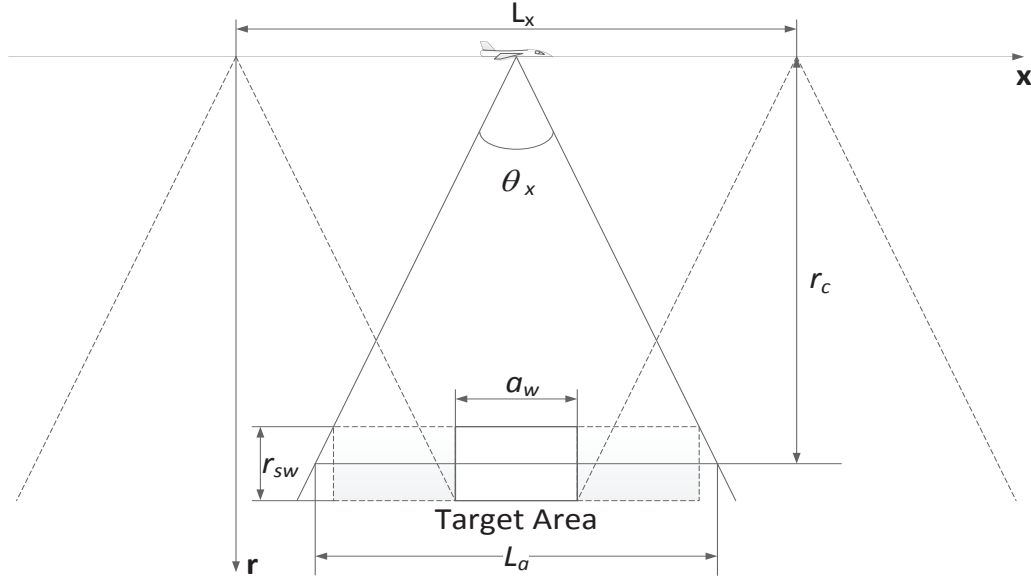


Figure 2.7: Schematic of a stripmap SAR, where L_x is the length of flight path to ensure the uniform cross-range resolution ΔCR for whole target area, while L_a is aperture size for one target with range of r_c , and a_w is the width of azimuth imaging unit.

width of azimuth imaging unit, which is usually narrower than the aperture size L_a at reference range r_c . However, in order to obtain uniform cross-range resolution within this area, the length of the flight path L_x is even larger than $L_a + a_w$. According to the equation (2.7), the cross-range resolution ΔCR of stripmap SAR is half of the antenna's azimuth size D_a , which is generally smaller than 2m. The sampling spacing, based on Nyquist sampling theorem for complex-valued signals, has to be smaller than the $\frac{D_a}{2}$,

resulting in massive number of sampling points over a long flight path L_x . For example, given $r_c = 6000\text{m}$ and operating wavelength $\lambda = 0.0517\text{m}$ while $D_a = 1\text{m}$, the aperture size $L_a \approx \frac{r_c \lambda}{D_a} \approx 310\text{m}$, according to equation (2.6). Provided that $a_w = 150\text{m}$, the number of sampling points N_m is over $\frac{L_a + a_w}{D_a/2} = 920$.

• Spotlight SAR

It requires an antenna steering controller to keep the antenna's illumination on the patch area during the whole flight time. Unlike the stripmap SAR, the target area is within

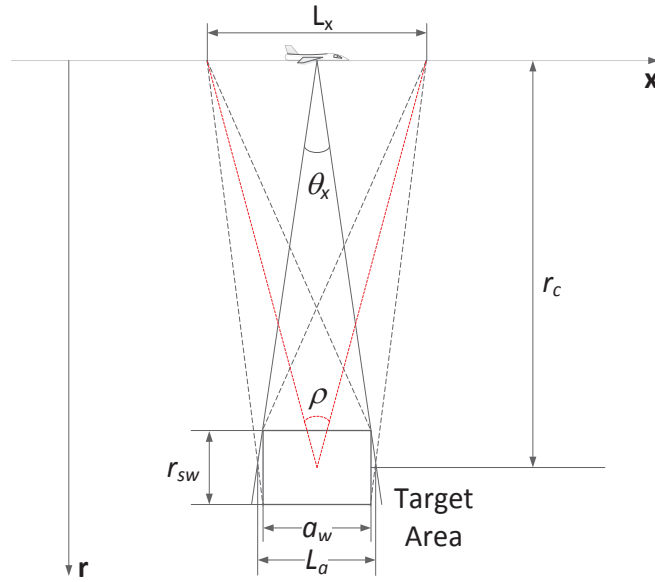


Figure 2.8: Schematic of a broadside spotlight SAR, where ρ is rotational angle of the whole flight path of SAR platform from the perspective of the target at the center of the rectangular target area.

the beam during the whole flight time, and the aperture size of spotlight SAR is equal to the length of flight path L_x rather than the aperture size of stripmap SAR denoted in equation (2.11). As shown in Figure 2.8, the angle ρ represents the rotation angle of the antenna beam during the flight path. Therefore, when ρ is small enough, the aperture size of spotlight SAR can be denoted as:

$$L_a = L_x = 2r_c \tan\left(\frac{\rho}{2}\right) \approx r_c \rho. \quad (2.20)$$

Since stripmap SAR aperture size $L_a \approx r_c \theta_x$, the aperture size of spotlight SAR L_x can

be longer than L_a on the condition:

$$\theta_x < \rho \leq \alpha_m, \quad (2.21)$$

where α_m is maximum angle allowed to be approximate to $\sin\alpha_m$ or $\tan\alpha_m$. According to equation (2.7), we can derive the cross-range resolution of spotlight SAR as:

$$\Delta CR = \frac{r_c \lambda}{2L_x} = \frac{\lambda}{2\rho}. \quad (2.22)$$

Thus, spotlight SAR can achieve better resolution if equation (2.21) is satisfied. Moreover, spotlight SAR can saves pulses to attain same azimuth resolution $\Delta CR = 0.5\text{m}$. The rotation angle is $\rho = \frac{\lambda}{2\Delta CR} = \frac{0.0517}{2 \times 0.5} = 0.0517\text{rad}$, resulting in the $L_x = r_c \rho \approx 310\text{m}$. Thus, the number of sampling points N_l is $\frac{L_x}{D_a/2} = 620$, only two-thirds of N_m .

- **Scan-mode SAR**

This type of SAR is often utilized in the spaceborne SAR systems, whose total range swath r_{sw} is too large to avoid range ambiguity if f_{pr} cannot be reduced, based on the inequality (2.18). It expands the range swath at the expense of lower cross-range resolution due to the aperture size's shrinkage for each sub-swath. It also needs an antenna steering controller to rotate the beam in elevation plane by a stepwise manner. Therefore, the controller can be a beamforming signal processor for patterning the beam direction using an array antenna at a marked fast speed [19]. Figure 2.9 only shows two sub-swaths, albeit the number of sub-swaths can be over five for spaceborne SAR [8]. The scanning period is fixed and the coverage rates for imaging scenes of different sub-swaths are same, i.e. $L_{x1} + L_{x2}\text{m}$. However, the widths of azimuth imaging unit for the two sub-swaths are different by a_{w1} and a_{w2} , since the aperture size of farther sub-swath, L_{a1} , is bigger than that of nearer sub-swath, L_{a2} .

- **Squint-mode SAR**

The squint mode can be applied into either stripmap SAR or spotlight SAR. The latter requires a continuously steering antenna whereas the former only needs fixed antenna.

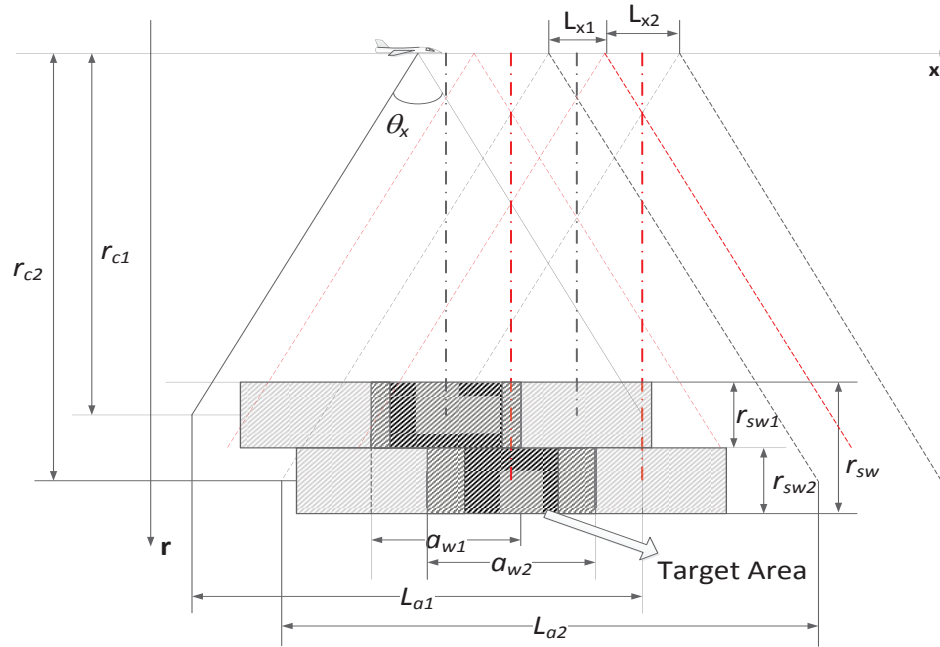


Figure 2.9: Schematic of a scan-mode SAR, in which the flight length L_{x2} is bigger than L_{x1} due to larger azimuth width a_{w2} of imaging area, corresponding to the farther range swath r_{sw2} .

Section 2.4.3 and Appendix B will discuss the azimuth resolution of the latter one. Here the squint stripmap SAR is described for the design in Chapter 5. As shown in Figure

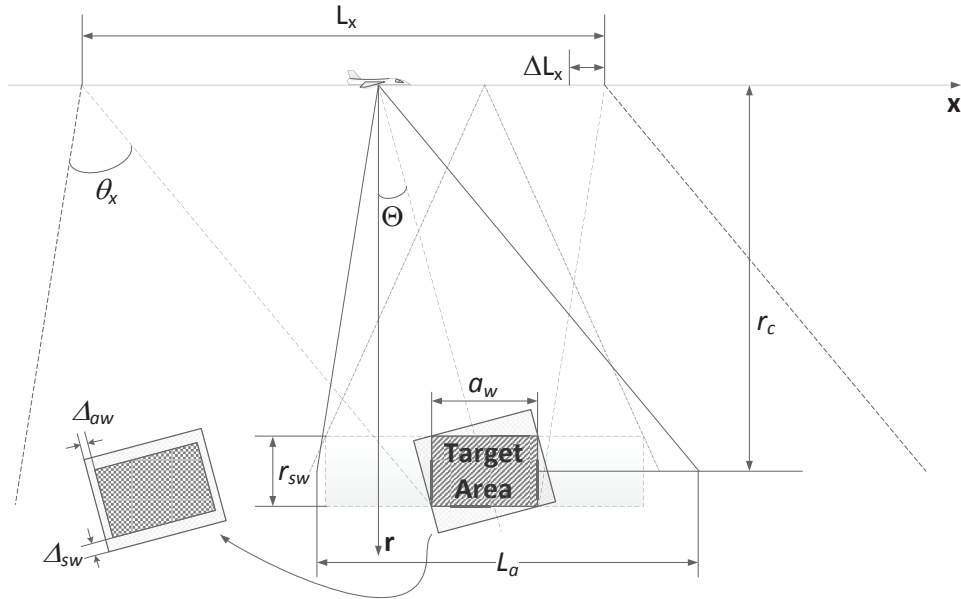


Figure 2.10: Schematic of a squint stripmap SAR. Its target area requires to be enlarged to cover the counterpart area of broadside stripmap SAR, causing flight length increased by ΔL_x .

2.10, the imaging area varies marginally from that of a broadside stripmap SAR, as long as the squint angle Θ is small enough. The imaging area of the squint stripmap SAR should be a bit larger to cover that of a broadside strip-map SAR. The increments in range Δ_{sw} and azimuth Δ_{aw} are close to $a_w \sin \Theta / 2$ and $r_{sw} \sin \Theta / 2$, respectively (see Appendix C). The expanded area can ensure same illumination region shown in Figure 2.7. Further, the ΔL_x stands for the difference of required path length between the squint and broadside stripmap SAR, which can be easily calculated by the law of cosines.

2.3.2 Wavenumber domain algorithm

As mentioned before, RAR cannot work at long distance (or high altitude) while constructing high-resolution image. However, SAR can possess both features as long as two conditions are satisfied. First, the information of adequate target returns is successfully collected by transceivers during a flight path. Secondly, an effective algorithm is used to focus the collected echo data. Intuitively, SAR imaging algorithm can synthesize a set of small (usually aligned) apertures to be a virtually much larger aperture in the sky. Therefore, a SAR algorithm is so vital that it provides an algorithm-supported "virtual antenna" with much larger aperture size for high-resolution imaging. Further, unlike RAR, different imaging algorithms dictates the hardware as well as software of the SAR system, following the down-converted received echo signal, which is therefore called raw data hereafter.

It is generally accepted that two core steps have to be implemented regardless of selected SAR algorithm. First, the raw data requires one two-dimensional (2-D) matched filter or two one-dimensional (1-D) filters for obtaining high-resolution image of targets at reference range. This step can be directly implemented in time domain, such as back projection algorithm (BPA), yet causing high workload of computation. On the contrary, the wavenumber domain algorithm, also called ΩKA , is applied in frequency domain by applying Fourier transform on raw data, gaining much more computational efficiency. Other SAR imaging algorithms could use both domains. Apart from this 2-D image compression, another key processing is to correct the errors for other targets within the imaging area. Figure 2.11 demonstrates two indispensable steps for SAR receivers. It is noteworthy the correction or focusing step does not have to

be after the compressions.

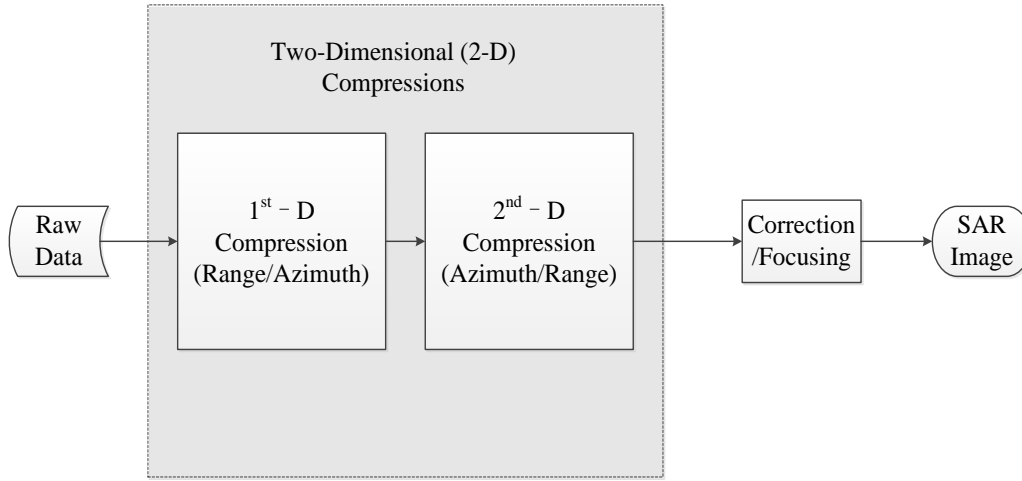


Figure 2.11: Two major steps for all SAR receivers: First is two dimensional compression for targets at reference range, while the second is algorithm-dependent correction for focusing all other targets in the imaging area.

As mentioned before, the most commonly used waveform is the LFM pulse signal. This signal was intensively exploited by two research groups from Canada and Germany respectively. The two independent teams presented a novel LFM-based SAR imaging algorithm in same conference. And then they jointly published a paper [20] and call the new algorithm chirp-scaling algorithm (CSA). Although LFM pulse is the most widely-used SAR signal in practice, other waveforms, such as nonlinear frequency modulation (NLFM) or OFDM signals, gradually drawing attentions due to unique features or ubiquitousness. Actually, most high-resolution SAR imaging algorithms are independent of the pulse shape, such as range Doppler algorithm (RDA) [8] and wavenumber domain algorithm (ΩKA) [21].

RDA only requires one-dimensional operations, increasing the efficiency. And the major image formation steps of RDA are completed in the range Doppler domain, in which the range-related parameters can be adjusted easily. Therefore, one marked advantage of RDA is its adaptability to the variation of the reference range [8]. Thus, it is preferable to be applied in spaceborne SAR systems due to the wide range swath of their imaging. However, this algorithm approximates the phase delay in equation (2.15) to be $2k\left(r_{pl} + \frac{v^2(\tau - \tau_{pl})^2}{2r_{pl}}\right)$. Although the error is much smaller than 2π when r_{pl} is much larger than $v(\tau - \tau_{pl})$, it could fundamentally affects the precision of the cross-range compression. The reason is the reference signal

for azimuth matched filtering is a chirp signal which is an approximation of the real azimuth reference signal in time domain.

By contrast, the ΩKA utilizes the complex conjugate of the real azimuth reference signal in frequency domain to effectively compress the echoes of targets located along the reference range, while the targets away from the reference range can be compressed precisely by the Stolt interpolation [8, 22, 23]. If platform velocity v is constant, the phase of echo pulse possesses the spherical feature shown in equation (2.15). The spherical signal spreads the cross-range spectrum and can be compressed by a matched filter. For ΩKA , the only azimuth modulation error is due to variation of platform velocity. For airborne SAR, the constant velocity assumption is valid as long as minor motion of the sensor caused by air turbulence is compensated sufficiently [24]. However, for spaceborne SAR, the velocity is a variable due to round surface of the earth. ΩKA algorithm has several advantages such as being independent of aperture size as well as transmission signal shape, best accuracy for airborne SAR imaging and excellent expandability for assorted SAR modes.

On the other hand, OFDM signal penetrates into currently various wireless communication systems with different operating frequency, ranging from very high frequency (VHF) to millimeter (mm) wave [25]. The operating range of these applications decreases from over 70km to around 1m with the increasing of working frequency. For most SAR applications, the operating range is over one kilometer. Therefore, the OFDM-based systems working in more than 10GHz is difficult to be applied for SAR applications due to their limited power. Since lower frequency requires larger synthetic aperture [21], ΩKA could be the first option for SAR imaging by using the COTS OFDM-based systems in microwave frequency.

The block diagram of applying ΩKA for stripmap SAR imaging is shown in Figure 2.12. The flow chart shows how the ΩKA transforms the raw data into a high-resolution SAR image, in which the blocks with dashed lines are neglected in this thesis. Interested readers can refer to [24, 26] for more detailed information. These operations, such as motion compensation (MoCo) and autofocus, are used for correcting those phase errors resulting from some non-ideal practical parameters, without altering the basic framework of the ΩKA algorithm.

The OFDM waveform, as a broadband signal, can be viewed as the direct superposition of numerous monochromatic signals due to their mutual orthogonality. Therefore, a single-

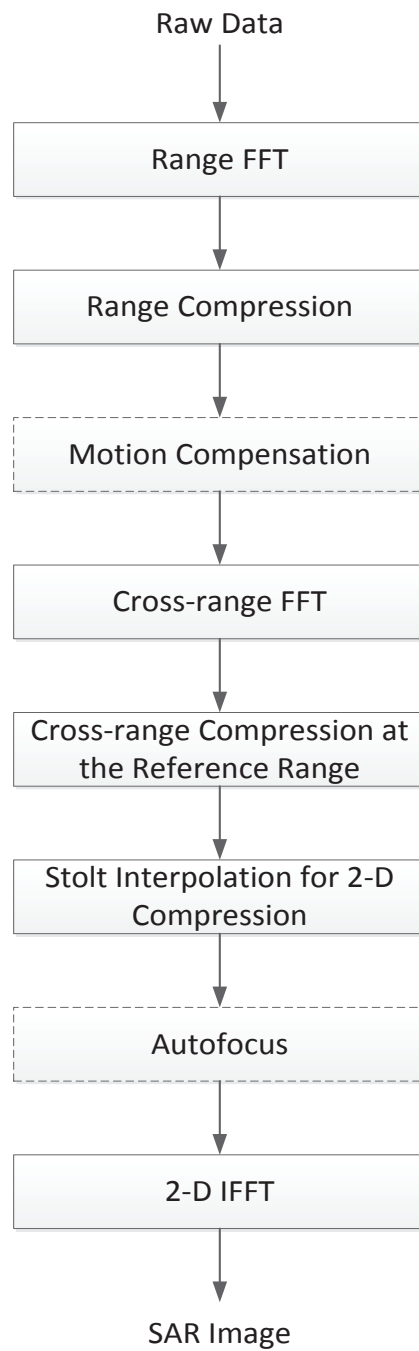


Figure 2.12: Flow chart of SAR imaging processed by ΩKA algorithm.

frequency waveform $e^{j\omega_1 t}$ is used as the transmitted baseband signal to formulize the ΩKA algorithm in accordance with the flowchart of this algorithm. The transmitted baseband SAR signal of unit amplitude is defined as:

$$s_{TX}(t) = \exp(j2\pi f_1 t) w_r \left(\frac{t}{t_p} \right) = \exp(j\omega_1 t) w_r \left(\frac{t}{t_p} \right), \quad (2.23)$$

where w_r represents the envelope shape of the monochromatic pulse with length of t_p . It is transmitted in the frequency of PRF during the flight path of the SAR sensor. Assuming a target with RCS of σ_t is located at (r_t, x_t) , the equation (2.14) becomes

$$R_t(\tau) = \sqrt{r_t^2 + (x - x_t)^2} = \sqrt{r_t^2 + v^2(\tau - \tau_t)^2}, \quad (2.24)$$

where τ_t is slow-time instance of the SAR platform of constant speed v corresponding to x_t . Thus, the received baseband signal, $s_{RX}(t, \tau)$, can be expressed as

$$\begin{aligned} s_{RX}(t, \tau) &= A_1 \sigma_t \exp \left(-j\omega_c \frac{2R_t(\tau)}{c} \right) \exp \left(j\omega_1 \left(t - \frac{2R_t(\tau)}{c} \right) \right) w_r \left(\frac{t - \frac{2R_t(\tau)}{c}}{t_p} \right) w_{cr}(\tau - \tau_t) \\ &= A_1 \sigma_t \exp(-jk_c R_t(\tau)) \exp \left(j\omega_1 \left(t - \frac{2R_t(\tau)}{c} \right) \right) w_r \left(\frac{t - \frac{2R_t(\tau)}{c}}{t_p} \right) w_{cr}(\tau - \tau_t), \end{aligned} \quad (2.25)$$

where A_1 represents a loss caused by transceivers and signal transmission media, while $\frac{2R_t(\tau)}{c}$ is the delay time of an echo from the target with slant range $R_t(\tau)$ at the slow time τ . ω_c and k_c are carrier angular frequency and wavenumber, respectively. The $s_{RX}(t, \tau)$ is the form of raw data to be processed in frequency domain by ΩKA algorithm.

Before the range compression, $s_{RX}(t, \tau)$ is required to be Fourier transformed into frequency domain of fast time. The output signal $s_{RX}(\omega, \tau)$ can be expressed as

$$\begin{aligned} s_{RX}(\omega, \tau) &= \int_{-\infty}^{\infty} s_{RX}(t, \tau) \exp(-j\omega t) dt \\ &= A_1 \sigma_t \exp \left(-j(\omega_c + \omega_1) \frac{2R_t(\tau)}{c} \right) W_r(\omega) w_{cr}(\tau - \tau_t), \end{aligned} \quad (2.26)$$

where $W_r(\omega)$ is the pulse envelope in the angular frequency domain, which depends on the pulse duration t_p and the signal frequency ω_1 , with full form of $W_r((\omega - \omega_1)t_p)$. The $s_{RX}(\omega, \tau)$

is followed by the range matched filtering in frequency domain, yielding

$$s_{c1}(\omega, \tau) = A_1 \sigma_t \exp\left(-j(\omega_c + \omega_1) \frac{2(R_t(\tau) - r_c)}{c}\right) W_r(\omega) W_{cr}(\tau - \tau_t), \quad (2.27)$$

where the r_c is the reference range for the imaging swath shown in Figure 2.5. Since the airborne platform's velocity v can be assumed to be a constant, x is used to denote the discrete azimuth position $v\tau$ for brevity. Then the instantaneous target range can be denoted as $R_t(x)$. It is denoted by azimuth position x via this equation:

$$R_t(\tau) = \sqrt{r_t^2 + (x - x_t)^2} \quad (2.28)$$

Thus, the range-compressed signal can be expressed as:

$$s_{c1}(\omega, x) = A_1 \sigma_t \exp\left(-j(\omega_c + \omega_1) \frac{2(R_t(x) - r_c)}{c}\right) W_r(\omega) W_{cr}(x - x_t). \quad (2.29)$$

According to the diagram, the $s_{c1}(\omega, x)$ will be Fourier transformed. But the result is better to be represented in the cross-range wavenumber domain. By applying the method of stationary phase (MSP) (see Appendix A), the nonlinear signal $s_{c1}(\omega, x)$ in wavenumber domain is

$$\begin{aligned} S_{c1}(\omega, k_x) &= \int_{-\infty}^{\infty} s_{c1}(\omega, x) \exp(-jk_x x) dx \\ &= \sigma_t A_1 \int_{-\infty}^{\infty} [\exp(-j2k(R_t(x) - j2kr_c)) W_r(\omega) W_{cr}(x - x_t)] \exp(-jk_x x) dx \quad (2.30) \\ &= \sigma_t A_1 A_2 \exp\left(-j(\sqrt{4k^2 - k_x^2} r_t + k_x x_t) + j2kr_c - j\frac{\pi}{4}\right) W_r(\omega) W_{cr}(k_x), \end{aligned}$$

where k is the fast-time wavenumber, which is the sum of carrier wavenumber k_c and signal wavenumber k_1 , while k_x is the slow-time wavenumber. The W_{cr} stands for the cross-range envelope in the slow-time wavenumber domain. A_2 and $-\frac{\pi}{4}$ represent the radical expression and the extra phase shift shown in the equation (A.9) of Appendix A.

In order to focus those targets at the range of r_c , the $S_{c1}(\omega, k_x)$ can be multiplied by a reference function f_R :

$$f_R = \exp(\sqrt{4k^2 - k_x^2} r_c - j2kr_c + j\frac{\pi}{4}). \quad (2.31)$$

This yields the compressed signal $S_{c2}(\omega, k_x)$:

$$S_{c2}(\omega, k_x) = S_{c1}(\omega, k_x) f_R = \sigma_t A_1 A_2 \exp \left(-j \left(\sqrt{4k^2 - k_x^2} (r_t - r_c) + k_x x_t \right) \right) W_r(\omega) W_{cr}(k_x). \quad (2.32)$$

Equation (2.32) shows that when the range of target r_t equals to r_c , its cross-range position x_t can be directly obtained by applying inverse Fourier transform (IFT) into the $\omega - k$ domain compression signal $S_{c2}(\omega, k_x)$. However, for those targets at ranges different from r_c , their range information $(r_t - r_c)$ cannot be extracted directly by imposing IFT on the non-linear phase $\exp \left(-j \left(\sqrt{4k^2 - k_x^2} (r_t - r_c) \right) \right)$. In order to implement IFT, an operator, called Stolt interpolation, is used to map the square-root coefficient $\sqrt{4k^2 - k_x^2}$ into the linear coefficient k_r in fast-time wavenumber domain, which yields:

$$S_{c2}(\omega, k_x) = \sigma_t A_1 A_2 \exp \left(-j (k_r (r_t - r_c) + k_x x_t) \right) W_r(\omega) W_{cr}(k_x), \quad (2.33)$$

where $k_r = \sqrt{(2k)^2 - k_x^2} = \sqrt{\left(\frac{2(\omega_c + \omega_1)}{c} \right)^2 - k_x^2}$ is called the Stolt interpolation from ω to k_r [23].

Eventually, the $\omega - k$ domain data is ready-made to be executed a two-dimensional (2-D) or two one-dimensional (1-D) IFT for reconstructing the final SAR image.

The Stolt interpolation is able to correct the residual range cell migration compensation (RCMC), remaining azimuth compression and residual second range compression (SRC) at the same time [8], as long as the assumption of constant platform velocity is valid. With effective MoCo, the speed can be regarded as a constant for airborne SAR systems.

2.4 Airborne SAR and Broadband Wireless Technologies

2.4.1 Current airborne SAR applications

SAR imaging provides a wealth of applications. It was first mounted on a warplane and used for military targeting, airborne warning, surveillance and reconnaissance under the day-and-night as well as all-weather conditions. Since 1978, the spaceborne SAR, mounted on a satellite, came out for civilian remote sensing of the earth surface, including forest, agriculture, ocean, ice, snow and so forth [27]. During the same period, airborne SAR did not slacken its pace

and it still played a role of vanguard in SAR field. Contemporary SAR sensors aim at offering robust SAR imaging with the similar level of resolution as that of optical imaging on one hand, and lowering the cost by cutting-edge technologies on the other hand [28].

Airborne SAR is still attractive due to its adaptability for flexible applications. NASA once launched a project of SAR2, which is the abbreviation of search and rescue synthetic aperture radar. With the aid of the AirSAR (an airborne SAR system), this project aims at search man-made large vehicle, especially the downed airplane [29]. Recently, the low-cost and light-weight airborne SAR arose a growing interests with the rapid development of UAS. A research team from Brigham Young University (BYU) has developed a series of light-weight airborne micro-SAR systems, in which the C-band MicroASAR is a robust and self-contained SAR system for diversified applications [30]. Since it utilizes continuous LFM waveform, the transmitter and receiver can operate at the same time. This improves the power efficiency, whereas requires more mixers and band pass filters to remove the low-frequency interference from the feedthrough components, which is used for isolation between transmitter and receiver antennas.

Considering the high cost of airborne SAR systems and low-cost COTS WiMAX devices in unlicensed band, we attempt to utilize WiMAX base stations for SAR imaging in the remainder of the thesis.

2.4.2 WiMAX and other OFDM-based wireless systems

This subsection first introduces OFDM technique. Afterwards, a brief description of WiMAX and other OFDM-based broadband wireless systems is given before a technical comparison between WiMAX and SAR.

OFDM is an efficient multi-carrier modulation technique, which was first officially proposed by Chang in 1966 [31]. However, this system requires an array of local oscillators (LO) to generate and coherently receive a mass of narrow-band sinusoidal waves, causing unaffordable high cost and complexity for the system implementation. This concept did not arise much attentions until 1971, in which Weinstein proposed to use fast Fourier transform (FFT) as well as inverse fast Fourier transform (IFFT) for accomplishing modulation and demodulation of

the OFDM system, paving a way for digitalizing OFDM systems.

The basic OFDM system diagram is shown in Figure 2.13. For the transmitter, the binary

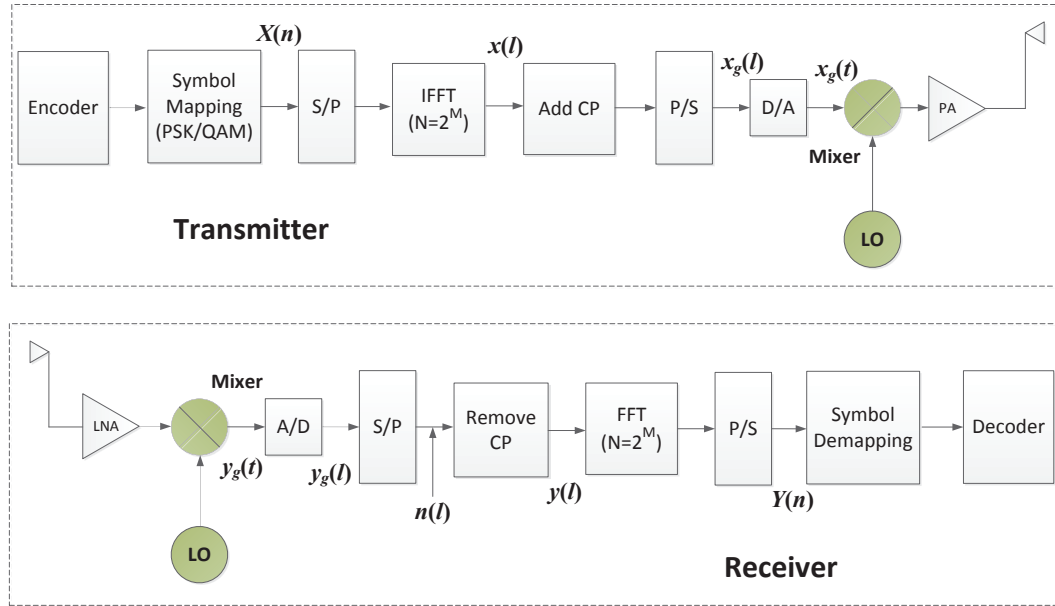


Figure 2.13: Basic diagram of a generally-accepted OFDM system.

data is first encoded for two major purposes: one is to compress and optimize the transmitted binary data by source coding, while the other is to lower the negative wireless channel effects, such as multi-path and shadowing, by channel coding. The coded data is then mapped into a form to be transmitted effectively by a digital modulation scheme, such as phase shift keying (PSK) or quadrature amplitude modulation (QAM). Once the modulated data $X(n)$ is obtained, it is converted from serial to parallel form for IFFT transformation. IFFT alters the data to be the paralleled narrow-band bit streams in time domain $x(l)$, which are split by the length of a useful OFDM symbol. After a cyclic prefix (CP) is inserted to each useful OFDM symbol, the data is converted to the data sequence $x_g(l)$ by a parallel-to-serial converter (P/S). The serial data is then transformed into analog signal $x_g(t)$ by the digital-to-analog converter (D/A). The baseband analog signal $x_g(t)$ is up-converted to the microwave LO frequency by a mixer, followed by the power amplifier (PA) before it propagates in the free space via an antenna.

At the receiver end, an antenna, together with a low-noise amplifier (LNA), receives and amplifies the attenuated and distorted microwave signal. Down-converted by the mixer with the same LO frequency, the analog received signal $y_g(t)$ is sampled and quantified to be the base-

band digital signal $y_g(l)$ by the analog-to-digital converter (A/D). The time-domain sequence is paralleled by the serial-to-parallel converter (S/P) and its CP part is removed, producing the bits streams ready for FFT. The parallel data is transformed to the digitally frequency domain by FFT before being converted to serial data $Y(n)$ by the P/S. Once the data is de-mapped with the aid of channel estimation, it is decoded to extract the digital information transmitted from the sender, thereby completing the process of communication.

The OFDM signal possesses several attractive features for radar applications. Firstly, the slow paralleled bit streams, due to numerous orthogonal subcarriers with narrow frequency band, simplify the hardware integration while provide a stable radar signal. Moreover, the FFT operation is simply to be implemented for SAR imaging in frequency domain. Further, its nearly rectangular frequency spectrum with a large number of subcarriers produces high spectrum efficiency for radar range resolution. On the other hand, the OFDM signal also suffers from weak points such as the effect of high peak-to-average power ratio (PAPR). The high PAPR requires the PA to have large linear range for suppressing power leakage and keeping performance. On the other hand, since the EIRP is restricted in unlicensed band by Federal Communications Commission (FCC), the maximum EIRP of OFDM wireless system is further limited by the large PAPR-caused power fluctuation. More detailed advantages and challenges will be discussed later in this thesis.

WiMAX is a popular wireless metropolitan area network (WirelessMAN). Its base station can cover up to 50km radial range and it is applied to mobile service, as the only competitor with the long term evolution (LTE) for 4G mobile communication. WiMAX Forum [32] reported that up to February of 2011, there had been 582 fixed and mobile WiMAX systems deployed over 149 countries. The growing popularity of WiMAX systems lowers its price years after year. Also, it adopts widely-endorsed OFDM multicarrier modulation technology, whose robustness for broadband application makes it a candidate waveform for SAR imaging. Based on current IEEE802.16 standard [33], WiMAX has two types of physical layers (PHY), i.e. WirelessMAN OFDM PHY and WirelessMAN OFDMA PHY, where OFDMA stands for orthogonal frequency-division multiple access. The two PHYs are for licensed fixed and mobile wireless communications, respectively. Their bandwidth range from 1.25MHz to 28MHz. The OFDMA PHY uses the subchannelization to improve power efficiency for mobile users

yet increasing the system complexity. Without the need to consider the power management, WiMAX SAR prefers to utilize the OFDM PHY for simplicity. More reasons for selecting OFDM PHY will be shown in Chapter 3.

It is also worth noting that the OFDM PHY of unlicensed bands, defined in the wireless high-speed unlicensed metropolitan area network (WirelessHUMAN), is similar to WirelessMAN OFDM PHY, whereas it is assigned with 256 subcarriers to share the bandwidth up to 20MHz. The unlicensed WiMAX base stations are able to work in the 5.8GHz license-exempt frequency band, which belongs to the worldwide industrial, scientific and medical (ISM) radio band between 5.725 and 5.875GHz. Unlike 2.45GHz ISM band crowded by many wireless users, there are fewer interference sources in 5.8GHz ISM band. Further, this ISM band pertains to the C-band of the radar spectrum, which is widely used for SAR imaging.

As we know, the basic DSP unit for OFDM signal is a symbol. However, to match the interface of the upper data link layer, the data transmission and reception in PHY is measured in frames. In the time division duplexing (TDD) mode, the bandwidth of OFDM signal is relatively big and it transmits and receives signal alternately, which consists of a downlink (DL) subframe and an uplink (UL) subframe. For a WiMAX base station, the signal is transmitted in the DL subframe while it is received during the UL subframe. It is noteworthy that the DL subframe contains symbols with other functionalities apart from data symbols. For instance, the preamble symbols, only using even subcarriers, are always used for synchronization. Figure 2.14 shows the structure of a DL subframe, where the first three symbols have different number of subcarriers from the data symbols. For maximizing bandwidth, it is preferable not to selected these special symbols as transmitted pulses for SAR. Similar as WiMAX, LTE and

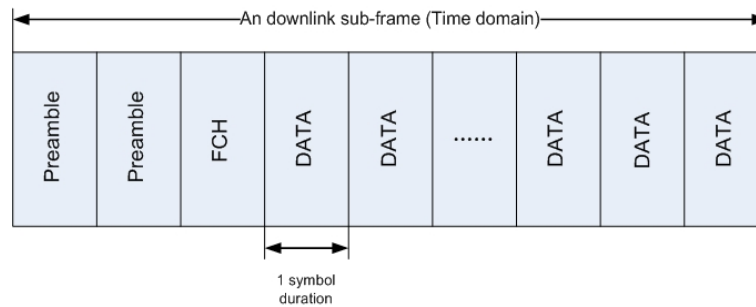


Figure 2.14: Downlink subframe structure of WirelessMAN OFDM PHY for WiMAX base station in TDD mode.

the wireless fidelity (WiFi) are popular OFDM-based wireless techniques as well. However, targeting different requirements of users, their system parameters identify themselves from WiMAX. Compared with WiMAX system, the parameters for LTE or WiFi are not preferable for SAR imaging.

To begin with, the LTE, which is the fourth generation of mobile telecommunication technology (4G), is oriented to mobile services. To balance the interchannel interference (ICI) among different mobile users and network capacity, the subcarrier spacing is set fixed as 60kHz for 20MHz bandwidth, which is still lower than the spacing of unlicensed WiMAX OFDM-PHY of 90kHz. Unlike the DL transmission adopting OFDMA technique, the UL transmission of LTE adopts a novel technology, named single carrier frequency division multiple access (SC-FDMA), to lower the PAPR for the signal transmitted from mobile users. Thus, an LTE base station utilizes different techniques and signal forms in transmission and reception. This asymmetrical feature is more suitable for frequency division duplexing (FDD) mode wireless communications. It is not appropriate for monostatic SAR since the received echo is still OFDM waveform rather than SC-FDMA pattern. Further, the operation frequency bands of LTE are below 2.62GHz and its products in unlicensed band are rare. Therefore, the SAR system using LTE devices could cause severe interference problems and high cost.

According to current IEEE 802.11 standard [34], the default CP duration of an OFDM symbol for WiFi technology is only $0.8\mu s$, which is a sufficient guard interval for wireless local area network (WLAN) of 150m operating radius. However, we will show it is too short for SAR applications. Moreover, WiFi products are only deployed in unlicensed band and their EIRP is restricted to be lower than 10W regulated by most regions over the world. For a SAR system using the power-limited WiFi devices, the range cannot be further expanded even if the SAR is working in a remote area, which is free from above-mentioned industrial regulations.

By above description, Table 2.1 compares WiMAX with WiFi and LTE considering three facets for SAR application, in which we can see WiMAX is the best choice, owing to its uniform OFDM transceiver, longer CP and ubiquity.

Table 2.1: System parameters comparison among LTE, WiFi and WiMAX

Wireless base station transceivers	Same access technology for transmitter and receiver	Availability in 5.8GHz ISM band	CP length
LTE	NO (OFDMA transmitter and SC-FDMA receiver)	Rare	$4.69 \mu s$
WiFi (802.11a - 20MHz)	YES (OFDM Transceivers)	Widespread	0.8 or $1.6 \mu s$
WiMAX	YES (OFDM or OFDMA Transceivers)	Widespread	$\frac{100}{9} \mu s$ (OFDM transceiver)

2.4.3 Similarities between SAR and WiMAX

- Signal Bandwidth

As mentioned before, the resolutions for SAR is composed of two kinds: one is range resolution ΔR ; the other is cross range resolution ΔCR . The formulae for these resolutions of two basic SAR modes (stripmap and spotlight) are illustrated in Table 2.2 [21], where the B is the signal bandwidth, while D_a represents the azimuth aperture size of the physical antenna. The flight length is fixed as L_x , while L_a is the aperture size of stripmap SAR. Θ is the antenna's squint angle with respect to broadside, and r_c is the reference range. Again, λ is operating wavelength and c is the speed of light. As shown in Figure 2.8, most spotlight SAR directs its antenna to the broadside, resulting its cross-range resolution ΔCR shown in equation (2.22). However, ΔCR of squint spotlight SAR also depends on the antenna's squint angle Θ described in the Table 2.2, according to the equation (B.2) of Appendix B. For the same L_x , it is clear the squint angle worsens the azimuth resolution of spotlight SAR. As shown in Table 2.2, the range resolutions ΔR for both modes depend on the bandwidth B of the transmitted signal, while the cross-range resolution ΔCR for any SAR mode depends on the length of the flight path L_x rather than the signal features. Soumekh [21] detailed how to use the concept of matched filter to

Table 2.2: Range and cross-range resolutions for SAR of two basic modes

SAR mode	Range Resolution	Cross Range Resolution
Stripmap	$\Delta R = \frac{c}{2B}$	$\Delta CR = \frac{R\lambda}{2L_a} = \frac{D_a}{2}$
Spotlight	$\Delta R = \frac{c}{2B}$	$\Delta CR = \frac{r_c \lambda}{2L_x \cos^2 \Theta}$

extract the cross-range information in a DSP way by transmitting narrow-band single-carrier sinusoidal pulses. And Garmatyuk [2] showed the cross-range SAR imaging by using the OFDM waveform as transmitted signal. For most of current airborne SAR sensors, ΔR and ΔCR are generally lower than 50m and 2m respectively.

For the physical layer of WiMAX, the maximum bandwidth of both OFDM PHY and OFDMA PHY is 28MHz. However, it is much more cost-effective for WiMAX SAR to use the unlicensed frequency bands. For unlicensed bands, OFDM PHY uses 256 subcarriers and OFDMA PHY uses 2048 subcarriers. These parameters are defined in the WirelessHUMAN, whose physical layer is similar to its licensed correspondence. Since the bandwidth in unlicensed band can only be 10MHz or 20MHz, the maximum viable bandwidth $B = 20\text{MHz}$. This bandwidth can support the theoretical range resolution to be 7.5m by the equation in Table 2.2, while the length of an airplane or a vessel is generally over 30m. These targets therefore can be resolved by using WiMAX signal.

As mentioned before, WiMAX transmits data or signaling in the basic unit of a frame, which is divided into DL and UL subframes for the TDD mode. As shown in Figure 2.14, a DL subframe is composed of many symbols. Certainly, it increases the throughput and efficiency to transmit symbols continuously. However, it could cause difficulty in the receiver of a monostatic radar, which will be discussed in Section 3.2. Thus, we first only reserve one symbol while nullify other symbols in a DL subframe.

For a symbol of WiMAX OFDM PHY (256 subcarriers), the power strength of guard or pilot subcarriers are different from that of data subcarriers. For example, the power in guard subcarriers is zero. To show the extreme performance of the SAR based on unlicensed WiMAX OFDM PHY, we assume the power of WiMAX device can be redefined by software. In simulation we set the all subcarriers of the useful symbol and the CP

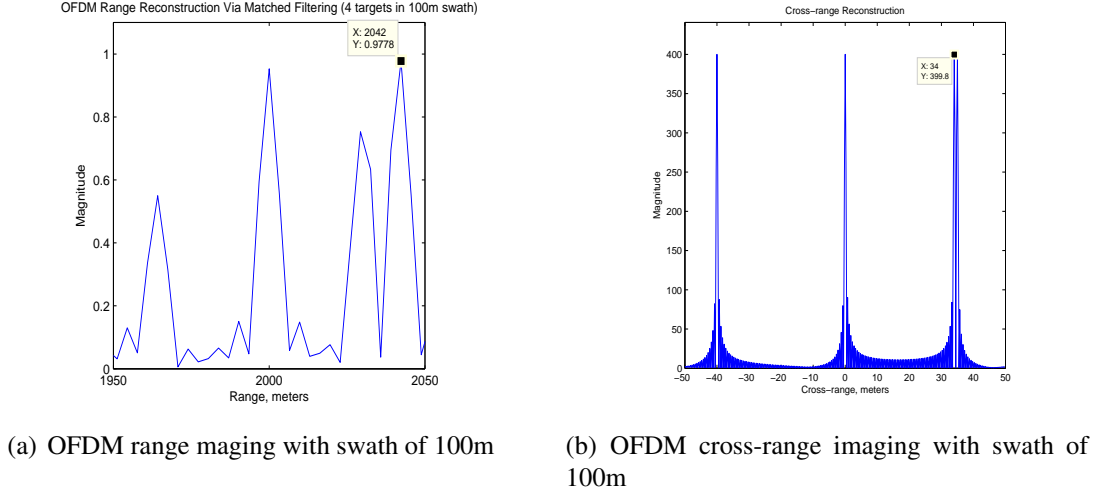


Figure 2.15: Range and cross-range imaging with resolution of 7.5m and 0.5m, respectively.

share same power level in order to obtain the optima of range resolution and operation range. Thus, an OFDM symbol, with 256 data subcarriers and 64 CP guard subcarriers, is used as the transmitted pulse.

Figure 2.15 (a) shows the simulation results of range imaging by using OFDM symbol pulses, in which four targets locate at 1965m, 2000m, 2030m and 2040m, respectively in range direction. In simulation, B is 20 MHz, yielding $\Delta R = 7.5\text{m}$. As shown in the Figure 2.15 (a), this range resolution can distinguish the target located at 2030m from the one at 2040m, yet failing to present their accurate positions (2042m), due to the quantization error of the digital processing.

Figure 2.15 (b) shows the simulation results of cross-range imaging by OFDM symbols in spotlight mode, in which four targets locate at -40m, 0m, 34m and 35m over cross range. Given $L_x = 100\text{m}$, $r_n = 2000$, $\lambda = 0.05\text{m}$, $\cos\Theta = 0$, we have ΔCR is 0.5m, based on the equation in Table 2.2. Thanks to its fine resolution, the 34m-target is distinguished from 35m-target and their cross-range position is precisely detected.

Thus, the range and azimuth information of targets can be acquired by using OFDM symbols, defined in the OFDM PHY of WirelessHUMAN, as transmitted pulses. The finest range resolution limit is 7.5m, if the transmitted pulse is the OFDM symbol, with 256 subcarriers of equal-strength. On the other hand, the cross-range resolution could be

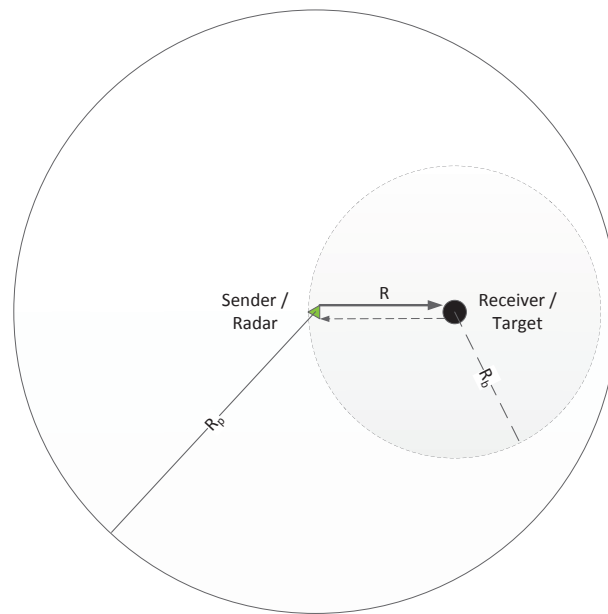
much finer by choosing different antenna size or SAR mode. However, the unequal resolutions can be accepted since the interpretability of SAR image composed of rectangular pixels is similar as that of square pixels for various targets [35].

- Transmitted Power

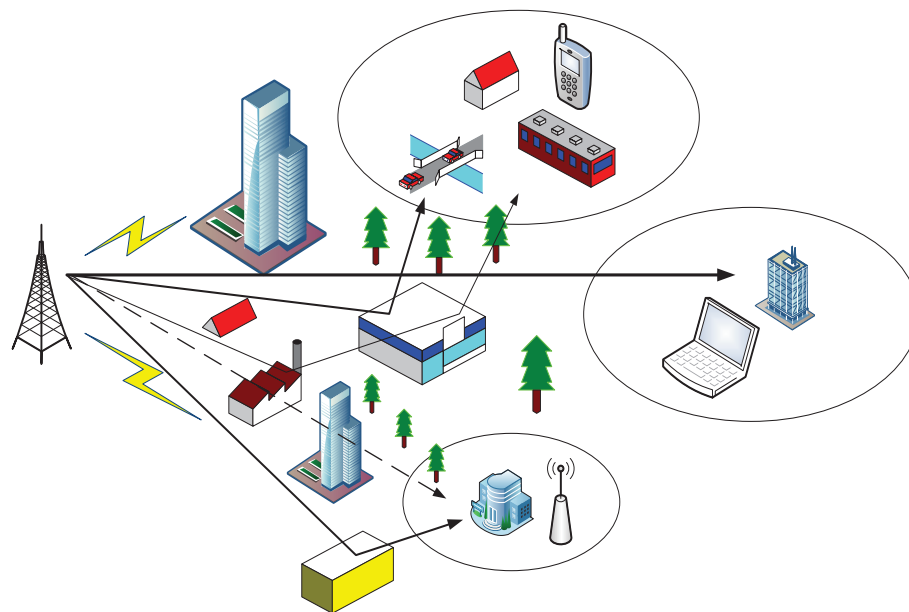
The energy of received echo for a radar system could be much weaker than the received signal energy for a wireless system for the same operating range if the microwave radiation propagates in the line-of-sight (LOS). It is because the path loss for the radar is the square of that for the wireless system in this case. Figure 2.16 (a) illustrates the different modes of signal propagation in free space for these two systems, where the green triangle is the sender or radar and the black circle is the receiver or target. Also, R represents the range between a transmitter and a receiver or a target, while R_p and R_b stand for the operating radius of the transmission signal and the backscattered echo, respectively. Since the signal for a monostatic radar propagates a round trip, its loss is related to the biquadrate of the target's range and depends on RCS of the target, while the loss for a wireless system is only in proportion to the square of the receiver's range.

However, in most situations, the wireless channel is non-line-of-sight (NLOS) due to the obstruction from crowded artificial or natural obstacles. As shown in Figure 2.16 (b), apart from the free path loss, the transmitted wireless signal may also encounter loss from multipath or shadowing effects during its propagation to the recipient. We can see the fixed access points, for WLAN or WirelessMAN, are generally located in buildings, while the mobile client premises equipment (CPE), like cell phones, can be inside the moving vehicles or trains. It is evident the transmission loss of LOS propagation (the heaviest solid line) is much less than those suffered from shadowing (dashed line), multiple scatterings as well as the Doppler effect.

Compared with base station, the CPE is more power-constrained. Thus, the uplink (UL) restricts the operation range due to its limited link budget. It is shown that the operation range of a cell for a WiMAX CPE indoor is only 1.5km for a suburban environment [36]. Since the wireless signal of NLOS propagation attenuates much more than that of LOS propagation, IEEE802.16 standard [33] regulates the maximum transmitted power



(a) Line of sight (LOS) channels for wireless and radar



(b) Non-line of sight (NLOS) channel of wireless communications

Figure 2.16: Channels comparison between radar and wireless communications

(output of power amplifier) to be 63.5dBm, which is over 2kW. Together with available WiMAX directional antenna, this power meets the requirements of most radar system.

Since the gain by post signal processing of RAR could be much lower than SAR, we first calculate the range for RAR using a licensed WiMAX base station as the transmitter, which can show how far a WiMAX base station can support for RAR application. Some

Table 2.3: Link Budget parameters for WiMAX

Parameter	Acronym
Effective Isotropic Radiated Power	P_e
Isotropic Receive Level	IRL
Receiver Sensitivity	P_r
System Gain	G_{sys}
Total Margin Loss	M_{tot}
Maximum Allowable Path Loss	MAPL
Free Space Path Loss	L_{fs}
Bandwidth	B
Transmit Antenna Gain	G_{ta}
Receive Antenna Gain	G_{ra}

key variables are shown in Table 2.3, while a link budget example shown in Table 2.4 is for outdoor mobile, considering both downlink and uplink sides [36]. The antenna's

Table 2.4: A sample link budget parameters for WiMAX

Parameter	Downlink(BS)	Uplink(SS/MS)
$G_{ta}(\text{dB})$	17	0
$P_e(\text{dBm})$	55	30
$G_{ra}(\text{dB})$	-1	18
$P_r(\text{dBm})$	-107	-109
IRL(dBm) ($=P_r - G_{ra}$)	-106	-127
$G_{sys}(\text{dB})$ ($=P_e - \text{IRL}$)	161	157
$M_{tot}(\text{dB})$	17	17
MAPL(dB) ($=G_{sys} - M_{tot}$)	144	140

noise temperature T depends on many factors such as the direction of antenna, rain, sea wave, and even the wind [37]. For simplicity, we just take the antenna direction into account. It is demonstrated that T ranges from 50K to 100K if antenna pointing to horizontal direction while around 290K if antenna vertically pointing to the earth. For the airborne radar application, the grazing angle has to be lower than 90 degree, resulting in

$T < 290K$. Even assuming the worst case, the noise temperature of receiver antenna is $T=290K$. The PSD of the noise is $\frac{N_0}{2} = kT = 4 \times 10^{-21} = -204dBW/Hz = -174dBm/Hz$, where k is the Boltzmann's constant ($\approx 1.38 \times 10^{-23} J/K$). In order to obtain the noise

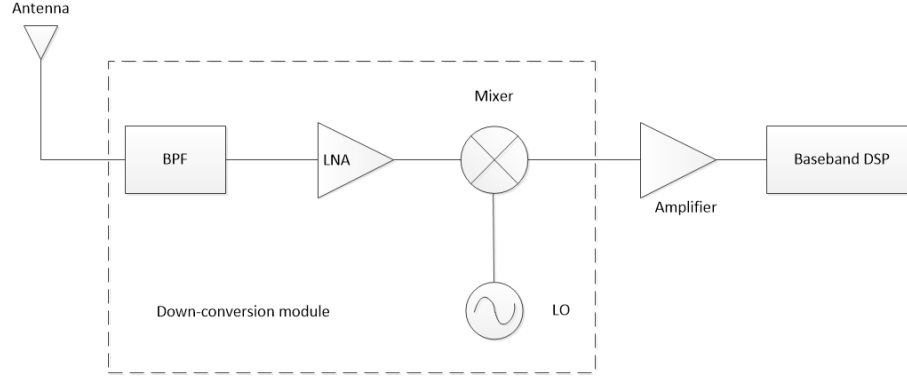


Figure 2.17: Radio frequency (RF) block diagram of a WiMAX receiver

power before baseband DSP, the receiver noise figure F_n and receiver bandwidth B are required to be taken into consideration. Figure 2.17 shows the structure of RF module of WiMAX receiver, in which a down-conversion module consists of a bandpass filter (BPF), an LNA, a mixer and an LO. The LNA and mixer both can produce additive noise. The receiver may contain several down-conversion modules before baseband signal processing, but the receiver noise figure is mainly contributed by the noise figure F_n of first LNA in the first down-conversion module. Although many simulation results showed the F_n of LNA can be as low as 1.9 dB below 7GHz, the author [38] verified F_n can be as low as 4dB at 6GHz by a practical measurement. It is common to see the F_n of a commercial WiMAX product in 3.5GHz licensed band is 5dB [39].

Given the bandwidth B of 20MHz, and receiver noise figure of 5dB, and input SNR (SNR_{in}) of 2dB, the receiver sensitivity can be calculated as below [36].

$$P_r = N_0/2 + 10\log_{10}B + F_n + SNR = -174 + 73 + 5 + 2 = -94dBm. \quad (2.34)$$

The bandwidth B for Table 2.4 is 1MHz, so the receiver sensitivity is 109dB. Based on equation (2.34) and Table 2.4, if the WiMAX base station is used as the hardware of WiMAX SAR, the isotropic receive level (IRL) is $P_r - G_{ra} = -112dBm$, since G_{ra} of base

station is 18 dB. Neglecting the margin loss M_{tot} caused by signal's NLOS transmission, the maximum allowable path loss (MAPL) equals to the system gain G_{sys} , which is $P_e - IRL = 167\text{dB}$. Many books [6–8, 14] show the radar function as,

$$SNR = \frac{P_t G_{ta} G_{ra} \lambda^2 \sigma}{(4\pi)^3 R^4 k T B F_n L_t} = \frac{P_t G_{ta} G_{ra} \lambda^2 \sigma}{(4\pi)^3 R^4 P_N L_t}, \quad (2.35)$$

where P_N is receiver noise power, which is equal to $k T B F_n$, while the loss of transmission line L_t is neglected here. R is the range, σ is the RCS of a target, and λ is the wavelength. Thus, the receiver sensitivity P_r can be represented as,

$$P_r = SNR \cdot P_N = P_t G_{ta} \cdot \left(\frac{1}{4\pi R^2}\right)^2 \cdot \sigma \cdot \frac{G_{ra} \lambda^2}{4\pi} = P_e L_{fs} \sigma \frac{G_{ra} \lambda^2}{4\pi} = P_e L_{fs} \sigma A_{eff}, \quad (2.36)$$

where $\left(\frac{1}{4\pi R^2}\right)^2$ denotes the free space path loss L_{fs} , while $\frac{G_{ra} \lambda^2}{4\pi}$ represents the effective receiver antenna area A_{eff} . Apart from L_{fs} in the round-trip path, the RCS σ , the wavelength λ and a constant $\frac{1}{4\pi}$ contribute the MAPL, i.e. $MAPL = \frac{P_t G_{ta} G_{ra}}{P_r}$ which can be denoted in logarithmic form as,

$$MAPL_{dB} = 10 \log_{10} \frac{P_t G_{ta} G_{ra}}{P_r} = 10 \log_{10} \frac{64\pi^3 R^4}{\sigma \cdot \lambda^2} = 167\text{dB}. \quad (2.37)$$

If σ of a plane is 10000m^2 and the carrier frequency is 5.8GHz, which yields $\lambda \approx 0.0517\text{m}$, the achievable range for an RAR is $R_{RAR} = 10^{\frac{167+10\log_{10}\sigma+20\log_{10}\lambda-30\log_{10}4\pi}{40}} \approx 5.1\text{km}$.

However, if $P_t = 63.5\text{dBm}$ and $G_{ta} = 31.5\text{dBi}$, the EIRP is equal to $P_e = 63.5 + 31.5 = 95\text{dBm}$, 40dB larger than that given in Table 2.4. In this case, to work in the same range, the σ can be as low as 1m^2 , which is generally the RCS of a person. Therefore, using WiMAX base station and directional antenna, the working range of a real aperture radar (RAR) can be as large as several kilometers.

- Pulse Repetition Frequency

As shown in Table 2.2, ΔCR counts on the length of flight path L_x . As the sampling frequency for slow-time processing, the PRF has to be bigger than the Doppler frequency bandwidth B_D to obtain the ΔCR . According to IEEE802.16, the minimum frame dura-

tion of WirelessHUMAN is 5ms. leading to f_{pr} of 200Hz.

According to equation (2.18), the equation $f_{pr} \geq \frac{2v\theta_x}{\lambda}$ can be satisfied as long as the platform velocity v or the antenna's angular 3-dB beamwidth θ_x is small enough. For example, given $\lambda = 0.0517\text{m}$, $\theta_x = \frac{\pi}{60}\text{rad}$ (using a high-gain antenna), and $v = 50\text{m/s}$ (e.g. speed of a UAS), we can derive $B_D \approx 101.3\text{Hz}$ by equation (2.13), which is lower than the given f_{pr} . On the other hand, the PRF also must offer acceptable unambiguous range, that is $f_{pr} < \frac{c}{2r_{sw}}$, where r_{sw} is the maximum range swath and c is the light speed. In this case, even the range swath is 15000m, the upper limit of f_{pr} is 10kHz, which leaves enough room for airborne SAR application of WiMAX SAR. Thus, the frame structure of WiMAX base stations could provides appropriate PRF for WiMAX SAR.

2.5 Chapter Summary

In this chapter, the features of SAR and WiMAX were described to show their similarities. Moreover, four common SAR modes and the wavenumber domain algorithm for SAR imaging were depicted for the remaining part of this thesis. Further, a number of symbols, concepts, principles, equations and figures in this chapter will also be utilized in following chapters.

Chapter 3

Problems of Utilizing WiMAX for SAR

3.1 Chapter Introduction

The previous chapter demonstrates the feasibility of utilizing WiMAX base stations for SAR imaging. By contrast, some problems for the application are analyzed in this chapter. To be specific, Section 3.2 takes care of some challenges, such as large minimum range, receiver disparity, resulting from the transmitted signal pattern and receiver structure defined in WiMAX OFDM PHY. Due to the regulated EIRP limit in unlicensed band, the achievable maximum range is elaborately investigated in the Section 3.3, in which the DSP loss for imaging is also taken into consideration.

3.2 WiMAX Transceiver Mechanism

3.2.1 Transmitter signal form

1. Leakage of transmitted power

As mentioned before, WiMAX base station transceivers transmit and receive signals in the unit of frame, whose default value is 5ms. For TDD mode, a frame is divided into DL subframe and UL subframe. WiMAX base stations transmit OFDM symbols to subscribers in DL subframe while receive symbols from them in UL subframe. To maximize the throughput, the symbols in DL subframe is continuous for WiMAX base stations. Re-

member the link sample in Chapter 2, the maximum transmitted power of WiMAX base station can be 63.5dBm, while the receiver sensitivity P_r is only -94dBm, the power of transmitter signal can be over 150dB higher than that of received echo, which will not be detected due to the power leakage of the transmitter. There is no feedthrough circuit in WiMAX receiver for isolating itself from the transmitter. If a WiMAX base station is used as a radar transceiver, the signal and the echo with the same frequency cannot coexist around the antenna at the same time to avoid the interference from transmitter to the receiver. As shown in Section 3.3.1, the constrained working range of several kilometers requires the pulse's length to be much shorter than a millisecond corresponding to the range of 150km. Thus, idle time periods, used for receiving echoes, have to be inserted among OFDM symbols to transform continuous waveform into pulses.

2. Minimum range

The minimum data unit in current WiMAX system is a slot, which consists of at least two OFDM symbols. Assuming that the rectangular slot is composed of two symbols and 256 subcarriers, the minimum range is too big due to the slot length as well as transmitting-to-receiving interval for the TDD WiMAX base stations.

For the unlicensed band physical layer (WirelessHUMAN) [33], the symbol durations for license-exempt bands are shown in Table 3.1. It is obvious that the symbol duration of OFDM PHY is shorter than that defined in OFDMA PHY.

Table 3.1: Symbol time duration of WirelessHUMAN

Bandwidth (MHz)	OFDM $T_u(\mu s)$ ($\varepsilon = \frac{144}{125}$)	OFDMA $T_u(\mu s)$ ($\varepsilon = \frac{8}{7}$)
10	$22\frac{2}{9}$	$179\frac{1}{5}$
20	$11\frac{1}{9}$	$89\frac{3}{5}$

The symbol duration T_u for 20MHz OFDM PHY seems longer than the need of fast-time processing for range imaging, which is approximately from 10^{-12} to 10^{-5} s [6]. The symbol duration of T_u is $11\frac{1}{9}\mu s$, whose reciprocal is the bandwidth of a subcarrier or a subcarrier spacing. However, if during the same symbol period, there are 256 subcarriers, then the actual bandwidth of the OFDM symbol is much larger, resulting in

much narrower waveform by using pulse compression technique mentioned before. It means the equivalent simple pulse duration is only $t_{sp} = \frac{11\frac{1}{9}}{256} \times \frac{144}{125} = 0.05\mu s$ [40], which is short enough for fast-time processing.

For pulsed monostatic radar system, there is a constraint of minimum range, because the radar cannot transmit signal and receive echo at the same time. Even the CP duration is neglected, to obtain the complete echo of a pulse by WiMAX SAR, a minimum range should satisfy the inequality as, $R_{min} > \frac{T_u + T_{tr}}{2}c$, where T_u is the duration of a useful symbol and T_{tr} is the transmit-to-receive transition gap (TTG) for WiMAX SAR. The minimum TTG is approximately $50\mu s$ and a slot in a WiMAX DL subframe at least includes two OFDM symbols (i.e. $T_u = \frac{200}{9}\mu s$) [33], which yields, $R_{min} > \frac{T_u + T_{tr}}{2}c = \frac{650}{18} \cdot 300m/\mu s \approx 10833m$. Section 2.4 mentioned the R_{RAR} , representing the operation range for an RAR by using a WiMAX base station, is generally lower than the minimum range (10833m). Thus, the monostatic WiMAX SAR cannot work due to the relatively large TTG. In order to alleviate the issue of minimum range and keep similar complexity, the transitional gap has to be lower and the pulse duration should be further shortened.

Intuitively, we could use two WiMAX base stations to decrease the transitional interval. Specifically, the UL subframe of one is the DL subframe of the other. However, it is still problematic and a feasible solution will be given and detailed in Chapter 4.

3. Doppler frequency bandwidth

Equation (2.13) shows the stripmap SAR's Doppler frequency bandwidth B_D depends on the platform velocity v , antenna beamwidth θ_x as well as wavelength λ . If $\lambda = 0.0517m$, $\theta_x = \frac{\pi}{60}rad$ while the platform velocity increases to $v = 100m/s$, we can derive $B_D > 200Hz$. The default frame duration is the reciprocal of PRF, resulting in the maximum acquired PRF is 200Hz. Therefore, the frame duration of WirelessHUMAN could not meet the Doppler bandwidth requirement of SAR if the platform velocity or antenna beamwidth becomes larger.

4. Signal bandwidth

The different symbol types within a WiMAX subframe, shown in Figure 2.14, results in

a problem of bandwidth inconsistency. Some symbols, such as preambles, only exploits half number of subcarriers, causing its operating bandwidth to be half of data symbols' bandwidth. Since the range resolution is dictated by bandwidth, WiMAX SAR would further worsen its relatively low range resolution by employing such symbols.

3.2.2 Receiver structure

As shown in Figure 2.13 in Chapter 2, the OFDM receiver aims at extracting the transmitted information by a series of steps such as demapping and decoder. On the other hand, Figure 2.11 shows that the received echo data requires to be compressed for two dimensions at first. This receiver seems quite different from the OFDM-based receiver described in Figure 2.13. Thus, how to deploying OFDM receiver for SAR imaging is a problem, which will be discussed and addressed in Chapter 4.

3.3 Power Restrictions

3.3.1 Transmitted power restriction from industrial regulations

IEEE 802.16 does not give the exact power limit for devices of WirelessHUMAN. However, the power in license-exempt frequency band is restricted by industrial or local regulations.

The license-exempt frequency band from 5.725GHz to 5.825GHz pertains to an ISM band available over the world, in which besides some WiMAX users, there are many others, such as WiFi users. Also, a power restriction imposed on these WLAN users working in this band. Although FCC is planning to increase its output power to some 25 Watt [41], so far the maximum EIRP for all unlicensed WLAN systems within North America is only 4 Watt (36dBm) according to the report [42]. If the receiver antenna power gain is still 18dBi, then it yields:

$$MAPL = EIRP - IRL = 36 - (-112) = 148\text{dB}, R_{RAR} \approx 1707m.$$

Therefore, to make WiMAX SAR working in further range, e.g. 3000m, the MAPL should become: $MAPL = 10\log_{10} \frac{P_t G_m G_{RXA}}{P_r} = 10\log_{10} \frac{64\pi^3 r^4}{\sigma \cdot \lambda^2} = 10\log_{10} \frac{64\pi^3 3000^4}{10000 \cdot 0.0517^2} \approx 158\text{dB}$.

The range can be increased by improving the antenna power gain or lowering the required receiver input SNR (SNR_{in}). For instance, when the antenna power gain (G_{ta} or G_{ra}) is 28dBi

rather than 18dBi or the required SNR_{in} for post baseband DSP is -8dB instead of 2dB, the R_{RAR} can be as high as 3000m. However, the first method cannot satisfy the power restriction, since EIRP, equaling to $P_t G_{ta}$, is 10 dB more than required maximum value of 36dBm. Further, the real EIRP restriction could be more serious than 4W due to the high PAPR of OFDM symbols. In order to avoid interference with other users in same band, the required SNR_{in} has to be lowered, which can be achieved by increasing the gain of post DSP. Despite of this method, WiMAX SAR still works in relatively small range, which results to smaller minimum range, thereby demanding short pulse duration as well as transmitter-to-receiver transition time.

3.3.2 Practical consideration for the processing gain of SAR

For a single pulse of an RAR, the signal processing gain comes from the matched filtering operation to form a narrow impulse. The gain depends on the compression factor C_f and matched filtering processor. For an OFDM symbol, C_f is the number of non-zero subcarriers.

Thanks to the orthogonality of OFDM subcarriers, the author [2] stated by using the OFDM symbol as the transmitted pulse, range compression also produces high gain, which is equivalent to the simple sum of the gains contributed by matched filtering the pulses with different single subcarrier. Therefore, if the subcarrier spacing is a constant, the more subcarriers the OFDM symbol has, the higher signal processing gain the RAR would have.

We first focus our attention on the range detection probability P_{rD} and range false alarm probability P_{rFA} . The cross-range detection can be checked in similar way. The following simulation for range imaging performance, such as P_{rD} or P_{rFA} , are simulated under different thresholds and SNR_{in} .

When there is no other artificial interference source, range detection capability is subject to the level of receiver noise and natural interference to the receiver. For simplicity, we equalize the effect of some interference like Rayleigh distributed clutter to be effect of thermal noise. And many kinds of noises, either being within a radar receiver or from outside environment, are summed to be an equivalent additive white Gaussian noise (AWGN), followed by a noise-free digital signal processor for SAR imaging. Thus, the only influence factor for range detection here is AWGN, which is always in the form of the receiver input SNR (SNR_{in}) for practical

application, which is the ratio of input signal power S and an average input noise power $P_N = \frac{N_0}{2}B = kTB$. If the transmitted pulse is a useful OFDM symbol with duration of T_u and the bandwidth is B , the maximum output SNR (SNR_{mf}) is achieved by matched filtering and the ratio is

$$SNR_{mf} = \frac{2P_t G_{ta} G_{ra} \lambda^2 \sigma C_f}{(4\pi)^3 R^4 kTB} = \frac{2P_t G_{ta} G_{ra} \lambda^2 \sigma N_{sc}/B}{(4\pi)^3 R^4 kT} = \frac{2P_t G_{ta} G_{ra} \lambda^2 \sigma T_u}{(4\pi)^3 R^4 kT} = \frac{2ST_u}{N_0} \sigma = \frac{2E_1}{N_0} \sigma,$$

where the P_t is transmitting power of a single-frequency signal, and $E_1 = ST_u$ is the energy of one OFDM symbol.

In simulation, we normalize the energy of a subcarrier in single OFDM symbol to be 1, and the noise PSD $\frac{N_0}{2}$ is decided by self-defined SNR. The given SNR is also named as detectability factor [7], which represents the required SNR_{in} before matched filtering to achieve certain P_{rD} with respect to preset P_{rFA} .

The author [7] used an approximated formula for calculating detectability P_{rD} when received random signal conforms to Rician distribution with normalized DC value as unit 1. The formula was derived by North, D.O [43] as, $P_{rD} = Q(\frac{E_{t1}}{\sqrt{P_N}} - \sqrt{\frac{2S}{P_N}} + 1)$, where P_N is mean noise power and E_{t1} is the threshold decided by given false alarm rate P_{rFA} . In fact, the detectable probability, obtained from the approximated formula, is slightly overestimated compared with actual results of Rician distribution calculated by numerical method. However, the Figure 2.5 in Barton's book can be a reference for the following simulations, [7] since it demonstrates for a sinusoidal wave, to obtain the detectability of over 0.999 for a steady target, SNR_{in} of 15dB is enough when the P_{rFA} is bigger than 10^{-5} .

There is an interesting properties for matched filter: no matter how long or what types of the input waveform is, the peak of SNR_{mf} is equal to the ratio received signal energy E_1 and the noise PSD $\frac{1}{2}N_0$ if the target RCS $\sigma = 1$. If the energy of a subcarrier with an OFDM symbol length is normalized, the energy of an OFDM pulse depends on how many subcarriers it has. Since $N_{sc} = 256$, the gain by matched filtering the OFDM symbol is 24dB. Thus, $SNR_{mf} = SNR_{in} + 24\text{dB}$ by using matched filter. In other words, if $SNR_{mf} = 15\text{dB}$, the required SNR_{in} is only -9dB. The detected noise envelope conforms to Rayleigh distribution. If a threshold η is set to offer the required low probability P_{rFA} of a false alarm caused by AWGN, then the P_{rFA} can be calculated by:

$$P_{rFA} = \int_{\eta}^{\infty} \frac{x}{P_N} \exp(-\frac{x^2}{2P_N}) dx = \exp(-\frac{\eta^2}{2P_N}).$$

Thus, if we set the P_{rFA} and know the mean noise power P_N (equals to variance of AWGN), then the threshold can be derived as $\eta = \sqrt{2P_N \ln(1/P_{rFA})}$. In simulation, to find the mean noise power, we only need to know SNR_{in} because we already set the input pulse power as one.

As a priori probability is unknown in radar detection, we use the Neyman-Pearson (NP) criterion as the best criterion to determine the threshold η . Given that the power level of real-time AWGN P_N can be precisely estimated, NP norm supposes a constant false-alarm rate (CFAR) to acquire adaptive threshold [44]. Figure 3.1 briefs the detection part of a radar receiver, in which the target echo is detected by its envelope, which is a common way to detect radar echo. Given a P_N , we can derive a threshold voltage, which is used to yield P_{rD} while satisfy the requirement of a preset constant P_{rFA} . As mentioned, the input signal power at the

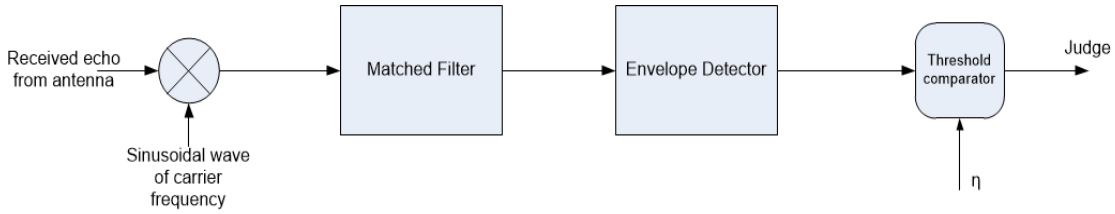


Figure 3.1: Envelope detection and threshold judge of a radar receiver for the single-carrier sinusoidal waveform.

receiver end is normalized to be 1, P_N therefore has inverse relation with the SNR_{in} . Because the farther the target range is, the weaker the echo signal power at the receiver is, SNR_{in} depends on the range of target. Thus, the detectability factor (different SNR_{in}) is used to set different P_N in simulation.

Table 3.2 shows the detection probability of different SNR_{in} from -9dB to -14dB to satisfy different P_{rFA} by simulation. According to this table, we can see even SNR_{in} is as low as -12dB, the range detection probability can be over 0.95 with the range resolution of 7.5m (20MHz). In fact, if the bandwidth is decreased, the noise power level will be reduced, thereby increasing the detection range. Thus, it is a tradeoff between range and resolution. Remember in Subsection 3.3.1, we show that to obtain the range of 3000m, the SNR_{in} is required to be -8dB instead of 2dB. However, in that case the EIRP is set as 36dBm ignoring the influence of high PAPR of OFDM symbol while the target RCS is as high as $10000m^2$.

Since signal propagates along LOS, the theoretical results are the detectable probability of a random signal of Rician distribution with a constant DC component of A, when

Table 3.2: Detection probability of single OFDM symbol with respect to SNR_{in}

SNR_{in}	-9dB	-10dB	-11dB	-12dB	-13dB	-14dB
$P_{rD}(P_{rFA} = 0.1)$	0.999	0.996	0.988	0.983	0.936	0.846
$P_{rD}(P_{rFA} = 0.01)$	0.999	0.997	0.990	0.971	0.926	0.836
$P_{rD}(P_{rFA} = 0.001)$	0.999	0.997	0.987	0.956	0.871	0.747

the threshold is set to be η . The theoretical P_{rD} can be calculated by this equation [45], $P_{rD} = \int_{\eta}^{\infty} \frac{x}{P_N} \exp(-\frac{x^2 + A^2}{2P_N}) I_0(\frac{xA}{P_N}) dx$, where I_0 represents the first kind modified Bessel function of order zero, η and P_N are same as those calculated before, while the DC content A is set to be its minimum variance unbiased (MVU) estimation, which is equal to the average peak magnitude in simulation [44].

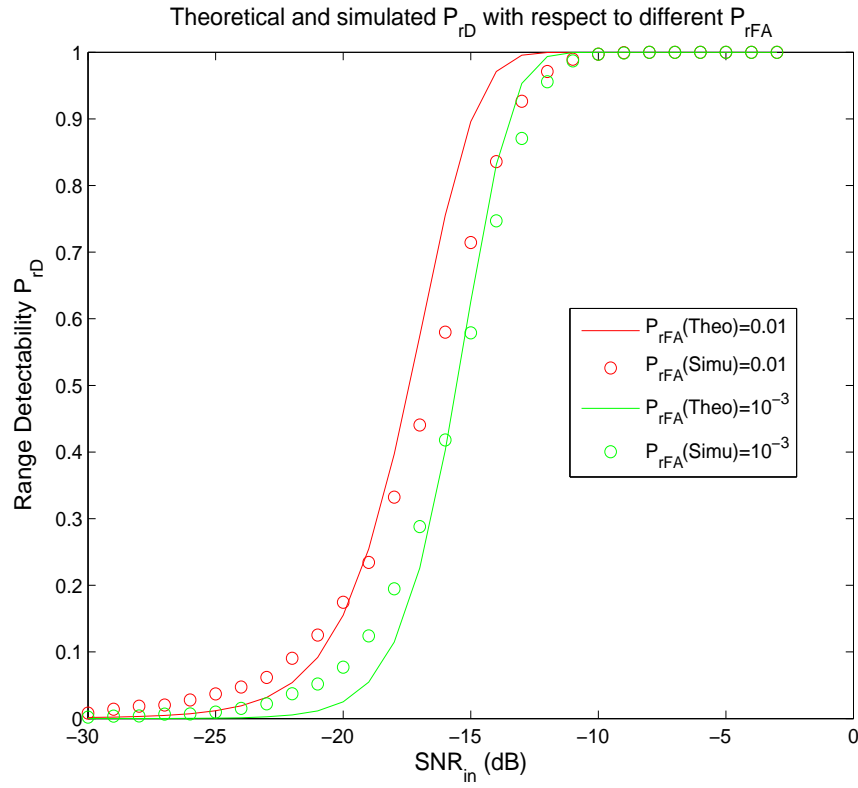


Figure 3.2: Comparison between simulation results and theoretical equation for obtaining the detectable probability of an OFDM symbol by envelope detection.

Figure 3.2 shows the similar trends of the detectable probability by the simulation results of Table 3.2 and the P_{rD} calculated by the above equation, when $P_{rFA} = 0.01$ and 0.001 ,

respectively. We can see the numerically integral result of detectable probability is close to theoretical value. Thus, OFDM symbol has similar detectability as sinusoid wave. However, compared with a sinusoidal waveform with bandwidth of a subcarrier spacing, in order to obtain same range resolution ΔR , one OFDM symbol can obtain SNR improvement as high as N_{sc} times by matched filtering.

For an OFDM symbol in WiMAX OFDM PHY, N_{sc} is 256 (24dB) if there are no guard subcarriers. However, since the imperfect digitally matched filtering, Figure 3.2 shows the required SNR_{in} of simulation results is 1 or 2 dB more than the theoretical value to obtain same detectable probability (> 0.5) for a steady target. This is a loss caused by range compression. Thus, the imperfect matched filtering processor affects the detectability for targets, and the DSP loss for range compression can be between 1 and 2 dB. Moreover, there are 56 zero subcarriers in OFDM PHY for practical WiMAX systems, resulting in the real N_{sc} of 200 (23dB), causing coarser ΔR of 9.6m. We just show the matched filtering processing in range direction can increase signal peak value by N_{sc} times at most. It works for both RAR and SAR. However, SAR has another compression gain by azimuth matched filtering. Each echo backscattered by a target is processed in a coherent manner as long as the echo is not distorted. Thus, the gain of azimuth SAR processing depends on how many pulses are transmitted within an effective aperture size L_a . Obviously, the number of pulses depends on the PRF and flight time of SAR sensor within the L_a [46]. Similarly, the DSP loss for cross-range compression can be from 1 to 2 dB, too.

An example is given to show how the processing gains in both range and azimuth direction improve the final image SNR SNR_{im} , which further lower the required SNR_{in} of RAR while keeping the detectable probability. Table 3.3 gives the parameters for this example. As

Table 3.3: Parameters of WiMAX SAR for imaging one point target

Parameter	Value
Theoretical Range resolution ΔR	9.6m
Theoretical Cross-range resolution ΔCR	0.5m
Range swath r_{sw}	400m
Azimuth unit width a_w	200m
Number of pulses N_p	2000

mentioned before, the range signal processing gain G_{rsp} is set as 23dB. The azimuth signal processing gain G_{asp} , equaling to N_p , is 2000, i.e. 33dB. Thus, the total gain is 56dB.

Image of 1 point ($SNR_{in} = -40dB$)

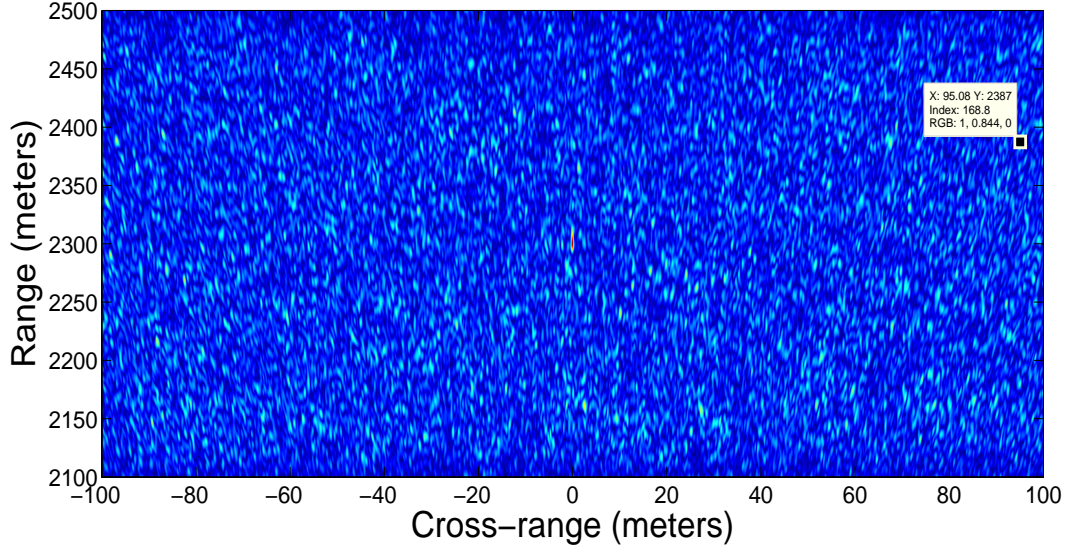


Figure 3.3: Reconstructed SAR image by ΩKA algorithm

Image of 1 point ($SNR_{in} = -40dB$ Threshold=167.6)

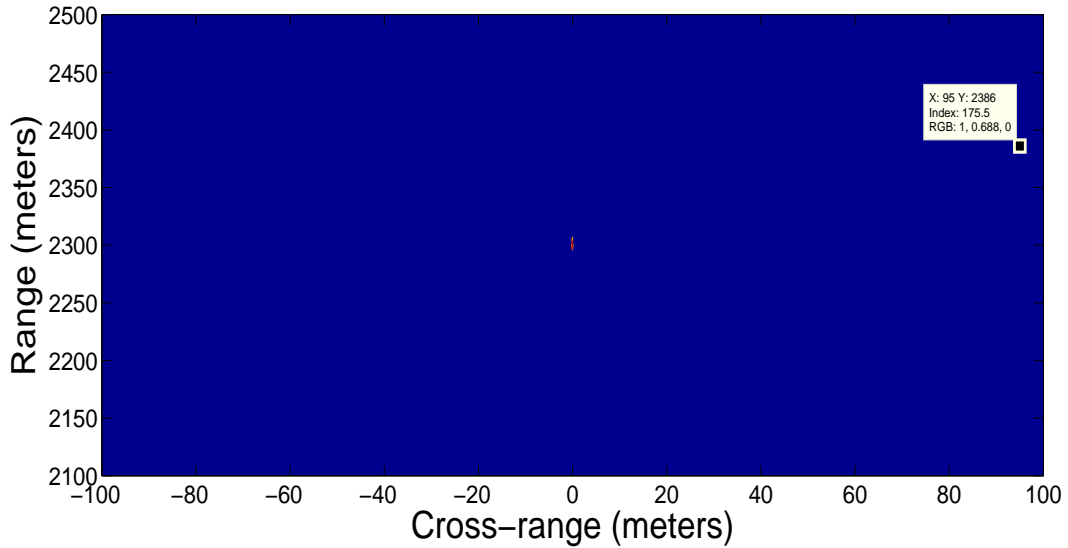


Figure 3.4: Envelope detection judged by a threshold of 167.6

Figure 3.3 and 3.4 shows SAR imaging for one target when the SNR_{in} is only -40dB. The peak value among pixels in this image is 255. Since the pixel number is $\frac{r_{sw}r_{aw}}{\Delta R \Delta CR} = 16667$. Since

the real resolutions are bigger than theoretical ones due to DSP (see Chapter 4), it is enough to set $P_{rFA} = 10^{-5}$. The value requires the SNR_{im} to be 15dB (see Figure 2.5 in Barton's book [7]). However, even if SNR_{im} is 56-40=16dB, a false alarm still appears in these two figures. It is due to the processing loss by imperfect matched filtering for both directions. The image quality is a vital parameter of SAR performance requirement [26], WiMAX SAR should therefore improve the imaging quality as far as possible, while satisfying P_{rD} and P_{rFA} is only a basic requirement.

Thus, the limited EIRP is an issue for WiMAX SAR to obtain high-quality image of low-RCS targets at a great distance. As will be shown in the simulations of Chapter 5, the SNR_{im} requires to be at least 20dB.

3.4 Chapter Summary

The chapter explained some difficulties for deploying WiMAX transceivers to the application of airborne monostatic SAR. They result from the difference of transceiver mechanisms and EIRP restriction for unlicensed WiMAX devices. The two major reasons guide the way for overcoming these challenges. Thus, this chapter works as a bridge to connect previous chapters with subsequent ones.

Chapter 4

Airborne Stripmap SAR Using License Exempt WiMAX Transceivers

4.1 Chapter Introduction

This chapter explores an idea of utilizing COTS WiMAX base station transceivers in unlicensed band for monostatic airborne SAR application. The OFDM PHY of the WiMAX transceiver has been redesigned to satisfy the requirements of airborne stripmap SAR applications. In order to accomplish stripmap WiMAX SAR, a fast microwave double-pole, double-throw (DPDT) switch with two absorbing loads have been added to the RF front of two WiMAX base stations, converting continuous OFDM waveform to pulses for transmission. For the receiver, CP is used for offering the circular convolution between transmitted pulses and channel information. This information consists of the positions of targets within an imaging area. By FFT, the convolved data in time domain is transformed to frequency-domain data, which is compressed in range by a proposed matched filter for subsequent ΩKA imaging processing. Moreover, the PRF of WiMAX SAR can be increased by this design. Simulation results manifest its feature and performance. For instance, when PRF is 1000Hz, WiMAX SAR can effectively reconstruct the image even if the input SNR at receiver end is as low as -30dB. WiMAX SAR can be used for imaging the target with relatively large RCS and size, such as a jet airliner or a truck [6], due to its limited transmission power and range resolution.

4.2 System Model of WiMAX SAR

An analytic model of WiMAX SAR is illustrated in this section. Figure 4.1 shows the block diagram of a WiMAX SAR system using commercial WiMAX transmitter and receiver. The steps of reception after the P/S are associated with software design. For SAR application, we replace these software-related blocks by imaging algorithm implementation. Specifically, a memory device follows the P/S to store 2-D raw data of targets' echoes. Afterwards, a signal processing way is proposed to perform range matched filtering, followed by executing the ΩKA algorithm, which is more robust with the change of synthetic aperture size [8].

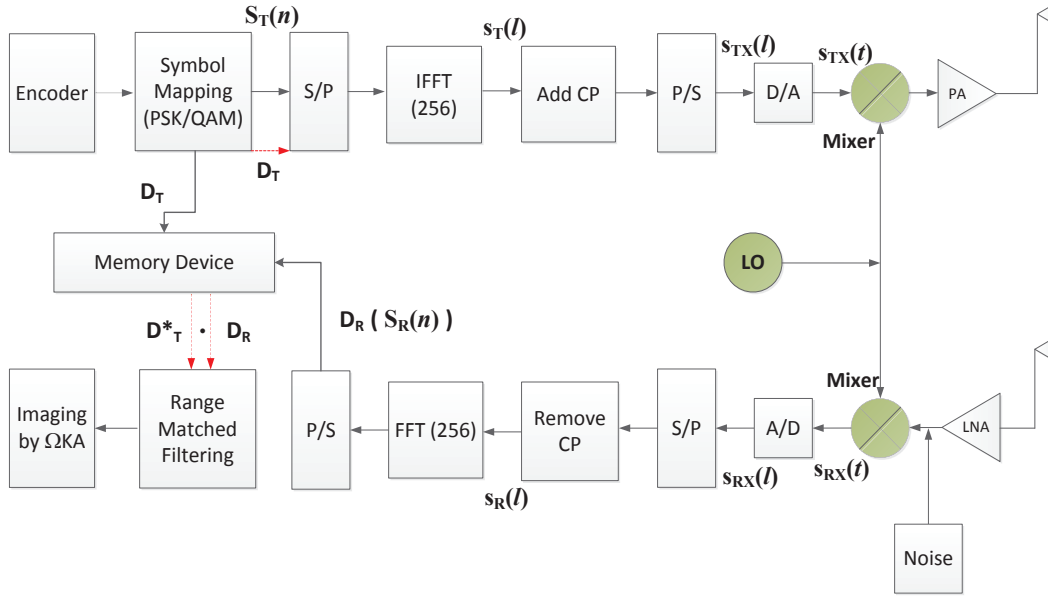


Figure 4.1: Block diagram of WiMAX SAR system. The memory device is needed to collect the frequency-domain echo data for the following software-based 2-D imaging.

As mentioned before, although WiMAX system transmits data in the unit of a frame, the signal processing of OFDM system is symbol-based. By an RF modification shown in Section 4.4, we can assume that pulse duration of WiMAX SAR is the length of an OFDM symbol. Therefore, the time-domain baseband transmitted signal, $s_{TX}(t)$, can be formulated as:

$$s_{TX}(t) = IFFT\{D_T\} \text{rect}\left(\frac{t}{T_s}\right) = \frac{1}{N_{sc}} \sum_{n=0}^{N_{sc}-1} D_t(n) \exp(j2\pi f_n t) \text{rect}\left(\frac{t}{T_s}\right), \quad (4.1)$$

where $D_T = [D_t(0), D_t(1), \dots, D_t(N_{sc} - 1)]$ is a complex vector of transmitted data digitally

modulated by QAM or PSK in frequency domain, N_{sc} is the number of subcarriers, f_n is the individual subcarrier frequency, and rect represents the rectangular shape of an OFDM pulse. Moreover, $T_s = T_u + T_g$, where T_s is the total length of an OFDM symbol, T_u is duration of useful OFDM symbol while T_g represents the duration of guard interval, which usually stands for length of CP.

The transmitted baseband signal is $s_{TX}(t)$ while the received baseband backscattered echo is defined as $s_{RX}(t)$. The moving SAR platform, compared with stationary targets, can produce Doppler shift for $s_{RX}(t)$. However, the processing for variation of Doppler shift depends on adopted SAR imaging algorithms. This chapter only focuses on the data acquisition of target in range direction by WiMAX systems. The received baseband signal, $s_{RX}(t)$, is expressed as

$$s_{RX}(t) = \frac{1}{N_{sc}} \sum_{n=0}^{N_{sc}-1} A(n) D_t(n) \exp\left(j2\pi f_n \left(t - \frac{2R}{c}\right)\right) \text{rect}\left(\frac{t - \frac{2R}{c}}{T_s}\right), \quad (4.2)$$

where $A(n)$ is a vector indicating the amplitude attenuation and phase distortion of n subcarriers over propagation channel and transceivers, and $\frac{2R}{c}$ is the delay caused by a target of range R while c is speed of light.

4.3 Range Matched Filtering by WiMAX Receiver

This section depicts a signal processing approach to use WiMAX receiver for data acquisition and range matched filtering.

From the diagram of Figure 4.1, we can notice a unique feature of the OFDM system is the operations on CP. Figure 4.2 shows how a whole OFDM symbol pass through a communication channel with length of $(G + 1)\Delta t$, where Δt is the sampling time spacing, which is equal to the reciprocal of sampling frequency, i.e. $\Delta t = \frac{1}{f_s}$. As we learn in the course related to *signal and system*, the simple multiplication of two continuous-time functions in frequency domain corresponds to the linear convolution of IFT in time domain. Similarly, the dual of dot multiplication of two discrete sequences in frequency domain is the circular convolution for these two signals modified by inverse discrete Fourier transform (IDFT) in time domain [41]. Provided that the two signals are s_1 and s_2 in time domain, these relations are shown in

equation (4.3).

$$\begin{cases} S_1(f) \bullet S_2(f) \longleftrightarrow \mathbf{FT}\{s_1(t) * s_2(t)\}, \\ S_1[n] \bullet S_2[n] \longleftrightarrow \mathbf{DFT}\{s_1[l] \otimes s_2[l]\}, \end{cases} \quad (4.3)$$

where \bullet represents the simple multiplication for continuous-time signals and dot multiplication for discrete sequences, while $*$ and \otimes stand for linear and circular convolution, respectively.

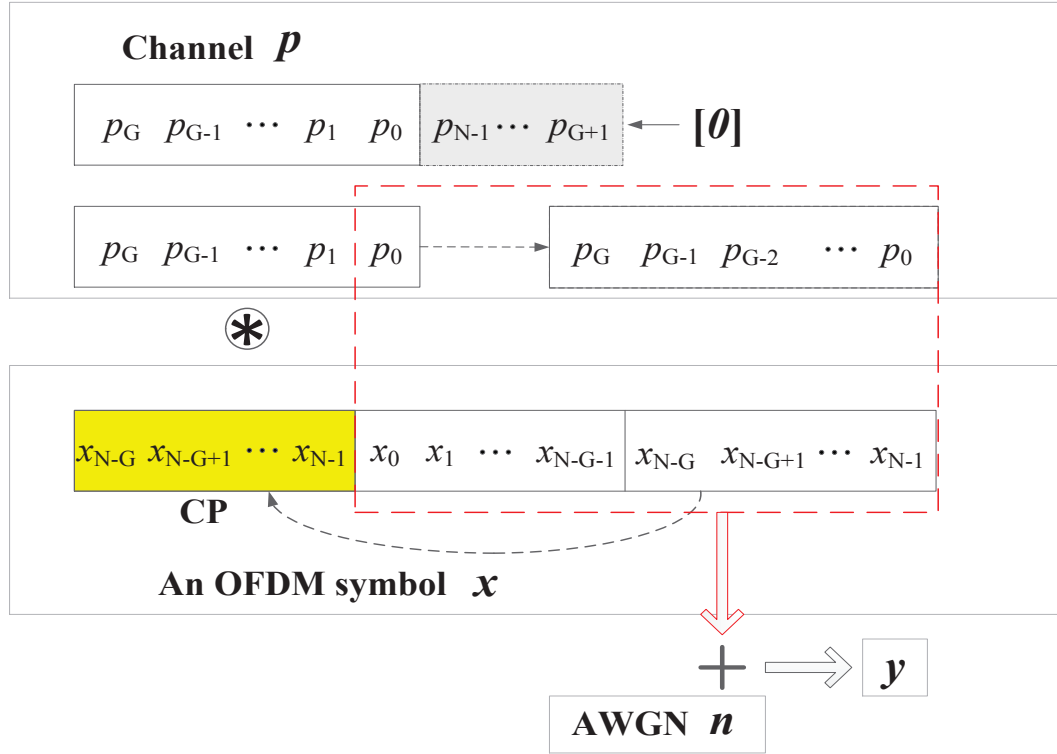


Figure 4.2: The operation of circular convolution between an OFDM symbol and channel, which is established through the inserted cyclic prefix (CP).

In general, it is a process of linear convolution when a signal, in the form of either continuous or discrete, passes through a channel. To maximize the throughput, the signal of OFDM system is continuous. Considering the effect of latency, the data processing unit cannot be too long and it is always a symbol in the microsecond scale. Like the transmitter, the OFDM-based receiver also processes the symbols one after the other. Thus, in order to contain channel information within a symbol length, the linear convolution operation is replaced with the circular convolution for the symbol-wise processing. Due to the delay by multi-path environment, a time interval should be inserted between two adjacent symbols. For accomplishing the circular convolution, we can place a cyclic prefix (CP) containing the last G time samples in each sym-

bol in this interval due to the channel length of $(G + 1)\Delta t$, shown as the yellow part in Figure 4.2. Together with the data part, the total length of an OFDM symbol \mathbf{x} is $N_T = N + G$. The figure also depicts the channel as a vector with length of $G+1$. Since the size of useful symbol is N , we can assume the length of channel vector \mathbf{p} is also N , i.e. $\mathbf{p} = [p_0, p_1, \dots, p_{N-1}]$, while leaving $N-G-1$ samples to be zeros (gray part). When p_0 shifts from the left edge to the right edge of the red dashed rectangle, the dot multiplications between channel vector \mathbf{p} and input vector $\mathbf{x} = [x_0, x_1, \dots, x_{N-1}]$ produces output vector $\mathbf{y} = [y_0, y_1, \dots, y_{N-1}]$ by the circular convolution in the equation (4.4).

$$\begin{cases} y_0 &= p_0 x_0 + p_1 x_{N-1} + \dots + p_G x_{N-G} + p_{G+1} x_{N-G-1} + \dots + p_{N-1} x_1. \\ y_1 &= p_0 x_1 + p_1 x_0 + \dots + p_{G+1} x_{N-G} + p_{G+2} x_{N-G-1} + \dots + p_{N-1} x_2. \\ \vdots &= \vdots \\ y_{N-1} &= p_0 x_{N-1} + p_1 x_{N-2} + \dots + p_{G-1} x_{N-G} + p_G x_{N-G-1} + \dots + p_{N-1} x_0. \end{cases} \quad (4.4)$$

As shown in Figure 4.2, the circular convolution \otimes is composed of two operations: a linear convolution between \mathbf{p} and \mathbf{x} , and the removal of the CP via selecting the area in the red dashed rectangle. The circular convolution produces a circulant matrix \mathbf{P} , and the received signal in time domain can be represented as,

$$\mathbf{y} = \mathbf{P}\mathbf{x} + \mathbf{n}, \quad (4.5)$$

where \mathbf{n} is the AWGN noise vector, and according to the equation (4.4), the channel matrix \mathbf{P} can be written as,

$$\mathbf{P} = \begin{bmatrix} p_0 & p_{N-1} & \dots & p_1 \\ p_1 & p_0 & \dots & p_2 \\ \vdots & \vdots & \ddots & \vdots \\ p_{N-1} & p_{N-2} & \dots & p_0 \end{bmatrix}, \quad (4.6)$$

where p_i denote the channel impulse responses (CIR) and $p_i = 0$ for $G < i \leq (N - 1)$.

Given an N -point FFT, a data vector in frequency domain is $\mathbf{X} = [X_0 \ X_1 \ \dots \ X_{N-1}]$. The data vector \mathbf{x} in time domain is generated by an IFFT operation on \mathbf{X} . The FFT, as a fast form

of the discrete Fourier transform (DFT), can be denoted in the way of a matrix:

$$[\mathbf{F}]_{l,n} = N^{-\frac{1}{2}} e^{-j2\pi \frac{ln}{N}}, \quad l, n = 0, 1, \dots, N-1. \quad (4.7)$$

where $N^{-\frac{1}{2}}$ is a factor to keep bit energy constant and $(l-1, n-1)$ represents the $(l, n)^{th}$ entry of the square matrix \mathbf{F} . It is easy to see the inverse discrete Fourier transform (IDFT) is the Hermitian matrix of \mathbf{F} , i.e.

$$N^{-\frac{1}{2}} e^{j2\pi \frac{nl}{N}} = \mathbf{F}^H, \quad n, l = 0, 1, \dots, N-1 \quad (4.8)$$

Therefore, the transmitted data vector in time domain is $\mathbf{x} = \mathbf{F}^H \mathbf{X}$. Since channel length is $G+1$, the OFDM symbol requires a CP with length of $N_{CP} \geq G$. As mentioned before, here we have $N_{CP} = G$.

Gray demonstrated that the DFT of the first column of a circulant matrix are the eigenvalues of this matrix, which also represents the frequency response of channel in a discrete manner. The eigenvectors of a square circulant matrix of a given size are the columns of the DFT matrix \mathbf{F} with the same size [47]. Since the DFT matrix \mathbf{F} is nonsingular and is a unitary matrix, the circulant matrix \mathbf{P} can be denoted as, $\mathbf{P} = \mathbf{F}^H \mathbf{P}_{EV} \mathbf{F}$, where \mathbf{P}_{EV} is a diagonal matrix using N eigenvalues as its diagonal entries. Similarly, we have

$$\mathbf{F} \mathbf{P} \mathbf{F}^H = \mathbf{P}_{EV} = \text{diag}(P_0, P_1, \dots, P_{N-1}), \quad (4.9)$$

where $P_n = \sum_{l=0}^G p_l e^{-j2\pi \frac{ln}{N}}$, $n = 0, 1, \dots, N-1$. Therefore, P_n denotes the frequency response of the n -th subcarrier.

Based on the received signal vector in time domain $\mathbf{y} = \mathbf{P} \mathbf{x} + \mathbf{n}$, and equation (4.9), the received data vector in frequency domain by the DFT can be written as,

$$\begin{aligned} \mathbf{Y} &= \mathbf{F} \mathbf{y} \\ &= \mathbf{F}(\mathbf{P} \mathbf{x} + \mathbf{n}) \\ &= \mathbf{F}(\mathbf{F}^H \mathbf{P}_{EV} \mathbf{F} \mathbf{x} + \mathbf{n}) \\ &= \mathbf{P}_{EV} \mathbf{X} + \bar{\mathbf{n}}. \end{aligned} \quad (4.10)$$

Since \mathbf{F} is a linear transform, the statistical properties of $\tilde{\mathbf{n}} = \mathbf{F}\mathbf{n}$ is same as \mathbf{n} . Therefore, the variance of AWGN noise is independent of the FFT operation and SNR at the receiver end will not be affected by the digitally frequency transform.

According to equation (4.10), we can see how a CP-created circulant matrix \mathbf{P} connects the frequency-domain output \mathbf{Y} with the frequency-domain input \mathbf{X} in a simple way. As long as the channel-caused maximum latency is smaller than the guard interval, this equation shows it is easy to extract the information of the transmitted data vector \mathbf{X} or the channel frequency response \mathbf{P}_{EV} via matched filtering if the other is already known or correctly estimated.

For SAR or RAR applications, \mathbf{P}_{EV} represents the channel information to acquire targets' positions. As shown in equation (4.6), the CP length determines the number of its non-zero elements in a column of \mathbf{P}_{EV} , which stands for the width of radar channel, i.e. r_{sw} . Thus, duration of CP should be as large as possible to obtain larger imaging range swath r_{sw} of SAR.

Figure 4.3 shows continuous OFDM symbols are truncated by the DPDT switch design shown in Section 4.4, resulting in pulsed symbols to be the WiMAX SAR signal form. We can set the start point of reception as the moment that transmitter just finishes emitting a symbol. As mentioned, if the delay caused by range swath is lower than CP's length, whole range information of all targets within this swath can be recorded in the received data symbol even if CP is discarded [48]. Figure 4.3 shows WiMAX SAR receiver only extracts a data symbol with length of T_u by removing CPs while maintaining D_T intact. Therefore, the time shift $\frac{2R}{c}$ of the rect-function in equation (4.2) can be neglected. As mentioned in [33], the f_n equals to $\frac{n}{T_u}$. If the sampling frequency of A/D is f_s , N_{sc} is the number of sampling points for the useful symbol duration and it equals to $T_u \cdot f_s$ while CP is $T_g \cdot f_s$. Thus, f_n can be denoted as $\frac{nf_s}{N_{sc}}$.

If the CP has been removed, the received sequence $s_R(l)$ in Figure 4.1 can be represented as a discrete format of received baseband signal $s_R(t)$ and l is equal to tf_s . And it can be converted back to a vector \mathbf{D}_R in frequency domain by implementing FFT. Given that the target RCS is $1m^2$, \mathbf{D}_R or $\mathbf{S}_R(\mathbf{n})$ is denoted by equation (4.11), where FFT represents FFT operator while \circ denotes Hadamard product and \otimes represents circular convolution. The phase delay is a vector

caused by a target's range, which is $PD(r)=[1, \exp(j\frac{2\pi}{N_{sc}}r), \dots, \exp(j\frac{2\pi(N_{sc}-1)}{N_{sc}}r)]$.

$$\begin{aligned} D_R = S_R(n) &= FFT\{s_R(l)\} = FFT\left\{\frac{1}{N_{sc}} \sum_{n=0}^{N_{sc}-1} A(n)D_t(n)\exp(j\frac{2\pi n}{N_{sc}}(l - \frac{2Rf_s}{c}))\text{rect}(\frac{l}{N_{sc}})\right\} \\ &= A \circ D_T \circ PD(-\frac{2Rf_s}{c}) \otimes SINC. \end{aligned} \quad (4.11)$$

The *sinc* sequence, obtained by FFT of the rectangular sequence $\text{rect}(\frac{l}{N_{sc}})$, can also be denoted as a vector, i.e. $SINC = [\text{sinc}(0), \text{sinc}(1), \dots, \text{sinc}(N_{sc} - 1)]$, if its phase information is neglected.

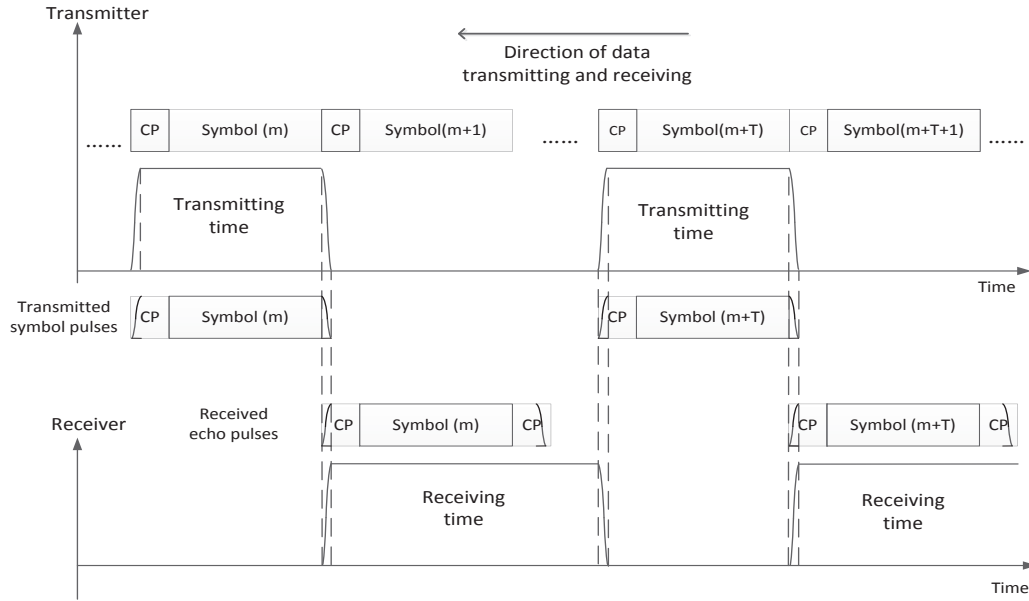


Figure 4.3: The pulse, with the length of an OFDM symbol, is transmitted and received by WiMAX SAR.

The current standard [33] shows the N_{sc} is 256 while the maximum CP is 64 for WiMAX OFDM PHY. It uses middle 200 subcarriers to transmit data while sets 55 zeros as guard time band on both sides together with a DC at the center. This means the digitally modulated data vector D_T contains zeros. Therefore, it is not appropriate to do scalar division like [48] proposed. Neglecting the shaping effect by convolving *sinc* function and multiplying D_R by

complex conjugate of the transmitted data vector D_{mTX}^* , we can obtain:

$$D_R \circ D_T^* = |D_T|_{1 \times N_{sc}}^2 \circ A \circ PD\left(-\frac{2Rf_s}{c}\right), \quad (4.12)$$

where $|D_T|^2$ is a constant vector. The target's relative range R can be obtained by executing IFFT on equation (4.12), and $\frac{2Rf_s}{c}$ is smaller than CP. The way to extract target range information is independent of encoding and digitally modulation methods of the transmitted data D_T . As transmission unit is an OFDM symbol, the minimum range of WiMAX SAR is $R_{min} = \frac{c}{2} \cdot T_s$. Figure 4.3 shows the range swath of WiMAX SAR imaging starts at R_{min} , thus the real range is $R_{real} = R_{min} + R$.

Above processing results in the range information of targets. However, most SAR imaging algorithms set the reference range as the center of range swath r_c rather than R_{min} , to execute range matched-filtering for the following 2-D image reconstruction. The reference signal can be expressed by equation (4.13), where $*$ represents the complex conjugate.

$$\begin{aligned} D_{Rc}^* &= FFT\left\{\frac{1}{N_{sc}} \sum_{n=0}^{N_{sc}-1} D_t(n) \exp\left(j \frac{2\pi n}{N_{sc}} \left(l - \frac{2R_c f_s}{c}\right)\right) \text{rect}\left(\frac{l}{N_{sc}}\right)\right\}^* \\ &= D_T^* \circ PD\left(\frac{2R_c f_s}{c}\right) \otimes SINC, \end{aligned} \quad (4.13)$$

where R_c is the relative reference range, equaling to $r_c - R_{min}$. For shifting the range variable from R to $R - R_c$, we can multiply D_R by D_{Rc}^* using Hadamard product while neglecting constant vector and the convolved *sinc* function, which yields

$$D_R \circ D_{Rc}^* = D_R \circ D_T^* \circ PD\left(\frac{2R_c f_s}{c}\right) = A \circ PD\left(-\frac{2(R - R_c)f_s}{c}\right). \quad (4.14)$$

4.4 RF Design for WiMAX SAR

This section first describes range limitation of WiMAX SAR in 5.8GHz unlicensed band. Our RF design for improving range-related parameter is given later.

4.4.1 System range level

This sub-section evaluates the achievable operating range for WiMAX SAR in the 5.8GHz unlicensed band.

Based on current IEEE 802.16-2012 standard [33], WiMAX have two types of spectra, i.e. licensed and license-exempt bands. For licensed band, the transmitted power is high enough to support over 10 km range. Nonetheless, the license is too expensive to pay. By contrast, license-exempt band is free while the transmitted power is constrained. Apart from power, another problem for WiMAX SAR working in an unlicensed band is how to share the band with others.

A license-exempt frequency band ranging from 5.725GHz to 5.825GHz is within a world-wide ISM band, in which there are not only some WiMAX users but many more other users, such as WLAN users. Thus, it is quite difficult to develop a mechanism for WiMAX SAR to coordinate with users of different standards. However, WiMAX SAR can still coexist with others. FCC [49] regulated the EIRP of wireless transmitters used for point-to-multipoint link (PtMP) is 3.2 Watt (35dBm) in this ISM band. Under this power, WiMAX SAR can mitigate its interference with others to an acceptable level. On the other hand, WiMAX SAR mounted on the aircraft operates imaging in a remote area, and concurrently antennas of WLAN base stations commonly orient towards the ground of the pathloss-concentrated metropolitan area. WiMAX SAR is not located within the beam of WLAN users and is free from their interferences. Therefore, it is feasible for WiMAX SAR to work under the power limitation of WLAN.

Figure 4.1 demonstrates the major noise is produced before echoes come into the receiver mixer. Neglecting the noise caused by A/D converter and FFT processor, we call this noise the input noise and corresponding signal-to-noise ratio (SNR) the input SNR, i.e. SNR_{in} . If SNR_{in} is lower than required input SNR SNR_{req} , the reconstructed image quality cannot be accepted. The SNR_{req} is dictated by the gains of post DSP, including range and azimuth processing.

Although the maximum EIRP is 35dBm, the PAPR for OFDM waveform is relatively big. The author [50] showed the probability of PAPR larger than 11 dB is only 0.001. Thus, the EIRP of WiMAX SAR, which is $P_t G_{ta}$ in equation (7), is reset as 24dBm. The antenna's gain

G_{ta} or G_{ra} is around 31dBi according to selected antenna aperture size, which will be shown in Section V. The noise figure of low-noise amplifier (LNA) F_n is 4 dB [38] while the loss of the transmission line L_t is 2dB.

A noticeable factor is the radar cross section (RCS) σ , which represents the target reflectivity. Assuming transmitter and receiver share same single polarization for simplicity, the maximum RCS σ_{max} of a perfectly stationary reflector, like a cylinder, is a scalar. It is dictated by reflector's size, material, shape and working frequency, while the practical RCS σ also depends on observation angle. Harre [51] shows the median RCS of a small vessel is around $30000m^2$. Thus, by rewriting the equation (2.35), an image with required input SNR SNR_{req} of 0 dB yields the maximum range at 5.8GHz as,

$$R_{max} = \left[\frac{P_t G_{ta} G_{ra} \lambda^2 \sigma}{(4\pi)^3 k T B F_n L_t S N R_{req}} \right]^{\frac{1}{4}} \approx 2521 \text{ m}, \quad (4.15)$$

where the kTB is noise power and λ is wavelength.

Based on above formula, we can increase range by raising antenna power gain G_{ra} or reducing SNR_{req} , yet the former is at the risk of violating regulations. It is worth noting the aperture size might be increased due to adopted antenna size. Therefore, the ΩKA algorithm detailed in [21] is preferable [8] to be applied in WiMAX SAR.

4.4.2 Design to increase signal processing gain

This sub-section depicts the purpose and structure of proposed RF front design. Intuitively, we can increase the pulse transmission rate to improve the gain from DSP of SAR, thereby lowering the SNR_{req} . In fact, the authors [8] illustrated for an airborne SAR, the practical PRF can be higher than that required by minimum PRF, and increasing PRF in a reasonable scope can improve receiver SNR without the need of growing peak power or pulse width. Thus, the gain from DSP of SAR can be improved by increasing PRF.

On the other hand, the maximum Doppler bandwidth has to be lower than PRF to satisfy Nyquist sampling criterion [6]. For airborne SAR, the nominal value of platform velocity is from 100 to 300m/s. The maximum Doppler frequency of airborne stripmap SAR is obtained

by equation (4.8).

$$F_{Dmax} \approx \frac{2v\phi_{az}}{\lambda} = \frac{2v}{D_a}, \quad (4.16)$$

where ϕ_{az} is the antenna beam angle. It will be shown that antenna physical size D_a is 1m. If the velocity is 200m/s, then F_{Dmax} is 400Hz. The PRF of standard WiMAX transceiver is fixed, equaling to the reciprocal of frame duration. As the default frame duration of WiMAX OFDM PHY in unlicensed band is 5 milliseconds, the default PRF is only 200Hz. Thus, in order to increase PRF of WiMAX SAR is essential. To maximally maintain the commercial WiMAX integrated systems, we propose to utilize two synchronized WiMAX base stations of same configuration and a high-speed DPDT switch with two absorbing loads, to increase PRF. A DPDT switch is composed of two synchronized single-pole, double-throw (SPDT) switches. Figure 4.4 shows the small-scale hardware alteration to achieve higher PRF, in which the OFDM generator represents the blocks from S/P to D/A, while OFDM remover denotes the

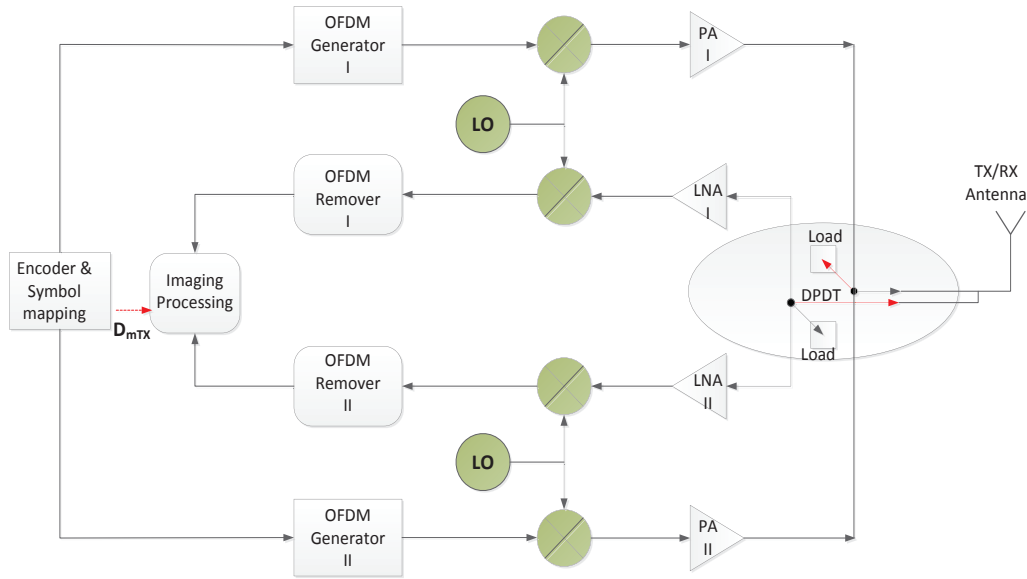


Figure 4.4: Schematic diagram of WiMAX SAR RF design. When the black switches are working, WiMAX SAR is transmitting. When a whole symbol is already transmitted, the red switches work for echo receiving as shown in Figure 4.3.

blocks from A/D to P/S in Figure 4.1. A single antenna is used for transmission and reception. And the two same WiMAX base stations, base station I and base station II, are of TDD mode. The frame of TDD-mode base station contains two subframes, i.e. downlink (DL) and uplink

(UL). For each base station, its DL and UL subframes are of same length. Using base stations to transmit signal and receive echo, we call DL subframes of base station I and base station II the TX_I and TX_II respectively. Similarly, the UL subframes are named the RX_I and RX_II. Thus, TX_I and RX_II share same time duration of one half frame while TX_II and RX_I share another half.

During the TX_I, when the switch (black pair) connects power amplifier I (PA I) with antenna for transmission, the PA II at the same time emits nothing as it is within the RX_II, resulting in no radiation ideally. Because the isolation (ISL) between the two SDPT switches cannot be infinity and return loss (RL) of absorbing load is not zero, the power leakage from PA I to low-noise amplifiers (LNA II) still happens. The cutting-edge technique can provide ISL of over 80dB from 0.5 to 10GHz [52]. Therefore, the power leakage from PA I to LNA II is $P_t - ISL = (24 - 31) - 80 = -87\text{dBm}$. Although it is big, the receiver in RX_II is not set to start processing until when the DPDT switch turns from the black pair to the red pair. Although PA I still have output signal, the amplified signal enters into a absorbing load instead of antenna from now on. If the RL of absorbing load is high enough, then the power leakage from PA I to LNA II can be as low as noise floor (-101dBm when bandwidth is 20MHz). Assuming RL is 15dB at 5.8GHz, then the leakage power coupled to LNA II can be lower than the noise floor of 20MHz bandwidth ($P_t - ISL - RL = (24 - 31) - 80 - 15 = -102\text{dBm}$). Considering the gain of RX antenna for received echo, the receiver sensitivity can be as low as -118dBm, ensuring the backscattered echo of weak power from targets can be received by WiMAX SAR. The case of WiMAX SAR within TX_II operates in a similar manner.

Figure 4.5 shows why WiMAX SAR needs two base stations. The top sub-figure shows a way to obtain default PRF (200 Hz) for SAR imaging on the condition that both TTG and receive-to-transmit transition gap (RTG) are short enough to enable minimum range to satisfy: $R_{min} > \frac{c}{2} \max[\text{TTG}, \text{RTG}]$. The middle sub-figure shows the waveform resulting from using a DPDT switch to control one WiMAX base station and using one additional receiver at the same time. This way cannot ensure fixed PRF due to the fact that base station cannot transmit pulses during UL subframe. The bottom sub-figure presents a method to increase PRF while avoid the negative effects of TTG and RTG between subframes at the same time.

The switching rate of 1000Hz is commonly used to test the switch's life performance [53].

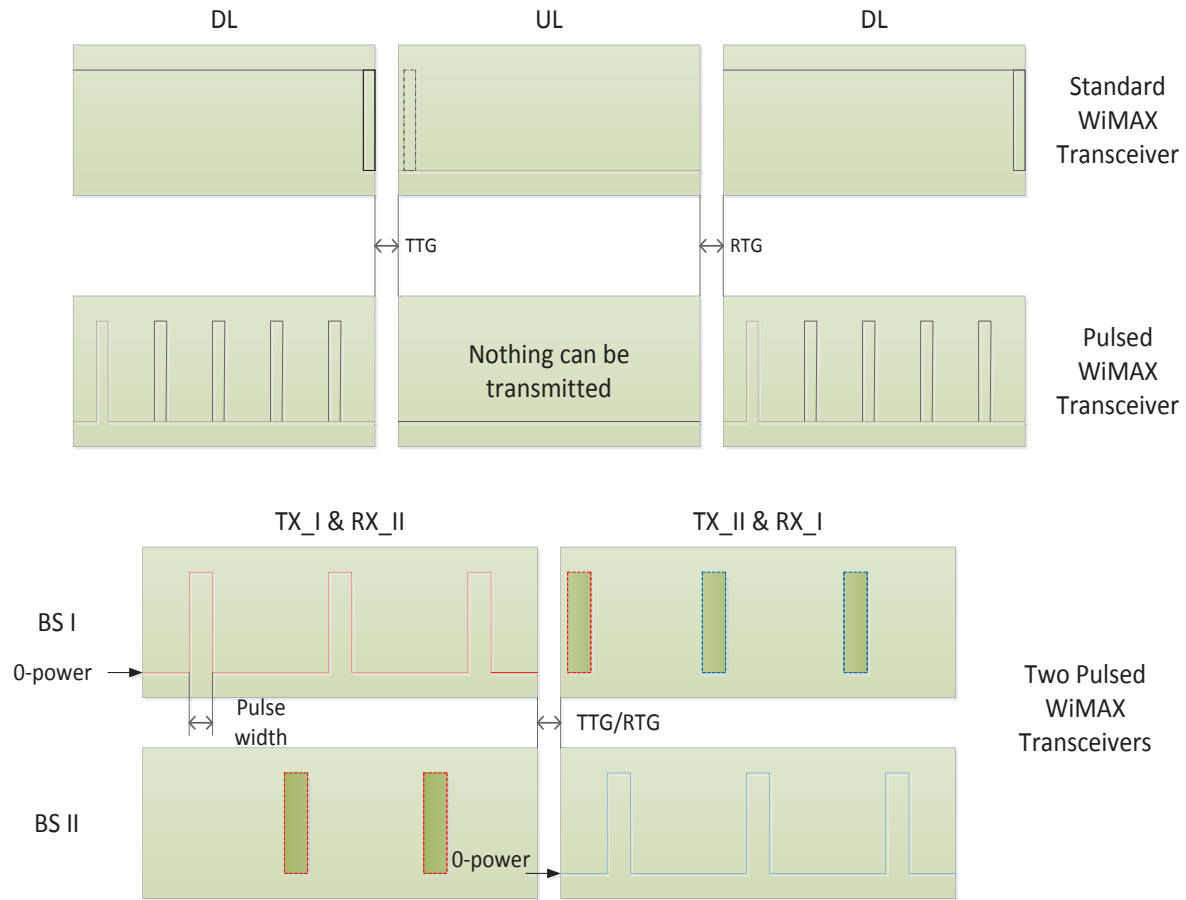


Figure 4.5: The reasons why two WiMAX base stations are required to be used include: forcing the length of pulses to be only one symbol duration; obtaining constant PRF; increasing the PRF to satisfy the requirement of Doppler bandwidth.

As the switching speed of the DPDT switch dictates the PRF of WiMAX SAR, we can set the PRF as at least 1000 Hz. Although the symbol duration is as short as the order of microsecond, the M/A-COM company [54] has designed faster GaAs switch with settling time of only 10 to 100 nanoseconds. Thus, the minimum pulse duration is almost same as an OFDM symbol length by the fast DPDT switch. This duration is much shorter than subframe duration (2.5 millisecond). As long as five symbol pulses are transmitted in a frame, the PRF becomes 1000 Hz. Moreover, the base station I and base station II exchange modes of transmission and reception at an interval of a subframe. Thus, a fixed but higher PRF can be given by using two WiMAX base stations shown in bottom sub-figure of Figure 4.4, in which the transmitted symbol pulses of base station I and base station II are colored to be red and blue respectively. And the received echoes are filled with green color.

As shown in Figure 2.14, a DL subframe contains different symbols, in which frame control head (FCH) have same operating subcarriers as data symbols while preambles are different [33]. There could be 64 or 128 subcarriers in preambles rather than 200 nonzero subcarriers in data or FCH symbols, resulting in different signal bandwidth. It is preferable to avoid using the preambles as transmitted data. The symbols of preamble are located in the first two symbols of a DL subframe. By setting an appropriate PRF, the DPDT switch enables WiMAX SAR to avoid preambles transmission. Figure 4.6 shows current microwave switches with fast settling time ($T_{set} < 100ns$) can be used to choose only data symbols as its transmission pulses if the pulse repetition interval (PRI) of WiMAX SAR is bigger than the sum of three-symbol length and duration of TTG or RTG. The "Volt" in this figure represents the percentage of detected RF voltage and the time duration of $0.1\mu s$ in which the percentage increases from 0% to 99.9% denotes the switch-on settling time T_{set} .

Thus, the slight RF front modification not only maintains the composition of commercial WiMAX base stations, but also allows the continuous OFDM waveform of standard WiMAX system to be changed as pulsed OFDM for SAR application. Further, this design frees WiMAX SAR from the constraints of fixed low PRF via adjusting the DPDT switch rate.

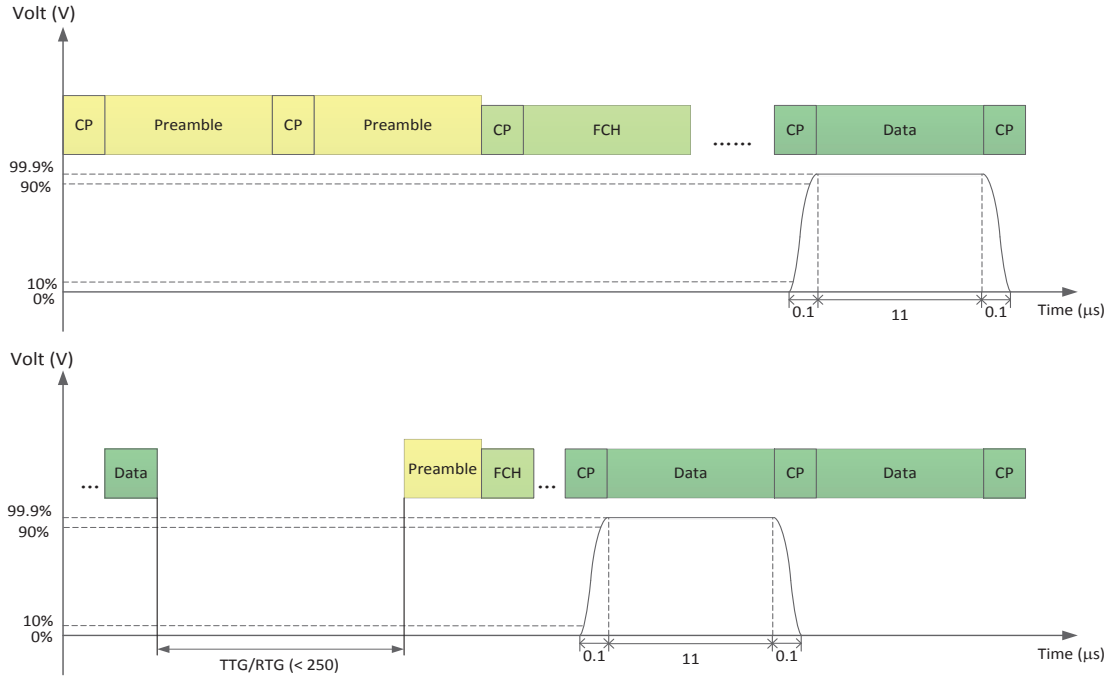


Figure 4.6: The proposed design can avoid negative effects such as large minimum range due to the length of TTG or RTG, and bandwidth loss caused by the symbols of preambles, by using a fast controlled DPDT switch for two WiMAX base station transceivers.

4.5 System Parameters and Simulation Results

This section gives the theoretical imaging resolution at the beginning, followed by the operating parameters of WiMAX SAR for simulation. Simulation results first show SNR_{req} can be lowered to expand range by increasing PRF. After that, the practical imaging resolutions ΔR and ΔCR are evaluated. The simulation of WiMAX SAR for imaging the famous Golden Gate Bridge is shown eventually.

The range resolution of WiMAX SAR is limited by WiMAX system bandwidth. The maximum bandwidth B of WiMAX systems in the unlicensed band is 20 MHz [33]. With the consideration of only 200 of 256 subcarriers which carry data, the theoretical range resolution of WiMAX SAR is

$$\Delta R = \frac{c}{2B} \times \frac{256}{200} = 9.6m, \quad (4.17)$$

where c is the speed of light. Neglecting the strength difference of pilot subcarriers [3], the code of WiMAX pulses is given in Appendix D. However, the azimuth resolution ΔCR of stripmap SAR is equal to half of D_a . This is shown in equation (2.7), which shows an antenna of

smaller size produces finer azimuth resolution. However, it causes less antenna gain and wider illuminating beam. To balance the resolution and antenna gain, the traditional antenna size D_a of SAR in C band (3.5-7.5GHz) is around 1m, resulting in the azimuth resolution of about 0.5m. This could cause that range unit is much larger than cross-range unit in the constructed SAR image. However, Moore [35] pointed out the rectangular pixels possess similar interpretability as that of square ones for various targets.

The system parameters of stripmap WiMAX SAR is set up in Table 4.1. Assuming the platform velocity v is fixed, the aperture sample spacing du represents the *PRF* level. Thus, in simulation we change *PRF* by using different du .

Table 4.1: Simulation parameters of WiMAX SAR

Parameter	Value
EIRP $P_t G_{ta}$	24dBm
Carrier frequency f_c	5.805GHz
Pulse duration $T_p (=T_s)$	$\frac{125}{9}\mu s$
Sampling frequency f_s	23.04MHz
Theoretical Range resolution ΔR	9.6m
Antenna aperture size D_a	1m
Theoretical Cross-range resolution ΔCR	0.5m
Reference range R_c	2300m
Range swath width r_{sw}	400m
Azimuth imaging unit width a_w	200m
Aircraft velocity v	200m/s
Target RCS σ	$10m^2$
PRF f_{pr}	1000Hz

4.5.1 Image quality improvement by increasing PRF

In this subsection, it is shown that the increase for PRF leads to lower SNR_{req} of WiMAX SAR. Figure 4.7 shows the original point targets and their corresponding WiMAX SAR image when SNR_{in} is 0dB and PRF is 1000Hz.

Figure 4.8 depicts the WiMAX SAR image of -30dB SNR_{in} with du of 0.5m and 0.2m, respectively. It is easy to see the image quality improves with the increase of PRF. If we set the SNR_{req} as -30dB, the operating range of SAR can be extended to over 6km for imaging the small vessel mentioned above.

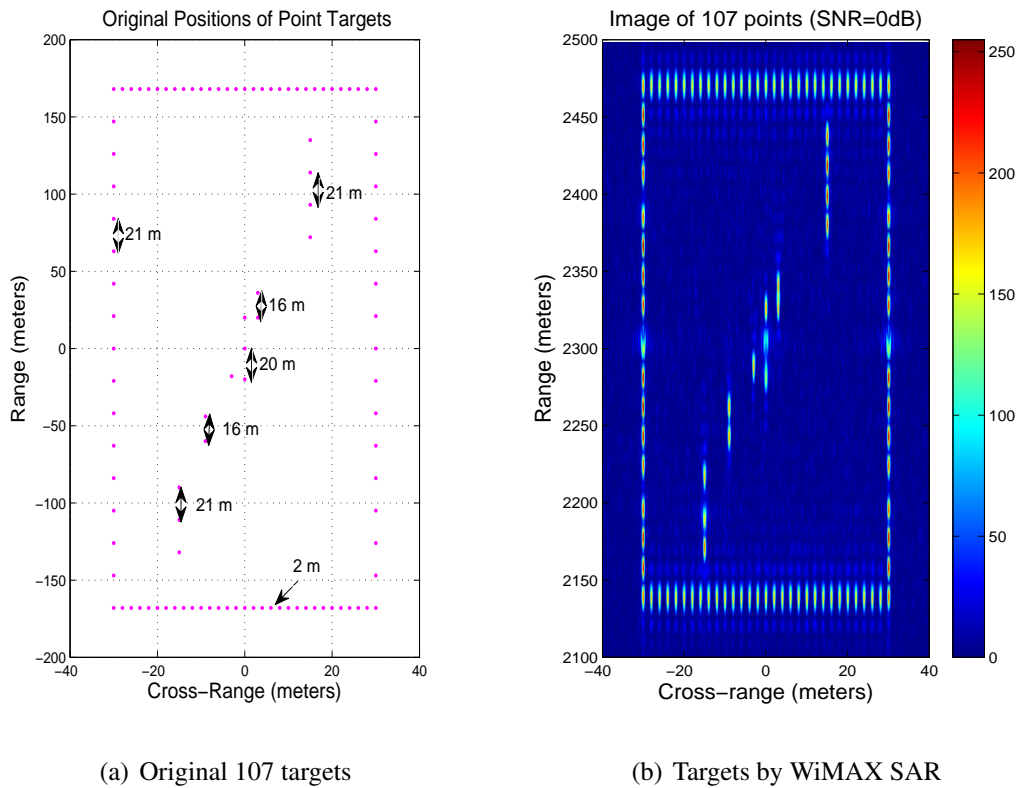


Figure 4.7: WiMAX SAR image for testing its real resolutions. Since the rectangular waveform could cause high sidelobes, the real range resolution could be lower than the theoretical one. Similarly, the sidelobes of antenna beam could widen the pixels in azimuth direction.

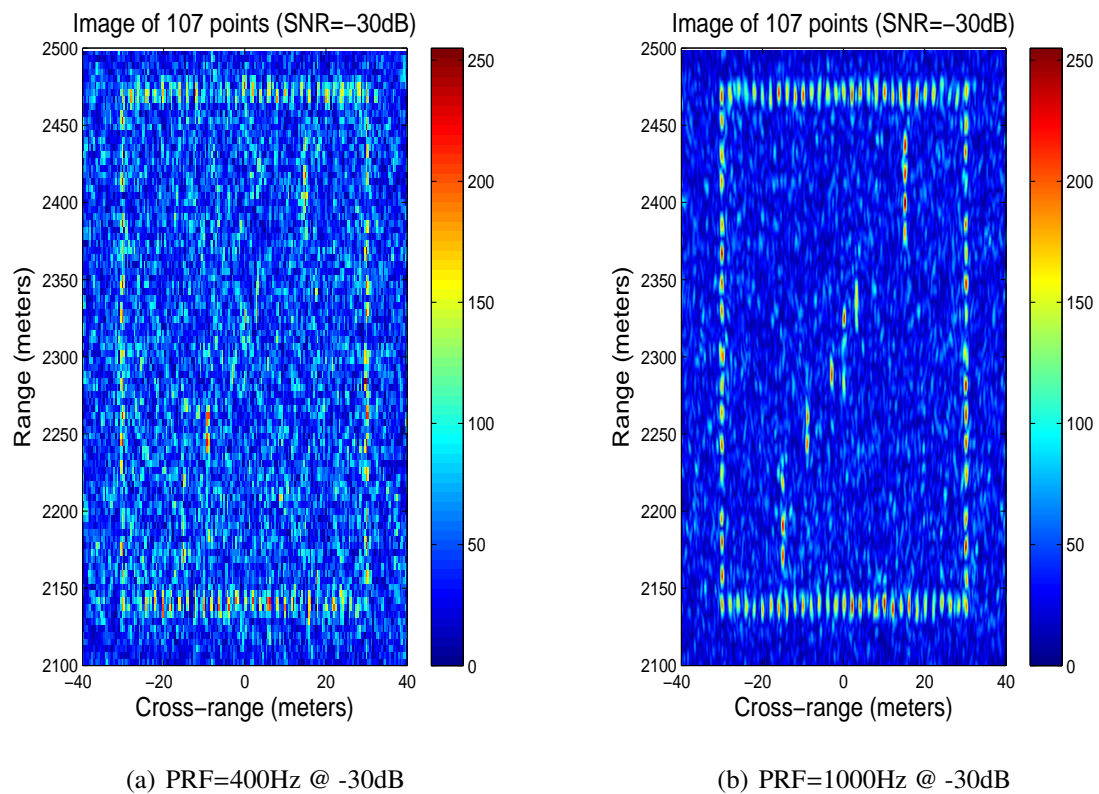


Figure 4.8: Comparison of image quality of WiMAX SAR with different PRF. By increasing the PRF by more than 3dB, the detectability of point targets is much better when the input SNR before signal processing is only -30dB.

4.5.2 Ideal and real WiMAX SAR image

The practical imaging resolutions of WiMAX SAR will be analyzed in this sub-section. Owing to limited length of DSP sequence, there are sidelobes by *sinc* function in the range direction. If a series of aligned targets are close to each other, the sidelobe effect aggravates. Because of this effect, the real ΔR is more than 9.6 m in Figure 4.7(b). Similarly, the beam pattern of planar antenna also causes sidelobes in azimuth domain, which worsens ΔCR of SAR image.

In Figure 4.7, if three or more targets are aligned in range direction, ΔR is increased to 21m. The resolution level also relies on its position (see the case of 16m interval). Due to the sidelobes caused by DSP, the point targets on four sides show a conservatively applicable range and cross-range resolution are 21m and 2m respectively. Figure 4.8 shows even if SNR_{in} is as low as -30dB, above resolutions are still valid as long as PRF is high enough.

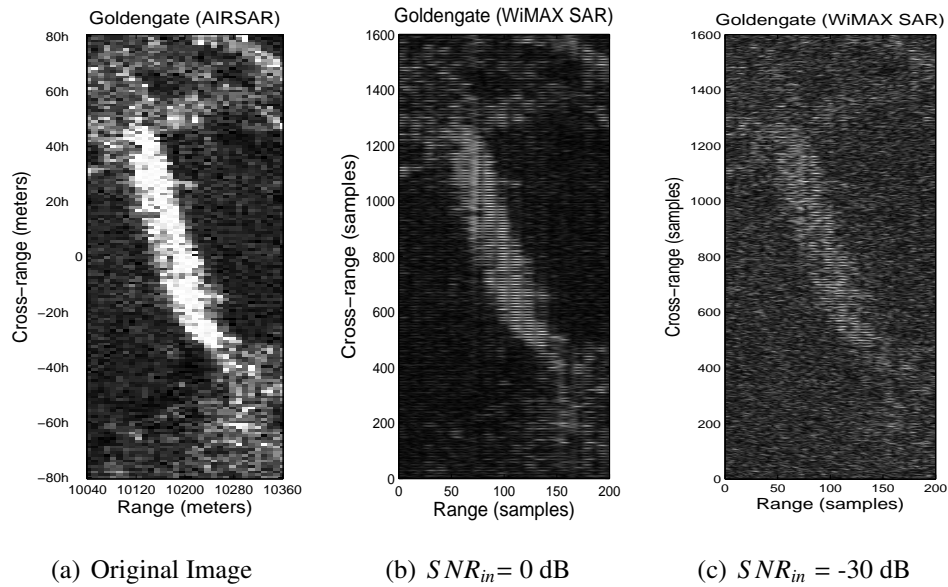


Figure 4.9: Image of Golden Gate Bridge reconstructed by WiMAX SAR. These figures show the imaging capability of WiMAX for distributed targets, whose original SAR image by AirSAR has different range and cross-range resolutions.

As the resolution level limited by the bandwidth of WiMAX, it is practicable for WiMAX SAR to image the contour feature of big targets. Figure 4.9(a) shows image of the Golden Gate Bridge (call it Goldengate in brief), which is truncated from an airborne SAR image of AIRSAR [55] in the mode of 20MHz bandwidth. Figure 4.9(b) and 4.9(c) are the images of Goldengate reconstructed by WiMAX SAR with SNR_{in} of 0 and -30dB respectively. The

former sub-figure is used to demonstrate the imaging capability of WiMAX SAR for distributed targets. We can clearly see the contour of the bridge part in the latter sub-figure, while the contrast of other dimmed part can be easily enhanced by post image processing.

4.5.3 Code correctness verification

As mentioned before, the CP length limits the width of imaging range swath r_{sw} to be around 400m, within which the length of target's echo, used for pulse compression, is as long as an OFDM data symbol. However, if a target is outside the range swath, only part of its echo can be received, and the fraction decreases as the target becomes farther away.

Figure 4.10 shows the effect of CP length upon the image of nine targets, which locate at 2200m, 2300m, 2400m, 2600m, 2800m, 3000m, 3200m, 3400m and 3600m, respectively. The range swath is between 2100m and 2500m. The simulation results illustrate CP can ensure similar imaging intensity for targets within the range swath, whereas the intensity for the target outside range swath decreases as its range increases. As shown in the subfigure of imaging contour, the nine targets are imaged accurately. Thus, Figure 4.10 verifies the correctness of our code to use CP for effective compression of limited range.

If the uniform imaging intensity for whole imaging area is not a necessity, the range swath can be doubled or even tripled. However, it is not the only way to expand range swath. Next chapter will show another way to increase range swath for uniform imaging intensity.

Chirp waveform is the mostly used signal shape in either RAR or SAR. We can utilize the chirp-based SAR image as the reference image, from which how much the image of WiMAX SAR differs can demonstrate the correctness of WiMAX SAR. Given that nine point targets scatter at (-22, 2300), (-20, 2300), (-10, 2180), (0, 2200), (0, 2300), (0, 2450), (22, 2300), (24, 2300) and (25, 2350), Figure 4.11 shows their images reconstructed by ΩKA algorithm with signal shape of chirp (Left) [21] and OFDM (Right) without additive noise. The two pulses in simulation share same signal parameters, such as pulse length, bandwidth and average power. The two subfigures in Figure 4.11 is difficult for eyes to distinguish one from another.

Mean square error (MSE) and peak signal-to-noise ratio (PSNR) are two common error metrics used to compare image compression quality [56], which are easy to evaluate since both

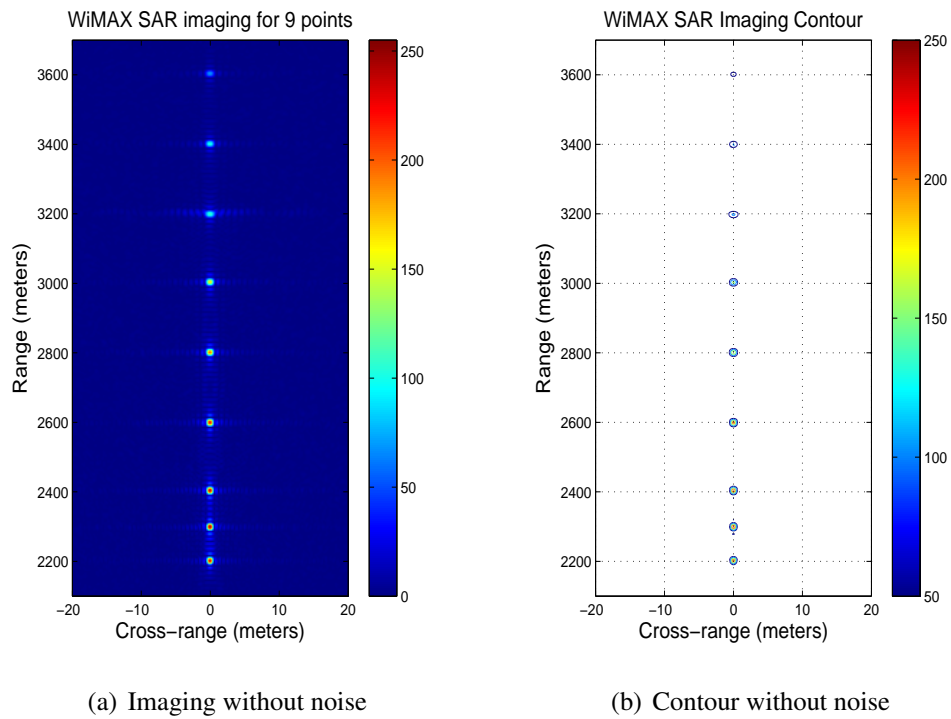


Figure 4.10: Nine point targets are imaged by WiMAX SAR, in which three targets within range swath (2100m-2500m) have uniform high intensity while others' intensities become weak as their range increase.

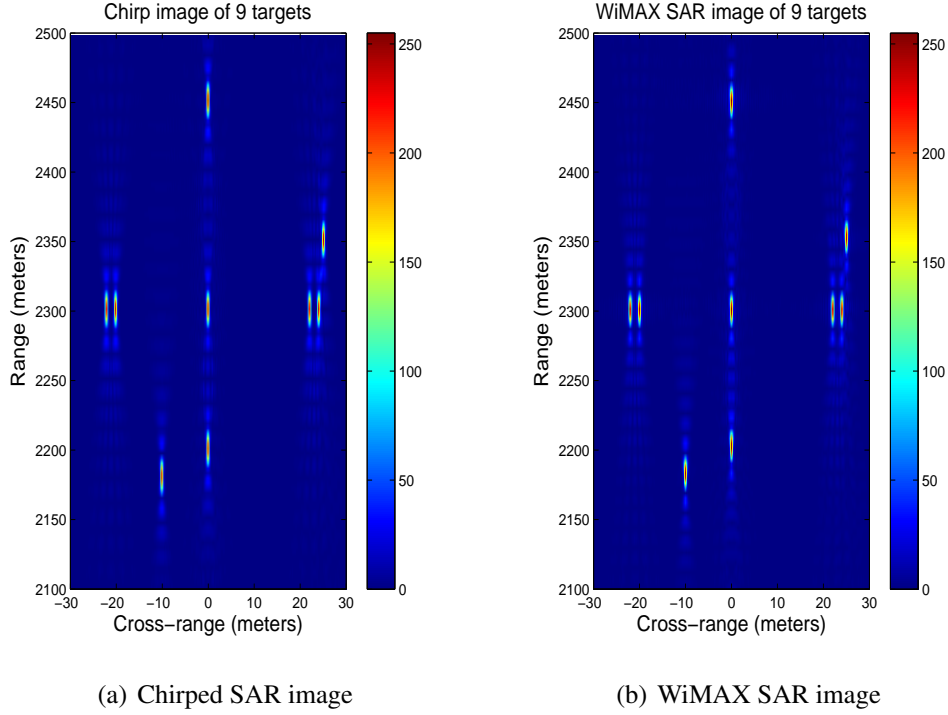


Figure 4.11: Nine point targets are imaged by chirped SAR and WiMAX SAR using ΩKA algorithm without additive noise.

of them are pixel difference-based measures [57]. Therefore, we can use these two metrics to test the correctness of our code for WiMAX SAR by comparing their MSE and PSNR.

The MSE and PSNR can be calculated by following equations:

$$\text{MSE} = \frac{\sum_{m=0, n=0}^{m=M-1, n=N-1} [I_c(m, n) - I_w(m, n)]^2}{M \bullet N}, \quad (4.18)$$

where I_c and I_w are image matrix of chirped SAR and WiMAX SAR respectively, while M and N are number of rows and columns respectively.

$$\text{PSNR} = 10 \log_{10} \left(\frac{P^2}{\text{MSE}} \right), \quad (4.19)$$

where P is the maximum value of image, and it is 255 since it is 8-bit unsigned data. The MSE denotes the cumulative squared error between WiMAX SAR image and the reference chirped SAR image, while PSNR works as a measure of peak error. Higher PSNR means better reconstructed image and lower peak errors. By contrast, the lower the value of MSE,

the smaller the error. By comparing the two measures of WiMAX SAR with chirped SAR, we obtain the PSNR is around 47.6dB while MSE is only around 1.1, which is barely perceptible with pixel value ranging from 0 to 255. Thus, the code for WiMAX SAR is extremely close to that of chirped SAR developed by Soumekh [21].

4.6 Chapter Summary

The chapter proposed an RF front modification to utilize commercial WiMAX base station transceivers in the 5.8GHz ISM band for monostatic stripmap SAR imaging. By the proposed DPDT switch, short pulsed signal can be obtained for the small-range SAR imaging. The increased PRF lowers the required input SNR to expand working range. In addition, the adverse effects of special symbols in a frame and gaps between DL and UL subframes can be overcome by the controlled DPDT switch. We also evaluated the real resolutions of WiMAX SAR by simulation and verified the correctness of the code for WiMAX SAR. Finally, this RF front design could potentially be applied into any other OFDM-based system with large bandwidth or high power for monostatic SAR applications.

Chapter 5

Enhanced WiMAX SAR System Equipped with Multiple Modes

5.1 Chapter Introduction

Widespread use of WiMAX systems has lowered the cost of radio units significantly. Chapter 4 put forward a design of single-mode SAR system which took advantage of the low-cost WiMAX transceiver units. However, the imaging swath width of this system was limited due to the short length of the CP of WiMAX, while the ghost images appear due to rectangular pulse shape. In this chapter, a multi-mode WiMAX SAR is proposed to overcome the limitations. Specifically, we first propose the design of a scan-mode WiMAX SAR, which significantly expands the slant range swath for a wider range of applications. Moreover, spotlight and squint-mode WiMAX SAR are also proposed to enrich imaging applications. Finally, a windowing scheme on the reference data for matched filtering is proposed to reduce ghost images in the range of direction. The validity of proposed design is confirmed through a number of simulation results. In the simulations, we use the widely-adopted ΩKA algorithm to accomplish the multi-mode WiMAX SAR. It is worth noting that the compensation for motion error of airborne SAR system is not considered here, as the error can be directly solved by applying a modified ΩKA algorithm instead [24]. In addition, the platform may be deployed using a UAS due to the light weight of WiMAX SAR.

5.2 System Model of Multi-mode WiMAX SAR

In this section, a simulation model of WiMAX SAR is depicted by a diagram. The way of how this system collect raw data for ΩKA algorithm processing is formulated in a concise manner.

Figure 5.1 shows the block diagram of the system model for simulation, in which the transmitter part from the Encoder to the power amplifier (PA) and the receiver part between the LNA to the FFT are same as WiMAX OFDM PHY [33], while other slight modifications are described as follows.

As mentioned in Chapter 2, many modes of SAR, such as spotlight and scanning SAR, are able to change the direction of antenna during the flight path. Some spaceborne stripmap SARs, like RADARSAT-1 [8], allow the orientation of its fixed antenna to be deviated from the broadside direction for a specific imaging geometry. The SAR is called the squint stripmap SAR, depicted in Figure 2.10, and the WiMAX SAR in this mode is named squint-mode WiMAX SAR. Together with the broadside stripmap mode, a multi-mode WiMAX SAR includes these four modes, which can be achieved by using an antenna steering controller. As mentioned, such a steering can be performed via beamforming with the aid of an FPGA [19]. For the scanning mode, since arriving time instance of the echo backscattered from the target at the nearest range varies from one sub-swath to another, the starting time for the receiver to collect echo data in each sub-swath should be different. Based on the Figure 4.3, a time controller [58] can be used to delay the starts of receiving time for different sub-swaths. As mentioned in previous chapter, a controlled DPDT switch has been used to convert continuous OFDM waveform into pulses for SAR application. The steps of reception after the FFT module are associated with the software design, which can be modified for applying SAR algorithms. To be specific, a memory device follows the FFT to store 2-D raw data of targets' echoes. Afterwards, a signal processing method is used to extract target information by removing transmitted data from echoes, followed by the ΩKA image reconstruction algorithm for multi-mode SAR imaging, since ΩKA is more robust with respect to the alteration of antenna's physical size or squint angle.

WiMAX SAR uses a fixed pulse duration, which is as long as an OFDM symbol defined by WiMAX OFDM PHY [33]. Therefore, the time-domain baseband transmitted OFDM pulse,

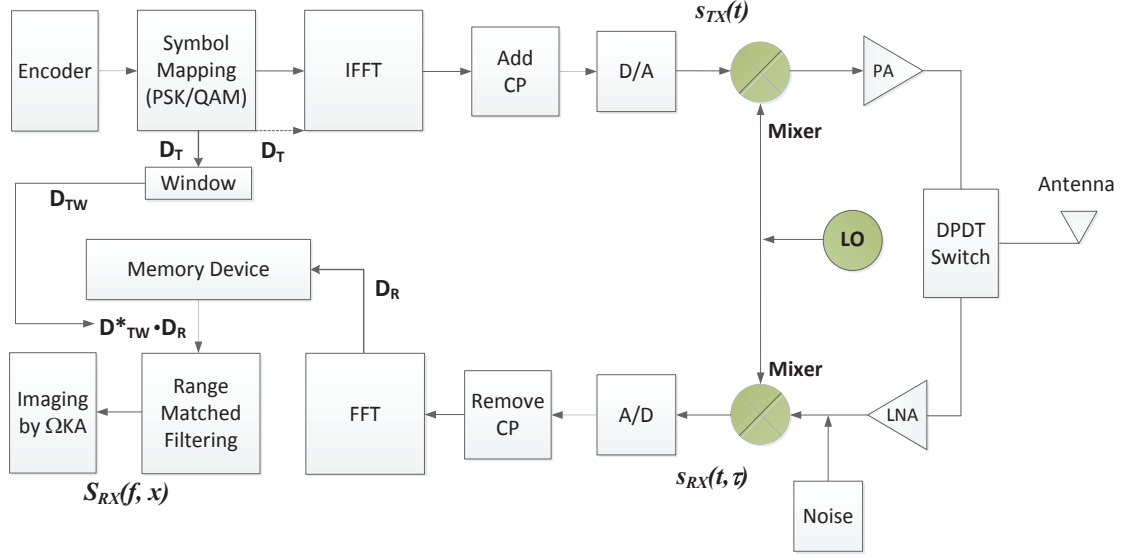


Figure 5.1: Block diagram of the simulation model for proposed multi-mode WiMAX SAR, in which the controlled DPDT module is used for converting continuous OFDM waveform into pulsed shape.

$s_{TX}(t)$, can be denoted as:

$$s_{TX}(t) = IFFT\{D_T\}w_r\left(\frac{t}{T_s}\right) = \frac{1}{N_{sc}} \sum_{m=0}^{N_{sc}-1} D_t(m)\exp(j2\pi f_m t)w_r\left(\frac{t}{T_s}\right), \quad (5.1)$$

where N_{sc} is the number of subcarriers, f_m is the individual subcarrier frequency, $D_T = [D_t(0), D_t(1), \dots, D_t(N_{sc} - 1)]$ is a complex vector of transmission data digitally modulated by PSK or QAM in frequency domain, and w_r represents the envelope shape of OFDM pulse. Moreover, $T_s = T_u + T_g$, where T_s is the total duration of an OFDM symbol, T_u is length of the useful part of the OFDM symbol while T_g represents the guard interval, which generally means the CP.

Figure 5.2 depicts the geometry of WiMAX SAR in the plane of slant range r and azimuth x . As WiMAX SAR transmits a pulse and receives echoes at different time instants within the flight period, the received baseband backscattered echo is defined as $s_{RX}(t, \tau)$, with two time variables t and τ . The pulse propagation time t in slant range, which refers to the speed of light c , is called the fast time; while the echo receiving time τ in cross range, associated with flight speed v of the platform, is called the slow time. In this chapter, we formulate the process of target information acquisition via multi-mode WiMAX SAR system. The received baseband

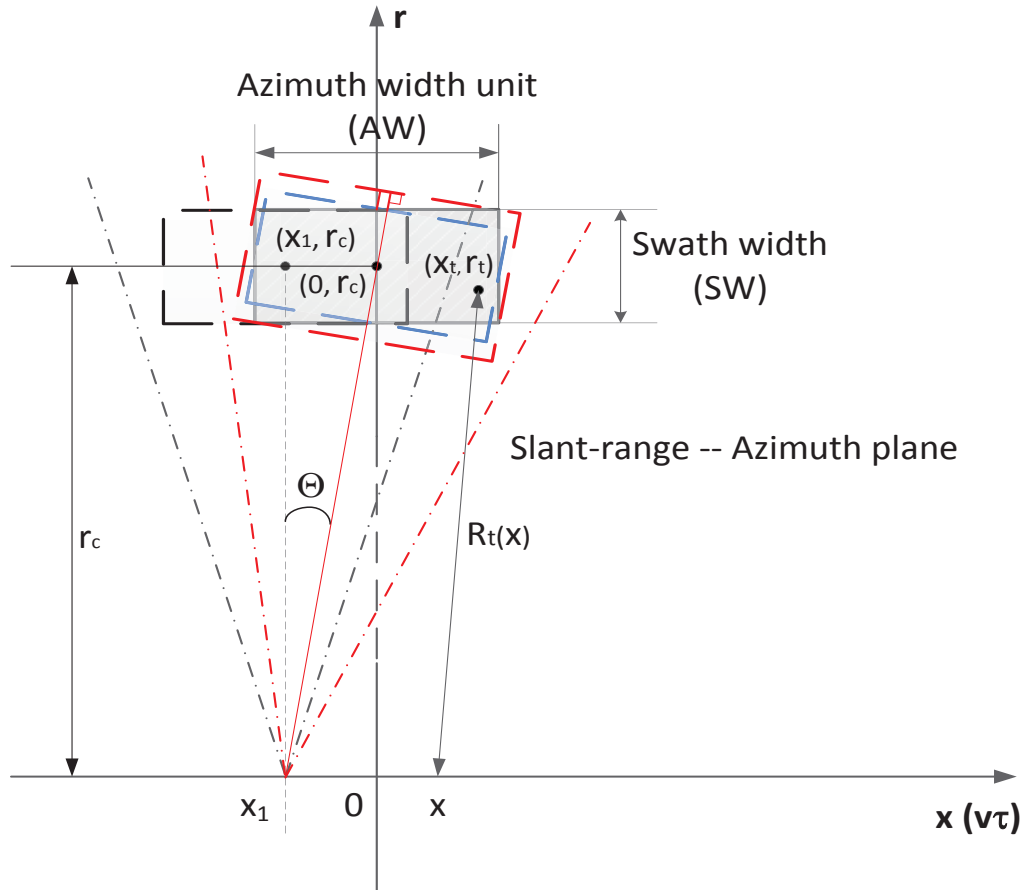


Figure 5.2: Imaging geometry of multi-mode WiMAX SAR. Due to the squint angle Θ , imaging area of spotlight and squint modes (red dashed rectangle) is different from that of stripmap and scan modes (shaded region).

signal, $s_{RX}(t, \tau)$, can be expressed as

$$s_{RX}(t, \tau) = \sigma \frac{A}{N_{sc}} \sum_{m=0}^{N-1} D_t(m) \exp\left(j2\pi f_m \left(t - \frac{2R_t(\tau)}{c}\right)\right) \times \exp\left(j2\pi f_0 \frac{2R_t(\tau)}{c}\right) w_r\left(\frac{t - \frac{2R_t(\tau)}{c}}{T_s}\right) w_{cr}(\tau - \tau_c), \quad (5.2)$$

where σ is radar cross section (RCS) of the target and A is a loss factor caused by WiMAX transceivers and signal transmission media, while f_0 is the carrier frequency and $\exp\left(j2\pi f_0 \frac{2R_t(\tau)}{c}\right)$ is a constant phase delay, which we will abbreviate as P . $\frac{2R_t(\tau)}{c}$ is the delay time of an echo from a target with slant range $R_t(\tau)$ at the slow time τ . Moreover, the antenna beam pattern imposes a weighting factor w_{cr} on the received signal over cross range. Finally, τ_c is the Doppler center, representing the time instant at which the target is in the center of the antenna beam. In order to represent spatial position of the target, x is used to denote the azimuth position $v\tau$, e.g. the absolute Doppler center position x_c is equal to $v\tau_c$. As shown in Figure 5.2, $R_t(x)$ is the instantaneous range from the moving SAR sensor $(x, 0)$ to the target (x_t, r_t) and can be expressed as:

$$R_t(x) = \sqrt{r_t^2 + (x - x_t)^2}. \quad (5.3)$$

In Figure 5.2, the points 0 and x_1 represent the two azimuth positions of the platform. If WiMAX SAR is operating in broadside stripmap mode, the relative Doppler center position is zero [8]. Thus, for the targets (x_1, r_c) and $(0, r_c)$, the absolute Doppler center positions are given by x_1 and 0, respectively. On the other hand, the imaging area is inversely related to the antenna physical size. To be specific, the azimuth width unit (AW) is limited by the 3-dB antenna azimuth beam width at the nearest slant range. Similarly, the 3-dB antenna elevation beam width dictates the size (SW) of range swath or sub-swath in WiMAX SAR.

Figure 5.2 shows the imaging area is the shaded rectangular region if the platform is at 0 position while it is the black dashed rectangle if the sensor is at x_1 position. Assuming WiMAX SAR stops pulse transmission from the position of x_1 , the target (x_t, r_t) cannot be effectively imaged since it is outside of 3-dB beam width drawn by two black dot dash lines. In order to illuminate this target, we can utilize the squint stripmap WiMAX SAR by rotating antenna by an angle of Θ from broadside in clockwise, causing the relative Doppler center position of x_1

rather than 0. The imaging area becomes the blue dashed rectangle, including the target (x_t, r_t) . However, this area does not cover the whole target area of solid rectangle with length of AW and width of SW . Based on equations (C.4) in Appendix C, if the squint angle Θ is small, the area can be covered by increasing the width of blue dashed rectangle by $AW \sin \Theta$ and the length by $SW \sin \Theta$, respectively, shown by the red dashed rectangle. It has been shown that as long as the time for signal to pass through the range swath is shorter than the CP duration T_g , the effect of slow time τ on the OFDM pulse envelope can be ignored. Thus, if $\frac{2R_t(\tau)_{max}}{c} = \frac{2(SW+AW \sin \Theta)}{c}$ is smaller than T_g , which is removed before FFT, the envelope shape in equation (5.2) is $w_r\left(\frac{t}{T_u}\right)$. Replacing τ with x , the received frequency-domain data vector produced by the OFDM pulse remover, shown in Figure 5.1, at any position x is formulated as:

$$D_R(f, x) = \sigma A P D_T \circ DL\left(-\frac{2R_t(x)}{c}\right) \otimes \mathbf{W}_r(f) w_{cr}(x - x_c), \quad (5.4)$$

where \circ represents Hadamard product while \otimes means circular convolution. And $DL(p) = [1, \exp(j2\pi f_1 p), \dots, \exp(j2\pi f_{N-1} p)]$ is the phase delay vector, which depends on a target's slant range, while $\mathbf{W}_r(f)$ is the envelope vector of the slant-range in the frequency domain. Multiplying $D_R(f, x)$ by complex conjugate of the D_{TW} in Figure 5.1, we can obtain the range information at a cross-range position, x , as:

$$\begin{aligned} S_{RX}(f, x) &= D_R(f, x) \circ D_{TW}^* = D_R(f, x) \circ D_T^* \circ W \\ &= \sigma A |D_T|^2 \circ W \circ PDL\left(-\frac{2R_t(x)}{c}\right) \otimes \mathbf{W}_r(f) w_{cr}(x - x_c), \end{aligned} \quad (5.5)$$

where W represents the windowing for the reference data D_T^* . The delay vector DL is combined with constant phase P , yielding $PDL\left(-\frac{2R_t(x)}{c}\right) = [\exp(-j\frac{4\pi}{c} f_0 R_t(x)), \dots, \exp(-j\frac{4\pi}{c} (f_0 + f_{N-1}) R_t(x))] = [\exp(-j\frac{2}{c} \omega_0 R_t(x)), \dots, \exp(-j\frac{2}{c} \omega_{N-1} R_t(x))] = [\exp(-j2k_0 R_t(x)), \dots, \exp(-j2k_{N-1} R_t(x))]$, where $\omega = 2\pi f$ is angular frequency and k denotes the wavenumber. Since $R_t(x)$ is not linear, MSP (See Appendix A) requires to be applied into equation (5.5), yielding the $\omega - k$ domain received

digital signal as

$$S_{RX}(\omega, k_x) = \sigma A |D_T|^2 \circ \mathbf{W} \circ \mathbf{KDL} \otimes \mathbf{W}_r(\omega) \otimes \mathbf{W}_{cr}(k_x), \quad (5.6)$$

where $\mathbf{KDL} = [\exp(jg(k_0)), \exp(jg(k_1)), \dots, \exp(jg(k_{N-1}))]$, in which $g(k) = -\sqrt{4k^2 - k_x^2} r_t - k_x x_t + 2kr_c - \pi/4$, while $\mathbf{W}_r(\omega)$, $\mathbf{W}_{cr}(k_x)$ are the envelope vectors of the target's echo in the $\omega - k$ domain. Since equation (5.6) is just the superimposition form of equation (2.30). The following steps (equations (2.31) to (2.33)) of ΩKA algorithm can be used on the $S_{RX}(\omega, k_x)$ to obtain the target's 2-D position.

5.3 Scan-mode WiMAX SAR

Due to the restriction on CP length, we design a scan-mode WiMAX SAR for swath expansion, whose operating range and geometry is illustrated in this section.

5.3.1 Operating range

The target of a truck, an aircraft or a small vessel can be viewed as one or several point targets when their physical sizes are comparable to the resolution of a SAR sensor. In comparison to the common radar, SAR enjoys more signal processing gains, including the gains in range G_{rsp} and azimuth G_{asp} domains, which can be written as [46]:

$$\begin{cases} G_{rsp} = \frac{T_u B}{L_{rsp}} = \frac{T_u c}{2\Delta R L_{rsp}}. \\ G_{asp} = \frac{N_p}{L_{asp}} = f_{pr} \frac{L_{am}}{\alpha v} \cdot \frac{1}{L_{asp}}, \end{cases} \quad (5.7)$$

where T_u is the useful OFDM symbol length, B is the noise bandwidth, c is the speed of light and ΔR is the range resolution; N_p is the effective number of pulses for imaging one point target, f_{pr} is the PRF, v is the platform velocity, while L_{rsp} and L_{asp} are signal processing losses for range and azimuth, respectively. To avoid confusion, the aperture size for stripmap SAR is denoted as L_{am} and it can be expressed as $L_{am} = \Delta CR_0 = \frac{R\lambda}{2\Delta CR_m}$ [6], where ΔCR_0 is the cross-range resolution of RAR, while ΔCR_m is the cross-range resolution for stripmap SAR. Finally,

α is an adjustment factor for different modes of this WiMAX SAR, resulting in aperture size $L_a = \frac{L_{am}}{\alpha}$. Compared with required input SNR SNR_{req} in Chapter 4, the image signal-to-noise ratio (SNR_{im}) [8] of the multi-mode WiMAX SAR is given by,

$$\begin{aligned} SNR_{im} &= SNR_{req} G_{rsp} G_{asp} \\ &= \frac{P_t G_a^2 \lambda^2 \sigma}{(4\pi)^3 R^4 k_b T B F_n L_t} \cdot \frac{T_u c}{2 \Delta R L_{rsp}} \cdot \frac{f_{pr} R \lambda}{2 v \alpha \Delta C R_0 L_{asp}} \\ &= \frac{P_t f_{pr} T_u G_a^2 \lambda^3 c \sigma}{4 (4\pi)^3 R^3 k_b T B F_n L v \Delta R \Delta C R}, \end{aligned} \quad (5.8)$$

where $\Delta C R$ is the cross-range resolution of the specific mode, which is equal to $\alpha \Delta C R_0$, while L is the system loss, which is a product of the loss from propagation and hardwares, L_t , and the loss from signal processing $L_{rsp} L_{asp}$.

5.3.2 Geometry

In a spaceborne scan-mode SAR system, high PRF is used for satisfying Doppler bandwidth requirement. However, due to the long slant range, the stripmap SAR's aperture size L_{am} is also very large. Consequently, multiple looks can be carried out for each sub-swath. It is customary to call the look *a burst* with length of L_b meters. This burst repeats periodically every L_p meters. Due to the short operating range, multi-mode WiMAX SAR possesses a small aperture size, in which only one burst is transmitted. Thus, the high-precision SAR algorithms, such as $\Omega K A$, can be directly applied in the burst processing [59]. Figure 5.3 describes the behavior of bursts in each sub-swath for scan-mode SAR applications. In order to keep the azimuth image resolution uniform, the equation $L_{am} \geq L_p + L_b$ must be satisfied [9].

As mentioned in section II, the starting time for the reception is changed when a new sub-swath is being imaged. As far as the range swath of WiMAX SAR is concerned, the range swath is limited by the duration of CP T_g . Thus, the maximum range swath $S W_{max}$ is,

$$S W_{max} = \frac{c T_g}{2}. \quad (5.9)$$

According to current standard [33], the maximum CP length of WiMAX systems in unlicensed band is $\frac{25}{9} \mu s$, which results in a limited range swath of around 400m. In fact, the effective

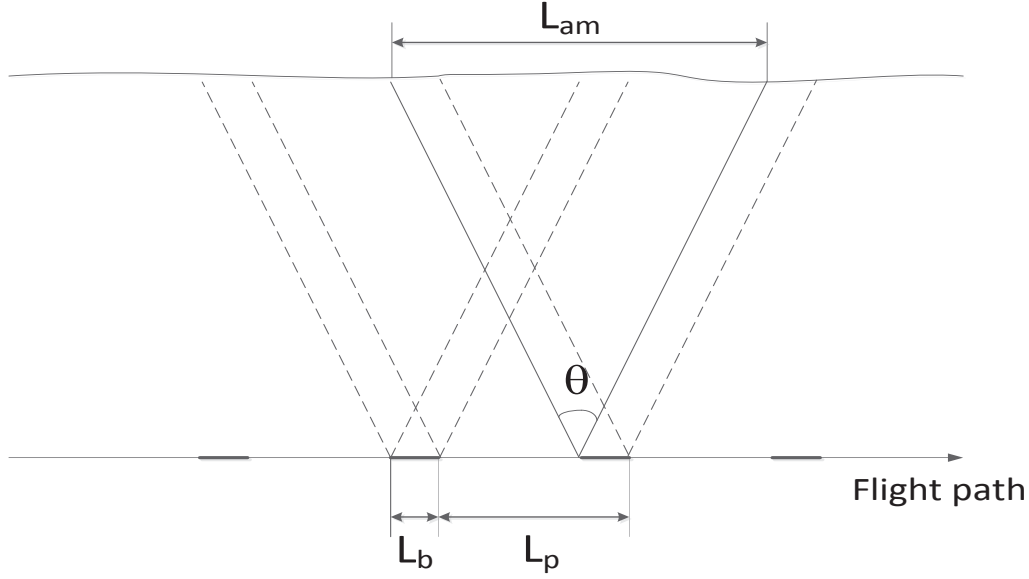


Figure 5.3: Geometry of scan-mode SAR imaging for one sub-swath. L_b is the burst length in which SAR transmits and receives while L_p is the repetition interval of two neighboring bursts. L_{am} is the aperture size of stripmap SAR.

swath is a bit narrower than 400m due to the comparatively coarse range resolution ΔR of WiMAX SAR. For the squint-mode or spotlight WiMAX SAR, when the squint angle is small, their SW and AW should satisfy the equation $SW + AW \sin \Theta < 400\text{m}$, in order to illuminate same area size as stripmap WiMAX SAR does. Microwave radiation in free space can pass a range interval of nearly 2100m twice over a pulse duration of $\frac{125}{9}\mu\text{s}$. Therefore, the closest slant range of WiMAX SAR is 2100m and we can set six sub-swaths, each with an effective width of 350m, in the slant range as shown in Figure 5.4. Assuming a flight height of 1050m, the maximum graze angle becomes 30° . We adopt the whole swath from 2125m to 4225m (the slant ranges within two red lines). By steering the antenna in elevation direction five times, scan-mode WiMAX SAR can reach farthest range of 4225m and finish one scanning process, thereby increasing swath width to 2100m. Once the EIRP is not restricted by the regulation in unlicensed band or the required image quality is lower, the range swath of 2100m situated in farther range can be easily imaged by delaying the start time of receiver processing.

In Figure 5.4, we can see six sub-swaths are used to cover the slant range swath of 2100m, and the maximum rotation angle within a whole scan is θ_1 , which is only $27.1 - 23.3 = 3.8^\circ$. The coverage of scan-mode WiMAX SAR is shown in Figure 5.5, where the numbers 5, 18.5,

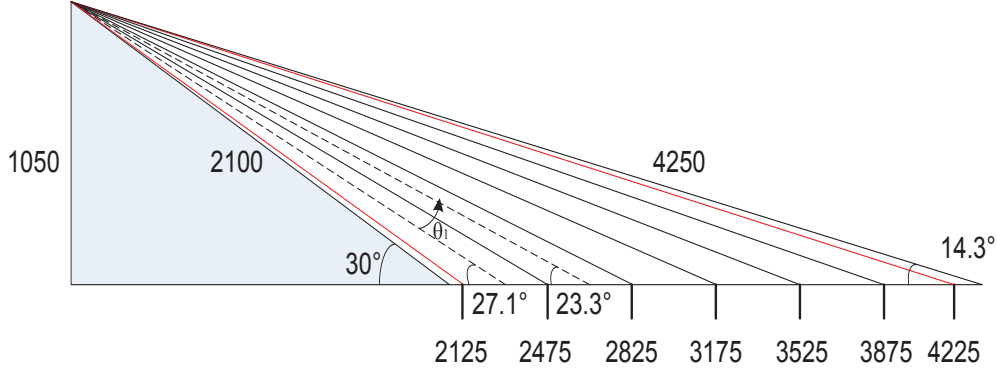


Figure 5.4: Geometry of scan-mode WiMAX SAR in range-height domain.

33.5, 50, 68, 87.5 represent x_c for different sub-swaths, while the azimuth imaging unit length L_u in cross range is set to be 100m, in which the WiMAX SAR ends burst transmission at the 96m. In fact, L_u is the same as L_p in Figure 5.3. The antenna azimuth beam width, which is L_{am} as mentioned before, becomes wider as the slant range grows. Since the slant range varies slightly within each narrow sub-swath, we define the effective aperture size L_{am} as,

$$L_{am} \approx r_c \frac{\lambda_c}{D_a} = r_c \frac{c}{f_c D_a}, \quad (5.10)$$

where r_c is the slant range from SAR sensor to the center of each sub-swath, D_a is the antenna azimuth size, $f_c = 5.805\text{GHz}$ is center carrier frequency, while c is the speed of light. The designed sub-aperture burst size L_b and corresponding L_{am} for different sub-swaths are shown in Table 5.1. To keep the azimuth resolutions in all sub-swaths similar [9], the variation of L_b , from one to another, is around 1/15 of L_{am} for any sub-swath. It is clear that $L_{am} > L_u + L_b$. The speed of UAS, as the platform of WiMAX SAR, is given by 50 m/s. Since the interval between two bursts is set as 3m within a scanning period in Figure 5.5, the scan-mode WiMAX SAR has $3/50 = 0.06\text{s}$ to finish antenna beam steering from one sub-swath to another. The time duration is enough for current beamforming systems [19]. The antenna beam patterns in all sub-swaths requires correction to avoid scalloping effect, yet causing uneven noise distribution for the imaging [9]. In order to reduce this noise effect, the images of closer three sub-swaths are formed by combining two looks, while the remaining three sub-swaths are reconstructed by only one look.

Table 5.1: Burst and center aperture size of each sub-swath

L_b (m)	L_{am} (m)
10	148.5
11	171
13	193.8
14	216.4
16	239
17	261.6

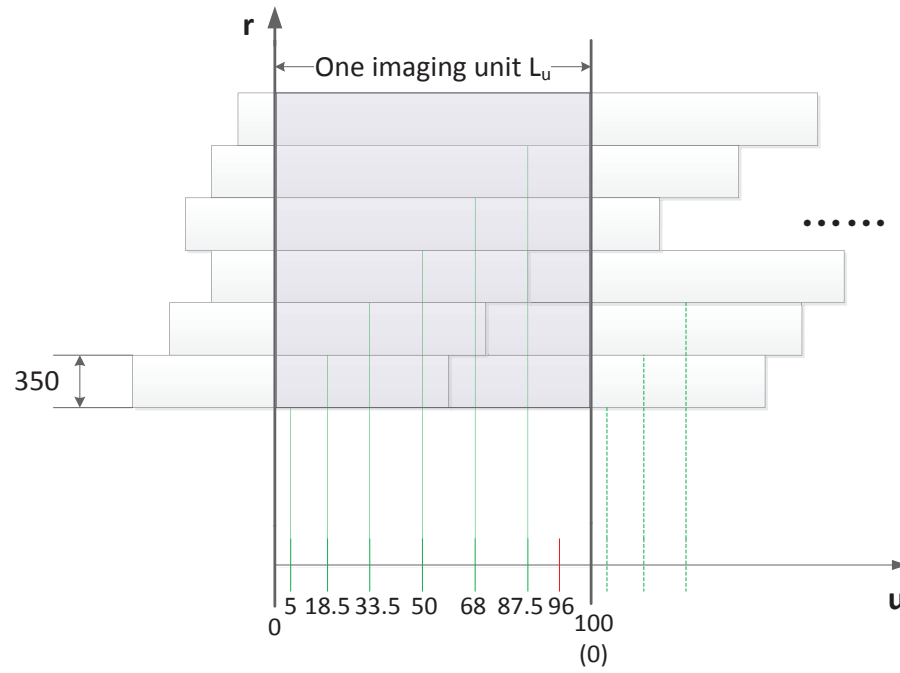


Figure 5.5: Imaging area of scan-mode WiMAX SAR, where the shaded rectangular region is the imaging area in one scanning process. The Doppler center positions x_c for different sub-swaths are given by green lines.

5.4 Simulation Results

This section presents the simulation results of multiple modes of WiMAX SAR and the windowing effect. As shown in equation (5.8), the image SNR SNR_{im} declines quickly with the increase of WiMAX SAR's slant range. The effective isotropic radiated power (EIRP) of WiMAX SAR is limited by regulations in unlicensed band. The burst length L_b , as the effective aperture size L_a of scan-mode WiMAX SAR, is only 1/15 of aperture size of stripmap SAR L_{am} . Accordingly, the α of scan mode is 15 in equation (5.8), causing almost 12dB lower SNR_{im} than that of stripmap WiMAX SAR. Thus, the EIRP limitation, for working range and detectable RCS of a target, is more severe in the scan-mode WiMAX SAR.

Since the EIRP of WiMAX SAR in 5.8GHz unlicensed band is 24dBm, $P_t = -3\text{dBm}$ and $G_a = 27\text{dBi}$ are set to satisfy this EIRP. To obtain finest range resolution, the bandwidth B is set to be 20MHz, which is the largest optional value in the unlicensed band [33]. Like the stripmap WiMAX SAR, the theoretical range resolution of scan-mode WiMAX SAR is 9.6m. Considering the given SW_{max} and G_a of this system, the elevation size D_e and azimuth size D_a of antenna of multi-mode WiMAX SAR are set as 0.3m and 0.8m, respectively, based on basic equations for antenna's beamwidth and gain [6]. Thus, its cross-range resolution is $\Delta CR = \alpha \Delta CR_0 = \alpha \frac{D_a}{2} = 15 \times \frac{0.8}{2} = 6\text{m}$.

We can derive that the number of effective pixels in the imaging area for one sub-swath is around $\frac{100 \times 350}{9.6 \times 6} \approx 608\text{m}^2$. For the point-target detection, a false alarm rate of 10^{-4} is low enough, which requires the SNR of 15dB for ensuring detection rate to be over 0.999 [7]. Based on the analysis in Chapter 3, the minimum SNR_{im} is 15dB for multi-mode WiMAX SAR to form an interpretable image. Since the median RCS of a small vessel, with length of 50m and width of 10m, is 30000m^2 [51], we set the RCS of a point target within one pixel ($9.6\text{m} \times 6\text{m}$) as $\sigma = 3000\text{m}^2$ for following scan-mode simulations except in Figure 5.7. If f_{pr} is set as 2000Hz for increasing G_{asp} for larger imaging range, T_u is the useful OFDM symbol length of $\frac{100}{9}\mu\text{s}$ [33], $\lambda = 0.0517\text{m}$, while $F_n = 4\text{dB}$, $L = 3\text{dB}$, $v = 50\text{m/s}$ and $c = 3 \times 10^8\text{m/s}$, the minimum image SNR SNR_{im}^{min} corresponding to range sub-swaths can be calculated.

Table 5.2 lists the SNR_{im}^{min} corresponding to different slant range R with target RCS of 3000m^2 . According to equation (5.8), the operating range of scan-mode WiMAX SAR is

between 2125m and 4225m, while the farthest range of other modes can be over 10km. By contrast, if the maximum range for the stripmap mode is set as 4225m, the target RCS can be as low as 200m^2 , which is the RCS level of a truck [6]. Figure 5.6 compares the difference of

Table 5.2: The image SNR for different slant range of scan mode

R (m)	2475	2825	3175	3525	3875	4225
SNR_{im}^{min} (dB)	27.32	25.59	24.07	22.71	21.48	20.35

swath widths for stripmap and scan-mode WiMAX SAR images of point targets. Due to its

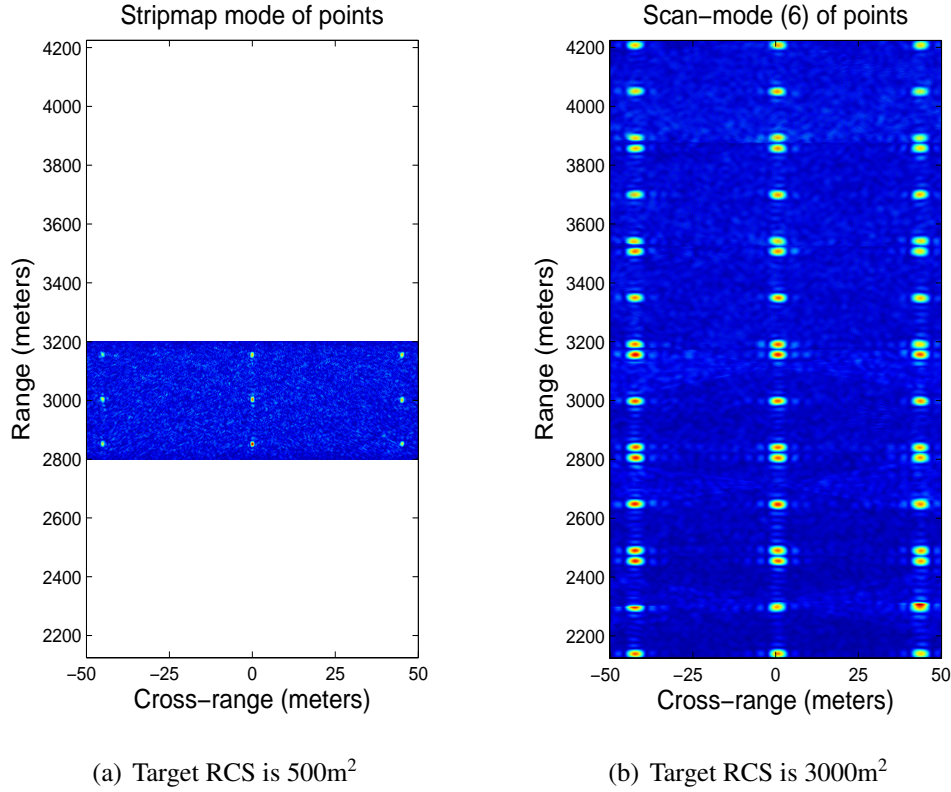


Figure 5.6: Comparison of images between stripmap and scan mode. The range swath of stripmap mode is 350m while the scan mode is 2100m. However, the cross-range resolution of stripmap WiMAX SAR is much finer.

larger range swath, the scan-mode WiMAX SAR is used initially for surveillance applications, while the spotlight WiMAX SAR is used to obtain finer details of the target of interest. Figure 5.7 compares the images of point targets produced by above-mentioned two modes. Unlike the stripmap SAR, the cross-range resolution of the spotlight SAR is not fixed by a given D_a and it

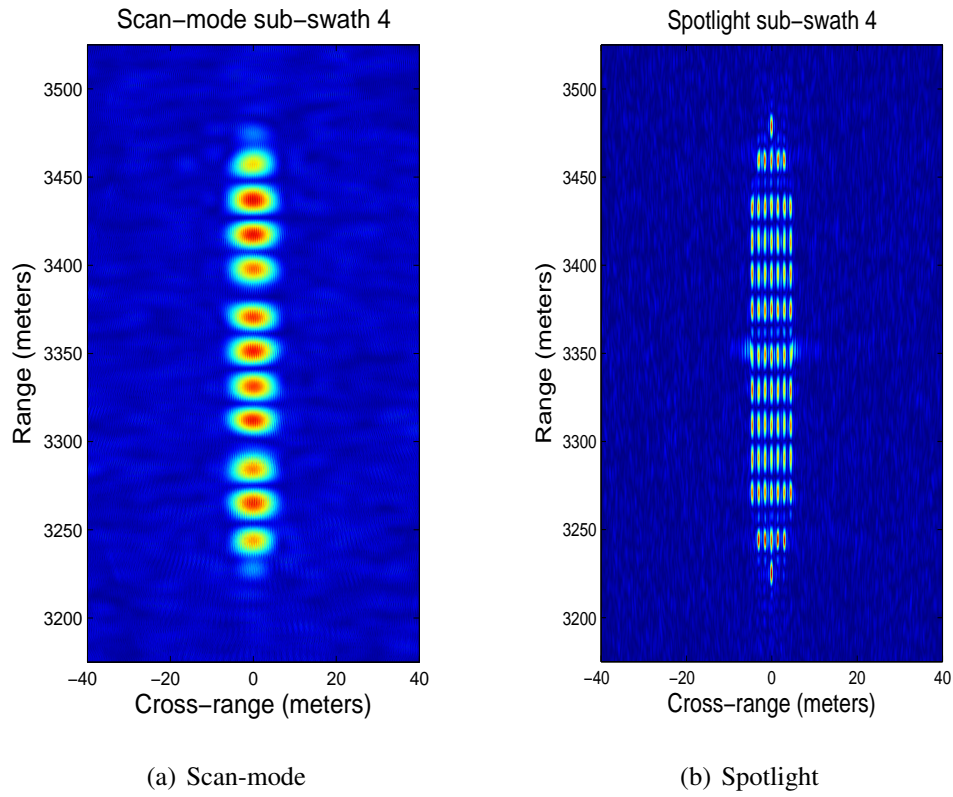


Figure 5.7: Comparison of images of 75 point targets with RCS of 200m^2 between scan and spotlight modes. The cross-range spacing of two targets is only 1.5m and the slant range swath is 350m.

can be altered by using the different aperture sizes. As shown in Figure 5.5, for the farthest two sub-swaths, the full imaging only requires one look when the image Doppler center position has deviated from the burst center. The targets in these two sub-swaths can be imaged by squint-mode WiMAX SAR by pointing the antenna to the center of target area via beamforming, without beam-pattern correction. Figure 5.8 illustrates the image of the farthest sub-swath and compares it with the image reconstructed by the broadside stripmap mode without antenna beam correction. We notice that the three targets on the left-hand side are dimmed in broadside mode. In Figure 5.9, a scan-mode WiMAX SAR image with reference data of D_T is compared

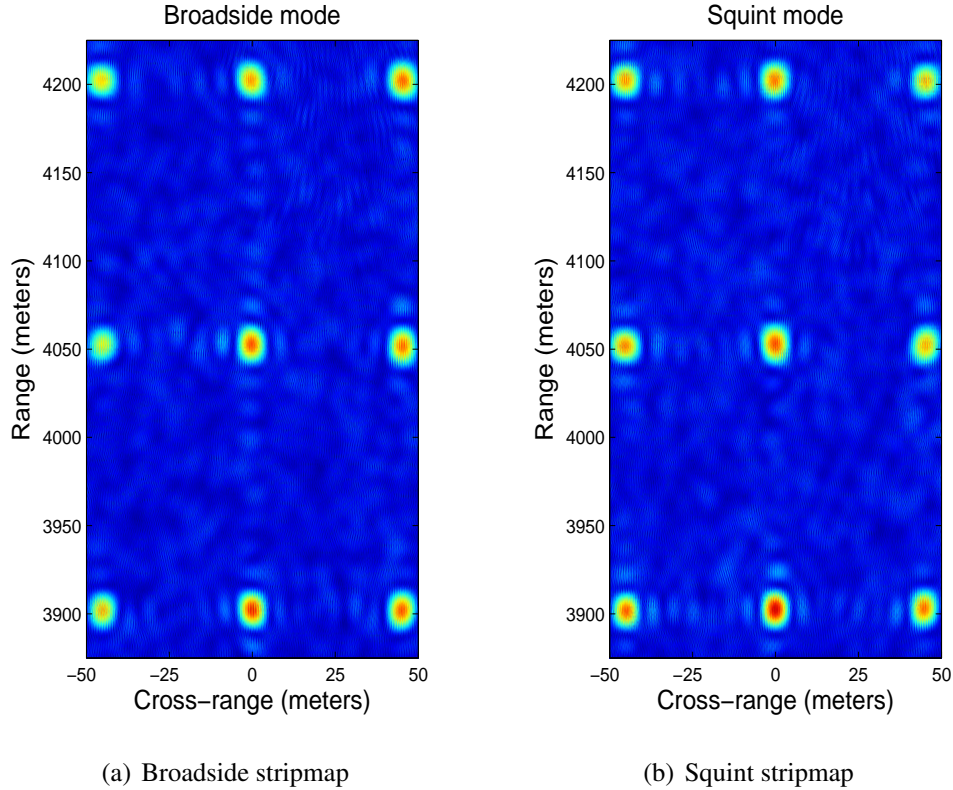


Figure 5.8: Comparison between broadside and squint stripmap modes for imaging the farthest sub-swath. Target RCS is 3000m^2 and Doppler center position x_c is 37.5m instead of 0m .

with that of D_{TW} , in which the ghost images are significantly inhibited by windowing the reference data.

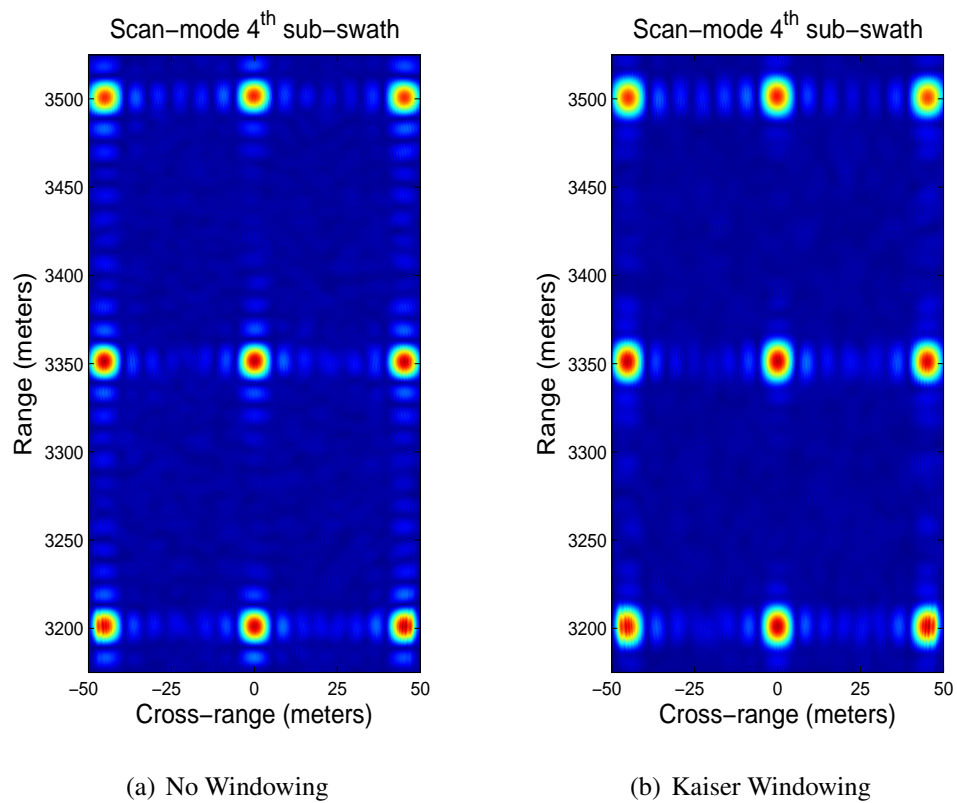


Figure 5.9: Comparison of images for 4th sub-swath in scan-mode WiMAX SAR with and without windowing. The ghost images in range direction are reduced by this scheme.

5.5 Evaluation of WiMAX SAR

Compared with the parameters in last chapter for the stripmap WiMAX SAR, here the antenna gain G_a is 4dB lower while the PRF f_{pr} is 3dB higher. To obtain interpretable SAR image as shown in Figure 5.6, RCS of target in Table 4.1 needs to be doubled at least. Table 5.3 summarizes the range of WiMAX SAR in stripmap mode for imaging different steady targets.

Table 5.3: Estimated working ranges for targets of different RCS by stripmap WiMAX SAR

Target	RCS (m^2)	Range (m)
Aircraft	20	2500
Truck	200	4200
Ship	3000	10000

The table reveals the WiMAX SAR is a small range airborne SAR working on comparatively large targets. It can be utilized for searching cars and ships in distress or crashed aircraft. Thus, it caters for the industrial interest of timely data acquisition for search and rescue.

On the other hand, WiMAX SAR have advantages as well as disadvantages in comparison to other existing or proposed SAR systems. Table 5.4 compares WiMAX SAR with other similar SAR systems in terms of cost, signal form, application parameters and so forth.

Table 5.4: WiMAX SAR in comparison with other similar SAR systems

	UWB-OFDM SAR [2]	WiMAX-based Passive SAR [3]	microASAR [30]	WiMAX SAR
Pros	High range resolution of cm-level	Large range (> 10 km)	CW chirp signal with constant envelope; 1.25m resolutions	Low component cost (\approx 200 USD); Easy to get; Multiple modes; Signal diversity
Cons	Very small range of only 40m	Complicated receiver; Unreliable system; Low range resolution	Relatively high component cost (> 2000 USD)	High PAPR, Low range resolution (\approx 10 m); Small range

5.6 Chapter Summary

This chapter proposed a design to equip stripmap WiMAX SAR with various imaging modes, which reinforces the functionality of WiMAX SAR. To be specific, the scanning mode expands the range swath by more than five times, while the spotlight mode provides more details about particular point targets. Further, the squint mode can be used for avoiding uneven noise due to antenna beam pattern compensation used in scanning mode. Finally, the operating ranges of stripmap WiMAX SAR for targets with different RCS were listed, and an objective assessment of WiMAX SAR was given in comparison with some comparable airborne SAR designs. So far, the simulation of multi-mode WiMAX SAR has been done and it could arouse further interests from industry in future to put the design into experiment for search and rescue and other applications.

Chapter 6

Conclusion and Future Work

6.1 Conclusion

The background and fundamentals of SAR and OFDM-based WiMAX were first introduced. Afterwards, the technical similarities between SAR and WiMAX were discussed to show the feasibility of utilizing WiMAX base station transceivers for a SAR sensor, followed by a discussion of several challenges for the WiMAX-based SAR system.

To overcome most of the challenges, Chapter 4 developed a system approach to exploit WiMAX for broadside stripmap SAR imaging. With the aid of a fast DPDT switch, two WiMAX base station transceivers were exploited to collaboratively work in order to generate appropriate pulsed signal for airborne SAR application. The WiMAX receiver was utilized for the processing of range pulse compression in frequency domain for the following Ω KA algorithm. The imaging swath of the stripmap WiMAX SAR is narrower than 400m due to the limited length of CP for circular convolution between transmitted pulse and channel information. At last, the code correctness was demonstrated by simulation results, such as comparing the image of WiMAX SAR with that of chirped SAR.

With the cutting-edge techniques, such as smart antenna and high-speed time controller, Chapter 5 proposed a design for scan-mode WiMAX SAR to significantly enlarge the range swath to be 2100m. Based on the available model of the scanning WiMAX SAR, broadside and squint spotlight modes, as well as squint stripmap mode were also integrated to enable a multi-mode WiMAX SAR, enriching its applications. A evaluation of WiMAX SAR was given

in the end of this chapter to summarize the features of the SAR design.

In addition, the second chapter depicted SAR techniques in a concise way, which is quite conducive to readers in other fields for understanding SAR principles rapidly.

In summary, the thesis pioneered a way to leverage commercial WiMAX base stations for airborne SAR. Although the proposed WiMAX SAR sensor is constrained by regulations in unlicensed band and incompatibility of two techniques in different fields, it will contribute to the advancement of civil SAR sensors by taking advantage of ubiquitous wireless devices.

6.2 Future Research

The most meaningful work for next step is to implement the proposed scheme by real-world measurement using available unlicensed WiMAX base stations and a cost-effective platform, such as a UAS. During the experiment of data measurement, some issues could be found for further optimizing WiMAX SAR.

Once the real raw data is collected by the experiment, the relatively coarse range resolution can be dramatically improved by utilizing the acquired data to estimate more precise range information. The estimation method is usually called superresolution, such as the bandwidth extrapolation and the compressive sensing.

The main bottleneck of WiMAX SAR is its limited transmitting power and antenna gain regulated by FCC for 5.8GHz unlicensed band, which restricts its operating range or RCS of imaged targets. If WiMAX SAR can obviate the EIRP restrictions by combining other techniques, its working range will be increased while required target's RCS can be reduced, thereby expanding the domain of both application and research for WiMAX SAR. For example, more efficient algorithms, such as the spectral analysis algorithm (SPECAN), could be applied for scan-mode WiMAX SAR to facilitate the processing of numerous raw data.

Additionally, the proposed scheme in Chapter 4 wastes transmitted power since DPDT switch only extracts a small fraction of transmitted continuous symbols in a subframe. If the frame length of WiMAX or other appropriate OFDM-based systems can be further shortened by speeding up the digital signal processors in future, the DPDT switch may not be required while the transmitted power can be mostly utilized since the frame duration is no longer a

problem for the minimum range of WiMAX SAR.

With the expansion of coverage area, the symbol length could be increased for future OFDM-based wireless systems, thereby widening the range swath of WiMAX SAR. This will provide more opportunities for its development.

Finally, even if the real measurement cannot be carried out soon due to various reasons, the real RCS model and speckle noise model could be added in the simulations of WiMAX SAR.

Appendix A

Derivation of Eq. (2.30) using MSP

Before deriving this equation by using the Method of Stationary Phase (MSP) [60], we should review the a few concepts and formula.

The wavenumber k is equal to $\frac{\omega}{c} = \frac{2\pi}{\lambda}$.

The Gamma function is

$$\Gamma(a) = \int_0^{\infty} u^{a-1} e^{-u} du, \quad a > 0. \quad (\text{A.1})$$

And $a = 1/2$ yields:

$$\Gamma\left(\frac{1}{2}\right) = \int_0^{\infty} u^{\frac{1}{2}-1} e^{-u} du = 2 \int_0^{\infty} e^{-v^2} dv = \sqrt{\pi}. \quad (\text{A.2})$$

MSP shows the value of integral in this form $I(k) = \int_p^q f(x) e^{jk g(x)} dx$ counts not only on the $f(x)$ and $g(x)$ at the points of p and q , but also on the those points within (p, q) , in which $g(x)$ get extreme values. These points are called stationary points.

If the n -order derivative of $g(x_0)$ is not zero while its derivatives in lower order are all zeros and n is even, the $I(k)$ satisfies the following equation:

$$I(k) = 2f(x_0) e^{jk g(x_0)} \frac{\Gamma(1/n) e^{j\frac{\pi}{2n}}}{n \sqrt[n]{kg^{(n)}(x_0)/n!}}, \quad x_0 \in (p, q) \quad (\text{A.3})$$

And $n=2$ yields:

$$I(k) = 2f(x_0)e^{jk g(x_0)} \frac{\Gamma(1/2)e^{j\frac{\pi}{4}}}{2\sqrt{k g''(x_0)/2}} = e^{j\frac{\pi}{4}} f(x_0)e^{jk g(x_0)} \sqrt{\frac{2\pi}{k g''(x_0)}}, \quad x_0 \in (p, q) \quad (\text{A.4})$$

As for the instantaneous slant range $R_t(\tau)$ of equation (2.25) in the Chapter 2, the $g(x)$ equals to $-2\sqrt{r_t^2 + (x - x_t)^2} - \frac{k_x}{k}x$, which yields

$$g'(x) = \frac{-2(x - x_t)}{\sqrt{r_t^2 + (x - x_t)^2}} - \frac{k_x}{k} = 0, \quad (\text{A.5})$$

which yields $x_0 = \frac{k_x}{\sqrt{4k^2 - k_x^2}}r_t + x_t$. Then we have

$$jk g(x_0) = -2jk \sqrt{r_t^2 + (x_0 - x_t)^2} - k_x x_0 = -j(\sqrt{4k^2 - k_x^2}r_t + k_x x_t). \quad (\text{A.6})$$

Here the k and k_x are two phasors of different directions and they have the relation [23] as $\sqrt{4k^2 - k_x^2} = k_r$, where k_r is orthogonal to k_x .

Thus, the phase history of target (r_t, x_t) in wavenumber domain (k_r, k_x) is

$$\Phi_k = k g(x_0) = -k_r r_t - k_x x_t, \quad (\text{A.7})$$

It is linear and the target position can be obtained simply by the inverse Fourier transform (IFT) or inverse fast Fourier transform (IFFT) for discrete signal.

On the other hand, the $g''(x_0)$ can be calculated by:

$$g''(x_0) = -2 \left(\frac{4k^2 - k_x^2}{4k^2} \right)^{\frac{3}{2}}. \quad (\text{A.8})$$

Thus, based on (A.6) and (A.8), equation (A.4) is derived to be:

$$I(k) = e^{j\frac{\pi}{4} - j\frac{\pi}{2}} \sqrt{\frac{\pi}{k} \left(\frac{4k^2}{4k^2 - k_x^2} \right)^{\frac{3}{2}}} f(x_0) e^{jk g(x_0)} = \sqrt{\frac{\pi}{k} \left(\frac{4k^2}{4k^2 - k_x^2} \right)^{\frac{3}{2}}} f(x_0) e^{-j(\sqrt{4k^2 - k_x^2}r_t + k_x x_t) - j\frac{\pi}{4}}. \quad (\text{A.9})$$

Appendix B

Target's cross-range resolution of squint spotlight SAR

In Section 2.3, we have shown the features of spotlight SAR. As shown in the Figure 2.8, the cross-range resolution in equation (2.22) is valid only for the conventional broadside spotlight SAR. However, spotlight SAR can also work in squint mode. For the squint spotlight SAR, the cross-range resolution for targets varies slightly from the commonly broadside spotlight SAR when squint angle is small. This is because its effective aperture size is lower than the flight path L_x . It is noteworthy that the selected SAR imaging algorithm is still ΩKA , whose advantage was detailed before. Thus, the targets within the image area could have same azimuth resolution in reconstructed SAR image. Figure B.1 shows the geometry of the squint spotlight SAR, where Θ is squint angle when the SAR sensor is located at the center of its flight path. R_n is the range between SAR sensor and the target with coordinate values of (x_n, r_n) , while r_c is the distance from flight path to the center of imaging area. As the target here is at the center of imaging area, then $r_n = r_c$. If both x_n and L_x are much less than r_c , we have

$$r_{xq} = \sqrt{\left(x_n - \frac{L_x}{2}\right)^2 + r_c^2} \approx \sqrt{x_n^2 + r_c^2} = R_n, \quad (\text{B.1})$$

where r_{xq} is the range in the case of squint mode.

According to equations (2.22) and (B.1), we can derive the cross-range resolution for squint

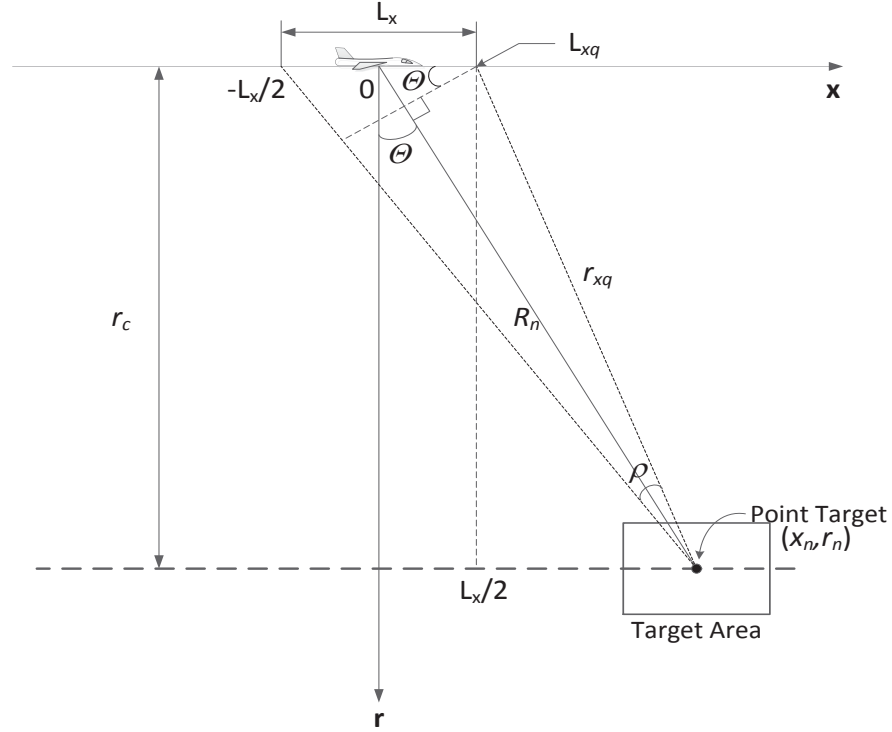


Figure B.1: Target cross-range resolution for the squint spotlight SAR.

spotlight SAR as,

$$\Delta CR = \frac{\lambda}{2\rho} = \frac{r_{xq}\lambda}{2L_{xq}} \approx \frac{R_n\lambda}{2L_x\cos\Theta} = \frac{r_c\lambda}{2L_x\cos^2\Theta}, \quad (\text{B.2})$$

where ρ is the rotation angle of the antenna beam while λ is the wavelength. Based on equation (B.2), it is easy to see the cross-range resolution of squint spotlight SAR becomes poorer when the squint angle Θ increases.

As detailed in Chapter 2, the targets within the imaging area can share the same azimuth resolution ΔCR as that of the target (x_n, r_n) , located at the center if ΩKA algorithm is applied to reconstruct the SAR image.

Appendix C

Area expansion due to squint angle

For squint-mode stripmap or spotlight SAR with small squint angle, the imaging area requires to be expanded to cover the whole imaging area of their corresponding broadside mode. Figure C.1 shows the geometry of this expansion, where the red rectangle represents the original image area of broadside-mode SAR, while blue dashed rectangle and green rectangle denote the imaging areas of squint-mode SAR rotated by Θ degree before with and without imaging area enlargement, respectively. The purple lines mark the expansion amount in range and azimuth width by Δ_{sw} and Δ_{aw} . The imaging area of interest is the red rectangle, of which range swath r_{sw} and azimuth unit width r_{aw} are two sides.

In order to calculate the augmentation parameters Δ_{sw} and Δ_{aw} , we can first define two variables x_{sw} and y_{sw} , which constitute the range swath r_{sw} by this equation,

$$r_{sw} = 2x_{sw} + y_{sw}. \quad (C.1)$$

According to the geometric relation in Figure C.1, the azimuth unit width r_{aw} is derived as,

$$r_{aw} = x_{sw} \tan \Theta + \frac{2y_{sw}}{\tan \Theta}. \quad (C.2)$$

Combining these two equations above, the augmentation parameters Δ_{sw} and Δ_{aw} is described

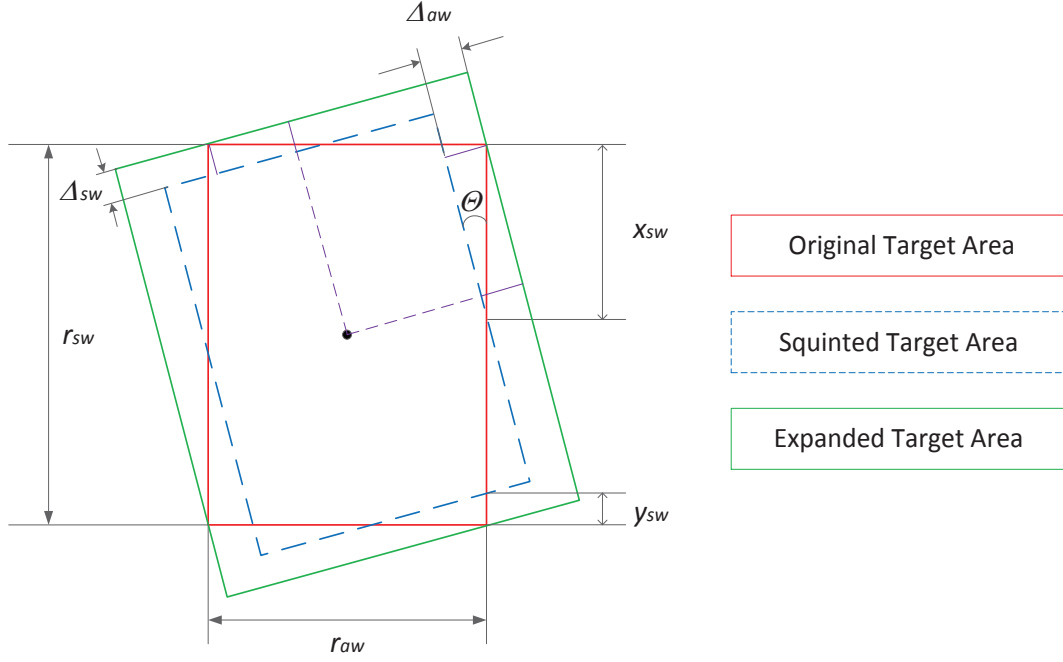


Figure C.1: Area expansion in spotlight or squint SAR, where Θ is squint angle.

by the functions of x_{sw} , y_{sw} and Θ as,

$$\begin{cases} \Delta_{sw} = y_{sw} \cos \Theta = \frac{2r_{aw} - r_{sw} \tan \Theta}{4 - \tan^2 \Theta} \sin \Theta, \\ \Delta_{aw} = x_{sw} \sin \Theta = \frac{2r_{sw} - r_{aw} \tan \Theta}{4 - \tan^2 \Theta} \sin \Theta. \end{cases} \quad (\text{C.3})$$

It is readily to notice that if Θ is close to zero, these augmentations can be approximate to

$$\begin{cases} \Delta_{sw} \approx \frac{r_{aw}}{2} \sin \Theta, \\ \Delta_{aw} \approx \frac{r_{sw}}{2} \sin \Theta. \end{cases} \quad (\text{C.4})$$

Appendix D

Key developed Matlab code

```
WiMAX signal generation START
% nPulses is the number of symbol pulses of stripmap SAR during flight path
nFFT = 256;    % Number of FFT points
nPSK = 4;
LenDataSeq = nFFT*nPulses;
fracCP = 1/4;    LenCP = ceil(fracCP*nFFT);    % Length of CP
dataSource = randsrc(1, LenDataSeq, 0:nPSK-1);
dataMod = pskmod(dataSource, nPSK);    % QPSK modulated transmitted data
GUARD1 = complex (0,0) * ones (28,1);
DC = complex (0,0);
GUARD2 = complex (0,0) * ones (27,1);
nRow = nFFT;
nCol = nPulses;
matrixMod = reshape(dataMod, nRow, nCol);
matrixMod(1:28,:) = GUARD1*ones(1,m);
matrixMod(129,:) = DC*ones(1,m);    % matrixMod is the matrix of nPulses
matrixMod(230:256,:) = GUARD2*ones(1,m);    % OFDM data symbols of WiMAX
matrixMod = matrixMod*sqrt(256/200);    % normalize its average power
cpBegin = nFFT-LenCP;
cpEnd = nFFT;
cpMatrix=zeros(LenCP,nCol);
ifftDataMatrix = zeros(nRow,nCol);
ifftTotMatrix = zeros(nRow+LenCP,nCol);
for iPls = 1:nCol,
    ifftDataMatrix(:,iPls) = ifft((matrixMod(:,iPls)),nFFT);
    for jCP = 1:LenCP,
        cpMatrix(jCP,iPls) = ifftDataMatrix(jCP+cpBegin,iPls);
    end
    ifftTotMatrix(:,iPls) = vertcat(cpMatrix(:,iPls),ifftDataMatrix(:,iPls));
end
wimaxTXBaseband = ifftTotMatrix;    % WiMAX baseband transmitted signal
```

WiMAX signal generation END

Range Pulse Compression by CP START

```

% wimaxRXBb is the received WiMAX baseband echo signal
wimaxRXBb(1:LenCP,:) = [];    % Remove CP of echo data
wimaxRXBb(257:end,:) = [];    % Extract echo of a symbol length
wimaxFreqRX = fft(wimaxRXBb,nFFT);
wimaxFreqMF = wimaxFreqRX.*conj(matrixMod);    % Range matched filtering
wMatrix = w'*ones(1,nPulses);    % Angular frequency matrix
Rc = rswHalf;    % Relative reference range is close to half-size of
                % the range swath if range is much larger than range swath
wimaxFreqMF = exp(j*wMatrix*2*Rc/c).*wimaxFreqMF;
% Offset reference range of OFDM data symbols as (4.14), and j is imaginary unit

```

Range Pulse Compression by CP END

Modification for scan mode START

```

nPulses = 2*ceil(LxHalf/da);    % LxHalf is half aperture size of stripmap SAR and da is the
                                % sample spacing, equaling to v/PRF
a = da*(-nPulses/2:nPulses/2-1);    % a is synthetic array of stripmap SAR
nPulsesScan = 2*ceil(ScanLxHalf/da); % ScanLxHalf is half aperture size of a subswath in
                                % scan mode and nPulsesScan is the number of pulses
a(1:nPulses/2-1-nPulsesScan/2) = pi;
a(nPulses/2+nPulsesScan/2:end) = pi;
ofs = ceil(offset/da);    % offset is spacing from a subswath's Doppler center to image center
a = circshift(a,[0,ofs]);
[row,scanArray] = find(a~=pi);    % scanArray shows effective aperture positions
beginScan = scanArray(1)-nPulses/2-1;
aScan = da*(beginScan:beginScan+nPulsesScan-1); % Now we get aScan as the subswath's
                                                % synthetic array of scan mode

```

Modification for scan mode END

Bibliography

- [1] N. Levanon, "Multifrequency Complementary Phase-coded Radar Signal," *Radar, Sonar and Navigation, IEE Proceedings*, vol. 147, no. 6, pp. 276–284, 2000.
- [2] D. Garmatyuk, "Simulated Imaging Performance of UWB SAR Based on OFDM," in *Ultra-Wideband, The IEEE International Conference on*, 2006, pp. 237–242.
- [3] J. Arroyo, "Passive Synthetic Aperture Radar Imaging Using Commercial OFDM Communication Networks," Ph.D. dissertation, Air Force Institute of Technology, Ohio, U.S., 2012.
- [4] E. Zaugg, D. Hudson, and D. Long, "The BYU SAR: A Small, Student-Built SAR for UAV Operation," in *Geoscience and Remote Sensing Symposium, 2006. IGARSS 2006. IEEE International Conference on*, July 2006, pp. 411–414.
- [5] Atmel(R)Corporation. (2007) Atmel Announces WiMAX Transceiver with Low RF Cost. Internet draft. [Online]. Available: <http://news.thomasnet.com/fullstory/Single-Chip-Transceiver-is-designed-for-WiMAX-applications-516587>
- [6] M. Richards, *Fundamentals of Radar Signal Processing*, ser. Professional Engineering. McGraw-hill, 2005.
- [7] D. K. Barton, *Radar System Analysis and Modeling*, ser. Artech House radar library. Artech House, 2005.
- [8] I. Cumming and F. Wong, *Digital Signal Processing of Synthetic Aperture Radar Data: Algorithms and Implementation*, ser. Artech House signal processing library. Artech House, 2005.
- [9] G. Franceschetti and R. Lanari, *Synthetic Aperture Radar Processing*, ser. Electronic engineering systems series. Taylor & Francis, 1999.
- [10] R. O'Donnell. (2010) Radar Cross Section. Internet draft. [Online]. Available: http://aess.cs.unh.edu/Radar%202010%20PDFs/Radar%202009%20A_7%20Radar%20Cross%20Section%201.pdf
- [11] J. Zyl and Y. Kim, *Synthetic Aperture Radar Polarimetry*. Wiley, 2011.
- [12] C. Balanis, *Antenna Theory: Analysis and Design*. Wiley, 2012.

- [13] W. M. Brown and L. J. Porcello, "An Introduction to Synthetic-Aperture Radar," *Spectrum, IEEE*, vol. 6, no. 9, pp. 52–62, 1969.
- [14] D. Massonnet and J. Souyris, *Imaging with Synthetic Aperture Radar*, ser. Engineering sciences: Electrical engineering. EFPL Press, 2008.
- [15] *IEEE 100 The Authoritative Dictionary of IEEE Standards Terms Seventh Edition*, IEEE Std. 100-2000, 2000.
- [16] J. L. Walker, "Range-Doppler Imaging of Rotating Objects," *Aerospace and Electronic Systems, IEEE Transactions on*, vol. AES-16, no. 1, pp. 23–52, Jan 1980.
- [17] R. Moore, J. Claassen, and Y. H. Lin, "Scanning Spaceborne Synthetic Aperture Radar With Integrated Radiometer," *Aerospace and Electronic Systems, IEEE Transactions on*, vol. AES-17, no. 3, pp. 410–421, May 1981.
- [18] C. Chang, M. Jin, and J. Curlander, "Squint Mode SAR Processing Algorithms," in *Geoscience and Remote Sensing Symposium, 1989. IGARSS'89. 12th Canadian Symposium on Remote Sensing., 1989 International*, vol. 3, Jul 1989, pp. 1702–1706.
- [19] C. Dick, F. Harris, M. Pajic, and D. Vuletic, "Real-time QRD-based Beamforming on An FPGA Platform," in *Signals, Systems and Computers, 2006. ACSSC '06. Fortieth Asilomar Conference on*, Oct 2006, pp. 1200–1204.
- [20] R. Raney, H. Runge, R. Bamler, I. Cumming, and F. Wong, "Precision SAR Processing Using Chirp Scaling," *Geoscience and Remote Sensing, IEEE Transactions on*, vol. 32, no. 4, pp. 786–799, Jul 1994.
- [21] M. Soumekh, *Synthetic Aperture Radar Signal Processing: with MATLAB Algorithms*. John Wiley & Sons, 1999.
- [22] R. H. Stolt, "Migration by Fourier Transform," *Geophysics*, vol. 43, no. 1, pp. 23–48, Feb 1978.
- [23] C. Cafforio, C. Prati, and F. Rocca, "SAR Data Focusing Using Seismic Migration Techniques," *Aerospace and Electronic Systems, IEEE Transactions on*, vol. 27, no. 2, pp. 194–207, Mar 1991.
- [24] A. Reigber, E. Alivizatos, A. Potsis, and A. Moreira, "Extended Wavenumber-domain Synthetic Aperture Radar Focusing with Integrated Motion Compensation," *Radar, Sonar and Navigation, IEE Proceedings*, vol. 153, no. 3, pp. 301–310, June 2006.
- [25] Y. Shoji, C.-S. Choi, and H. Ogawa, "70-GHz-Band OFDM Transceivers Based on Self-Heterodyne Scheme for Millimeter-Wave Wireless Personal Area Network," *Microwave Theory and Techniques, IEEE Transactions on*, vol. 54, no. 10, pp. 3664–3674, Oct 2006.
- [26] W. Carrara, R. Goodman, and R. Majewski, *Spotlight Synthetic Aperture Radar: Signal Processing Algorithms*, ser. Artech House signal processing library. Artech House, 1995.

- [27] A. Moreira, P. Prats-Iraola, M. Younis, G. Krieger, I. Hajnsek, and K. Papathanassiou, "A Tutorial on Synthetic Aperture Radar," *Geoscience and Remote Sensing Magazine, IEEE*, vol. 1, no. 1, pp. 6–43, March 2013.
- [28] A. Reigber *et al.*, "Very-High-Resolution Airborne Synthetic Aperture Radar Imaging: Signal Processing and Applications," *Proceedings of the IEEE*, vol. 101, no. 3, pp. 759–783, March 2013.
- [29] B. D. Huxtable, C. R. Jackson, A. W. Mansfield, and H. Rais, "Synthetic Aperture Radar Processing System for Search and Rescue," *Proc. SPIE*, vol. 3069, pp. 185–192, 1997.
- [30] M. Edwards *et al.*, "MicroASAR: A Small, Robust LFM-CW SAR for Operation on UAVs and Small Aircraft," in *Geoscience and Remote Sensing Symposium, 2008. IGARSS 2008. IEEE International*, vol. 5, July 2008, pp. V–514—V–517.
- [31] R. Chang, "Synthesis of Band-Limited Orthogonal Signals for Multichannel Data Transmission," *Bell System Technical Journal*, vol. 45, pp. 1775–1796, December 1966.
- [32] WiMAX Forum, "Industry Research Report," WiMAX Forum, 462 Stevens Ave, Suite 309 Solana Beach, CA 92075, Tech. Rep., 2011.
- [33] *IEEE Standard for Air Interface for Broadband Wireless Access Systems*, IEEE Std. 802.16-2012, 2012.
- [34] *IEEE Standard for Information Technology–Telecommunications and Information Exchange Between Systems Local and Metropolitan Area Networks–Specific Requirements Part 11: Wireless LAN Medium Access Control (MAC) and Physical Layer (PHY) Specifications*, IEEE Std. 802.11-2012, 2012.
- [35] R. Moore, "Tradeoff Between Picture Element Dimensions and Noncoherent Averaging in Side-Looking Airborne Radar," *Aerospace and Electronic Systems, IEEE Transactions on*, vol. AES-15, no. 5, pp. 697–708, Sept 1979.
- [36] Z. Abate, *WiMAX RF Systems Engineering*, ser. Artech House Mobile Communications. Artech House, 2009.
- [37] M. Long, *Radar Reflectivity of Land and Sea*, 3rd ed., ser. Radar Library.
- [38] S. Chehrazi *et al.*, "A 6.5 GHz Wideband CMOS Low Noise Amplifier for Multi-band Use," in *Custom Integrated Circuits Conference, 2005. Proceedings of the IEEE 2005*, 2005, pp. 801–804.
- [39] Lyrtech. (2009) WiMAX RF Module. Internet draft. [Online]. Available: <http://www.dspecialists.com>
- [40] J. Arroyo and J. Jackson, "SAR Imaging Using WiMAX OFDM PHY," in *Radar Conference (RADAR), 2011 IEEE*, 2011, pp. 129–134.

- [41] J. G. Andrews, A. Ghosh, and R. Muhamed, *Fundamentals of WiMAX: Understanding Broadband Wireless Networking*, ser. Prentice Hall Communications Engineering and Emerging Technologies. Upper Saddle River, NJ, USA: Prentice Hall PTR, 2007.
- [42] Spectrum Engineering Branch, "Canadian Proposals for The WRC-03 on 5GHz RLAN Issues," Industry Canada, PPT, 2002.
- [43] D. North, "An Analysis of The Factors Which Determine Signal/Noise Discrimination in Pulsed-Carrier Systems," *Proceedings of the IEEE*, vol. 51, no. 7, pp. 1016–1027, 1963.
- [44] S. Kay, *Fundamentals of Statistical Signal Processing: Detection Theory*, ser. Prentice Hall Signal Processing Series. Prentice-Hall PTR, 1998.
- [45] S. Rice, *Mathematical Analysis of Random Noise*, ser. Bell Telephone System Technical Publications. American Telephone and Telegraph Company.
- [46] R. Raney, "Radar Fundamentals: Technical Perspective," in *Principles and Applications of Imaging Radar, Manual of Remote Sensing*, F. Henderson and A. Lewis, Eds. 3 ed., pp. 9–130, 1998.
- [47] R. M. Gray, "Toeplitz and Circulant Matrices: A Review," *Foundations and Trends in Communications and Information Theory*, 2006.
- [48] C. Sturm, T. Zwick, and W. Wiesbeck, "An OFDM System Concept for Joint Radar and Communications Operations," in *Vehicular Technology Conference. VTC Spring 2009. IEEE 69th*, April 2009, pp. 1–5.
- [49] AIR802. (2014) FCC Rules and Regulations. Internet draft. [Online]. Available: <http://www.air802.com/files/FCC-Rules-and-Regulations.pdf>
- [50] L. Cimini and N. Sollenberger, "Peak-to-Average Power Ratio Reduction of An OFDM Signal Using Partial Transmit Sequences," *Communications Letters, IEEE*, vol. 4, no. 3, pp. 86–88, March 2000.
- [51] I. Harre. (2004) RCS in Radar Range Calculations for Maritime Targets. Internet draft. [Online]. Available: <http://www.mar-it.de/Radar/RCS/rcs.htm>
- [52] UMCC. (2013) SR-U000-TS DPDT Switch. [Online]. Available: <http://www.everythingrf.com/products/switches/umcc/613-101-sr-u000-ts>
- [53] G. Rebeiz *et al.*, "The Search for A Reliable MEMS Switch," *Microwave Magazine, IEEE*, vol. 14, no. 1, pp. 57–67, Jan 2013.
- [54] P. Hindle, "The State of RF/Microwave Switches," *Microwave Journal*, vol. 53, no. 11, pp. 20–36, November 2010.
- [55] JPL. (1988-2004) Airborne Synthetic Aperture Aadar (AIRSAR). [Online]. Available: <http://airsar.jpl.nasa.gov/>

- [56] R. C. Gonzalez and R. E. Woods, *Digital Image Processing*. Reading, Mass., Menlo Park, Calif., New York: Addison-Wesley Publishing Company, 1992, includes bibliographical references and index. [Online]. Available: <http://alpha.lib.uwo.ca/record=b2161785>
- [57] I. Avcibas, I. Avcba, B. Sankur, and K. Sayood, "Statistical Evaluation of Image Quality Measures," *Journal of Electronic Imaging*, vol. 11, pp. 206–223, 2002.
- [58] ONSemiconductor. (2014) MC1455B: Timer Circuit. [Online]. Available: <http://www.onsemi.com/PowerSolutions/product.do?id=MC1455B>
- [59] R. Bamler and M. Eineder, "ScanSAR Processing Using Standard High Precision SAR Algorithms," *Geoscience and Remote Sensing, IEEE Transactions on*, vol. 34, no. 1, pp. 212–218, Jan 1996.
- [60] A. Papoulis, *Systems and Transforms with Applications in Optics*, ser. McGraw-Hill series in systems science. Malabar, Florida : Robert Krieger Publishing Company, 1968.

Curriculum Vitae

Name: Kai Liu

Post-Secondary Education and Degrees: 2001-2005, B.Eng.
Telecommunication and Information Engineering
Nanjing University of Posts and Telecommunications
Nanjing, Jiangsu, P.R.China

2006 - 2009, M.Sc.
Purple Mountain Observatory
Chinese Academy of Sciences
Nanjing, Jiangsu, P.R.China

2012 - 2014, M.E.Sc.
Electrical and Computer Engineering
The University of Western Ontario
London, Ontario, Canada

Related Work Experience: Teaching Assistant
The University of Western Ontario
2012 - 2013

Research Assistant
The University of Western Ontario
2012 - 2014

Publications:

[1] K. Liu, X. Wang, J. Samarabandu, and A. Akhtar, "Monostatic Airborne SAR Using License Exempt WiMAX Transceivers," to appear in *Proc. Vehicular Technology Conference. VTC Fall 2014, IEEE 80th*, September 2014.

[2] K. Liu, X. Wang, J. Samarabandu, and A. Akhtar, "Enhanced WiMAX SAR System Equipped with Multiple Modes," to appear in *Proc. International Conference on Information and Automation. ICIAfS'14, IEEE 7th*, December 2014.